

## **General Disclaimer**

### **One or more of the Following Statements may affect this Document**

- This document has been reproduced from the best copy furnished by the organizational source. It is being released in the interest of making available as much information as possible.
- This document may contain data, which exceeds the sheet parameters. It was furnished in this condition by the organizational source and is the best copy available.
- This document may contain tone-on-tone or color graphs, charts and/or pictures, which have been reproduced in black and white.
- This document is paginated as submitted by the original source.
- Portions of this document are not fully legible due to the historical nature of some of the material. However, it is the best reproduction available from the original submission.

TR-83-18

(NASA-CR-174541) SURFACE ACOUSTIC  
WAVE/SILICON MONOLITHIC SENSOR/PROCESSOR  
Final Report (Syracusc Univ., N. Y.) 123 p  
HC A06/MF A01 CSCL 13H

N84-10366

Unclas  
G3/31 15190

Surface Acoustic Wave/Silicon Monolithic  
Sensor/Processor

Final Report

September, 1983

Prepared Under  
NASA Grant #NSG1611

by the

Department of Electrical and Computer Engineering  
Syracuse University  
Syracuse, NY 13210

Stephen T. Kowel  
Philipp G. Kornreich  
Principal Investigators

Akbar Nouhi  
Robert Kilmer  
Mohammed Ayub Fathimulla  
Ebrahim Mehter



## ABSTRACT

A new technique for sputter deposition of piezoelectric zinc oxide (ZnO) is described. An argon-ion milling system has been converted to sputter zinc oxide films in an oxygen atmosphere using a pure zinc oxide target. Piezoelectric films have been grown on silicon dioxide and silicon dioxide overlaid with gold. The sputtered films were evaluated using surface acoustic wave measurements, X-ray diffraction, scanning electron microscopy, Auger electron spectroscopy, and resistivity measurements. The effect of the sputtering conditions on the film quality and the result of post-deposition annealing are discussed.

The application of these films to the generation of surface acoustic waves is also discussed. Piezoelectric ZnO overlays on silicon are of interest because they represent an integration of surface wave and semiconductor technologies. This integration provides the ability to acoustically modulate image-generated carriers in a prototype surface acoustic wave/silicon smart sensor known as a DEFT device.

## CONTENTS

	<u>Page</u>
ACKNOWLEDGEMENT.....	112
LIST OF FIGURES.....	iii
LIST OF TABLES.....	vii
<b>Chapter</b>	
I    Introduction.....	1
II   General Theory of Sputtering.....	4
III  Description of the Argon-Ion Sputtering Unit..	9
IV   Deposition Procedure.....	18
V    Dependence of Film Quality and System Performance on the Sputtering Conditions.....	21
VI   The Effect of Post-Deposition Annealing on the Film Quality.....	51
VII  Comparision of the Argon-Ion System With Competitive Sputtering Units.....	77
VIII Application of the Zinc Oxide Films to the DEFT Device.....	81
IX   Conclusion.....	96
<b>Appendices</b>	
A    Substrate Cleaning Procedure.....	97
B    Scanning Auger Electron Spectroscopy Standards	98
C    Calculation of the Acoustic Mode.....	103
REFERENCES.....	113

## LIST OF FIGURES

<u>Figure No.</u>	<u>Title</u>	<u>Page</u>
3.1	Schematic diagram of the argon-ion sputtering unit.....	10
3.2	Schematic diagram of the ion source and grid assembly.....	12
3.3	The target assembly. The shafts of the target holder have been hollowed to allow water to circulate behind the target.....	16
5.1	Graph showing the sputtering rate as a function of the percentage of oxygen in the sputtering gas.....	22
5.2	Graph showing the sheet resistance of the film as a function of the percentage of oxygen in the sputtering gas.....	25
5.3	SEM photograph of a ZnO film sputtered at 130 degrees centigrade.....	30
5.4	SEM photograph of a ZnO film sputtered at 400 degrees centigrade (1 micron scale)..	31
5.5	SEM photograph of the film pictured in Figure 5.4 with a higher magnification (400 nanometer scale).....	32
5.6	Auger analysis of the film sputtered at low temperature after 90 seconds of depth profile.....	34
5.7	Auger analysis of the high temperature film after 90 seconds of depth profile...	36
5.8	Auger analysis of the low temperature film after four and one half minutes of the depth profile.....	38
5.9	Auger analysis of the high temperature	

	film after four and one half minutes of the depth profile.....	39
5.10	Auger analysis of the low temperature film upon completion of the depth profile	40
5.11	Auger analysis of the high temperature film upon completion of the depth profile	41
5.12	Graphical representation of the dependence of the structure of the sputtered film on the substrate temperature and sputtering gas pressure.....	44
5.13	SEM photograph of an etched ZnO film.....	45
5.14	SEM photograph of the film pictured in Figure 5.13 away from the film edge.....	46
5.15	Graph showing the sputtering rate versus the acceleration voltage for a constant beam current.....	48
6.1	Graph showing the zinc oxide sheet resistance as a function of the annealing temperature.....	52
6.2	Auger analysis of the unannealed film upon completion of the depth profile.....	55
6.3	Auger analysis of the annealed film after completion of the depth profile.....	56
6.4	Expanded version of the zinc peaks for the unannealed film.....	57
6.5	Expanded version of the zinc peak for the annealed film.....	58
6.6	Expanded version of the oxygen peak for the unannealed film.....	59
6.7	Expanded version of the oxygen peak for annealed film.....	60
6.8	Variation of the height of zinc, carbon, oxygen peaks as a function of the profile time for the unannealed film.....	62
6.9	Variation of the height of zinc, carbon, and oxygen peaks as a function of the profile time for the annealed film.....	63
6.10	Variation of the average concentration of zinc, carbon, and oxygen as a function of	

	the profile time.....	64
6.11	Variation of the average concentration of zinc, carbon, and oxygen as a function of the profile time.....	65
6.12	Results of the diffraction analysis for the unannealed film.....	68
6.13	Results of the diffraction analysis for the annealed film.....	70
6.14	Surface acoustic wave insertion and detection apparatus.....	71
6.15	Picture of the acoustic response of the ZnO film.....	72
6.16	Graph showing the surface acoustic wave amplitude as a function of the annealing temperature.....	74
8.1	Graph of $k^2$ versus $hk$ for $hk < 5$ .....	83
8.2	The device consists of an array of photo-diodes, each connected in parallel by an interdigital contact pattern.....	85
8.3	Transducer geometry for the sensor of Figure 8.2.....	86
8.4	An overview of the DEFT device.....	87
8.5	Detail of the image sensing array elements	88
8.6	Prototype zinc oxide DEFT device.....	92
8.7	Output of the ZnO device when illuminated with uniform light.....	93
8.8	Output of the ZnO device with no image....	95
B.1	Auger standard for oxygen.....	99
B.2	Auger standard for carbon.....	100
B.3	Auger standard for zinc.....	101
B.4	Auger standard for argon.....	102
C.1	A cross-section of the transducers.....	104
C.2	Direction of propagation of the SAW.....	106

C.3 Dispersion characteristics for ZnO on Si.. 108

LIST OF TABLES

<u>Table No.</u>	<u>Title</u>	<u>Page</u>
5.1	Data for Figure 5.1. Each film was sputtered for 5 minutes under the conditions given in Section 4.....	23
5.2	Data for Figure 5.2.....	26
5.3	Data for Figure 5.15. Each film was sputtered for 5 minutes with a 50mA beam current.....	49
6.1	Data for Figure 6.1.....	53
6.2	Data for Figure 6.16. All attenuations are referenced to 30mV.....	76
7.1	Comparison of the argon-ion sputtering unit with competitive systems.....	83
C.1	Calculation of the acoustic mode by measuring the separation between successive transducers	110
C.2	Calculation of the acoustic mode using the geometry of the interdigital transducer.....	111

## I Introduction

The goal of this program was to create a new Deft sensor based on a silicon photodiode array as the sensing medium, with a thin film zinc oxide overlay to provide the surface acoustic wave modulation. If such a sensor could be developed, it could have a number of advantages in comparison with the current DEFT sensor technology based on a cadmium sulfide film as the image sensing material deposited on a lithium niobate piezoelectric substrate. Among these advantages would be very fast time response to changes in the image, integration of excitation and processing circuitry and, ultimately, higher resolution.

This report reviews the progress to date and describes the work that needs to be done if the Deft sensor is ultimately to be based on a silicon semiconductor technology. Our efforts to create effective launching of surface acoustic waves on silicon using zinc oxide overlays has been successful and our results are comparable to those achieved in other laboratories. Current difficulties in detecting significant image transform signals seem to be related largely to the specific design of the silicon photodiode array which we obtained early in this research program. It is hoped that a future opportunity will arise which will permit the redesign of the diode arrays which will provide the isolation necessary to obtain significant signal response.

The field of surface acoustic wave (SAW) devices has been an area of considerable activity for many years. Traditional acoustoelectric devices have used a piezoelectric material, typically lithium niobate, as the substrate. Interdigital transducers<sup>(19)</sup> are deposited on the substrate to generate and detect surface acoustic waves. Since the substrate is piezoelectric the acoustic wave will carry an associated electric field. This phenomenon has been used to create many useful devices such as delay lines, filters, convolvers, and correlators.

The possibility of integrating SAW and semiconductor technology has generated interest in zinc oxide (ZnO) thin films. Much of this interest has been directed towards developing new sputtering techniques for ZnO. By sputtering zinc oxide, which is piezoelectric, on silicon, which is not piezoelectric, the functions of active and acoustic devices can be combined on one substrate. RF magnetron, DC magnetron, RF diode, DC diode, and DC triode units have all been used for this purpose with varying degrees of success<sup>(21,22)</sup>.

It is with this application in mind that we have developed a new sputtering technique for zinc oxide. This innovative procedure utilizes an argon-ion beam milling apparatus converted for sputtering. This system has been

used to grow acoustic quality ZnO, that is a piezoelectric film that will support an acoustic wave with a minimum of attenuation, on oxidized silicon and oxidized silicon overlaid with gold.

Previous work at this laboratory had focused on designing the fixtures used in the system <sup>(39)</sup>. While zinc oxide films had been grown, the films generally suffered from high conductivity and a lack of piezoelectric activity. Our most recent efforts have overcome these problems while more completely characterizing the sputtering process. We have also explored the application of these films to a SAW device known as DEFT <sup>(31)</sup> (Direct Electronic Fourier Transform).

The main body of this thesis describes the use, structure, and performance of the argon-ion sputtering unit. A comparison of this system with the aforementioned sputtering units is presented. Also discussed are the general theory of sputtering, the results of post-deposition annealing of the ZnO films, and the application of the films to the generation of surface acoustic waves. The appendices present the cleaning procedure used for the substrates, Auger standards, and a calculation of the acoustic mode present in the films.

## II General Theory of Sputtering

The ability to deposit high quality thin films in a reproducible fashion is essential for any microelectronic device. Traditionally, this crucial task has been performed by evaporation techniques such as resistance heating. However, the demands of the electronic industry for films unattainable by conventional methods has stimulated considerable effort towards developing more versatile deposition techniques. One of the outgrowths of this search has been the sputtering process.

The biggest advantage of sputtering over other deposition techniques is its ability to deposit materials incompatible with other methods. Sputtering offers the capability to deposit with good adhesion and uniform thickness materials such as <sup>(1)</sup> :

- (1) multicomponent alloys,
- (2) refractory materials,
- (3) insulating films.

Of course, there are also disadvantages. Among them are:

- (1) source material must be available in sheet form,
- (2) deposition rates are lower than most other processes,
- (3) source material must be cooled,

(4) large number of parameters must be controlled.

Sputtering is a method of film deposition which involves the removal of material from a solid target by bombarding it with positive ions. The simplest way to visualize the ion sputtering process is as a transfer of momentum from the incident ions to the target material. A bombarding ion of mass  $M$  (usually a noble gas) is incident on a stationary target of atoms of mass  $m$ , the material to be sputtered. Upon collision, the maximum energy  $E_m$

(2)  
transferred to the stationary atoms is

$$E_m = 4mM(E_i)^2 / (m+M)^2$$

where  $E_i$  is the energy of the incident ion.  $E_m$  is often referred to as the energy-transfer coefficient. If the momentum transferred to the stationary atom is greater than some threshold value, the stationary atom will be displaced, or sputtered.

If the incident ion has more than the threshold energy  $E_t$  (typically 10 to 35eV) but less than some upper limit (about 50KeV), the mean energy  $E$  of the struck target atom will be

$$E = (E_s + E_t) / 2$$

where  $E_s$  is the kinetic energy of the initially stationary particle after the collision. For energies below  $E_t$ , no sputtering will occur. For energies much greater than 50KeV, the bombarding ion will bury itself in the target lattice (ion implantation) and will not cause any sputtering.

A parameter which characterizes the sputtering process is the sputtering yield  $S$ , which is defined as the number of ejected atoms per bombarding ion. Since the bombarding ion will typically undergo several collisions (that is, more than one atomic layer is involved), the sputtering yield is usually greater than unity.

Calculation of the sputtering yield involves determining the number of atoms displaced by a primary hit. In general, the yield will be a function of the angle of incidence of the ions, their energy, the position at which the yield is measured, and the materials involved in the

(3)  
sputtering process .

The yield is normally not dependent on the target temperature unless the sputtering process raises the target temperature to the point where sputtering and evaporation

are superimposed <sup>(4)</sup>. Since the sputtering process is very inefficient (about 95% of the incoming ion's energy is transformed into heat), the target material must be cooled to prevent evaporation, especially when sputtering low melting point materials.

Sputtering yields rarely differ by more than an order of magnitude, even for materials with widely different evaporation rates. This allows for sputtering of multicomponent materials at a relatively uniform rate. A rather interesting phenomenon, and one which is unexplainable via the billiard ball model, is that yields vary much more with ion species than with target atom

species <sup>(5)</sup>.

As the energy of the incident ion is increased from the threshold value the yield normally rises exponentially at first, then linearly, reaches a maximum value, and eventually begins to decrease. For low energies, Gurmin et

al. <sup>(6)</sup> have found that the yield is proportional to the energy where the proportionality constant depends on the ion and target masses, the energy transfer coefficient, and the heat of sublimation of the target material. In the medium

energy range, the yield can be shown to be <sup>(7)</sup>

$$S = (E/4E_t) [1 + [\ln(E/E_s)/2]]^{-.5} Qn^{2/3}$$

where  $Q$  is the collision cross section and  $n$  is the number of atoms of the target material per unit volume. For this energy range,  $Q = (a)^2$  and

$$a = A_o / (Z_1^2 + Z_2^2)^{.5}$$

where  $Z_1$  is the atomic number of the bombarding ion,  $Z_2$  is the atomic number of the target atom, and  $A_o$  is the Bohr radius of the atom. For high energies, the billiard ball model breaks down and the sputtering yield falls off as the incident ions begin to bury themselves in the lattice.

An interesting and rarely discussed point is what happens to those ions that do imbed themselves in the target. If the ions are from a noble gas (typically argon), then it has been observed via electron microscopy that the ions form microscopic noble-gas bubbles in the target

material (8). It is generally believed that these "bubbles" have little effect on the sputtering yield, but to date no in-depth studies have been done to verify this.

### III Description of the Argon-Ion Sputtering Unit

The system used for sputtering is a converted ion-beam etching apparatus, a 3" Veeco Microetch station (model number 3ME-156). This unit is significantly different than the diode, triode, and magnetron systems <sup>(2)</sup> used by others. Each technique possesses unique features and advantages, a point to be considered in greater detail in Section 7.

A schematic representation of the system is shown in Figure 3.1. A brief description of the operation of the unit is given below, followed by a detailed discussion of each of the major sections.

An arc discharge between the anode and cathode serves as the ion source. The ions needed to support this discharge are supplied by the incoming gas, in this case a 60/40 mixture of argon and oxygen. For a discussion of the gas mixture used see Section 5. The accelerating system, which is at -1KV with respect to the cathode, extracts the beam from the ion source into the target chamber. The focusing coil produces a magnetic field which both focuses and contains the accelerated ions. The energy and current density of the ion beam can be adjusted via the accelerating potential, magnetic field strength, and arc discharge. These accelerated ions impinge upon the zinc oxide target below where sputtering occurs. The off-sputtered particles then deposit on the heated substrates.

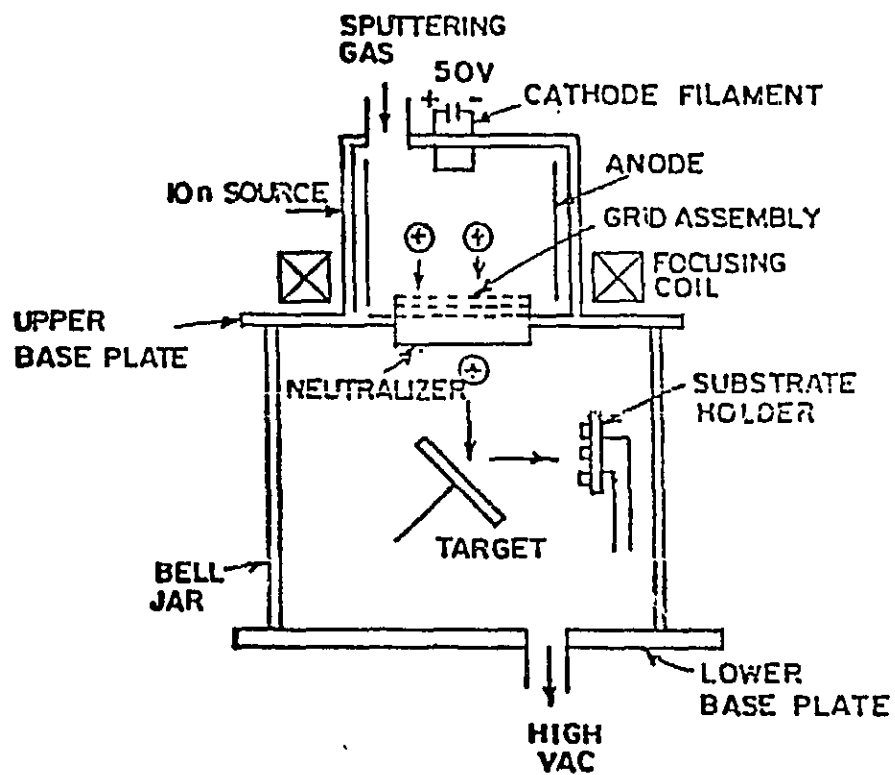


Figure 3.1 - Schematic diagram of the argon-ion sputtering  
 (2)  
 unit .

ORIGINAL PAGE IS  
 OF POOR QUALITY.

To prevent the buildup of a retarding potential on the surface of the target when sputtering insulating materials, a neutralizing filament is provided in the main chamber.

The entire process occurs at a pressure of  $10^{-4}$  Torr to ensure a large mean free path for both the ion beam and the sputtered particles.

From the above discussion, it is apparent that the sputtering unit may be divided into three main sections:

- (1) Ion Source,
- (2) Ion Acceleration System,
- (3) Target Chamber.

The entire apparatus rests on a 22" diameter aluminum baseplate and is intended to be used in conjunction with an 18" bell jar. Each of these components is described in detail below <sup>(9)</sup>.

#### (1) Ion Source (Figure 3.2)

As its name indicates, the ion source supplies a continuous flow of positive ions for the ion beam. Designed to function at pressures in the range of  $10^{-4}$  Torr as measured at the upper baseplate, this Kaufman type discharge source utilizes a regulated piezoelectric gas feed-through valve to maintain a stable operating pressure. A 60/40 mixture of argon and oxygen is used as the ionizing gas.

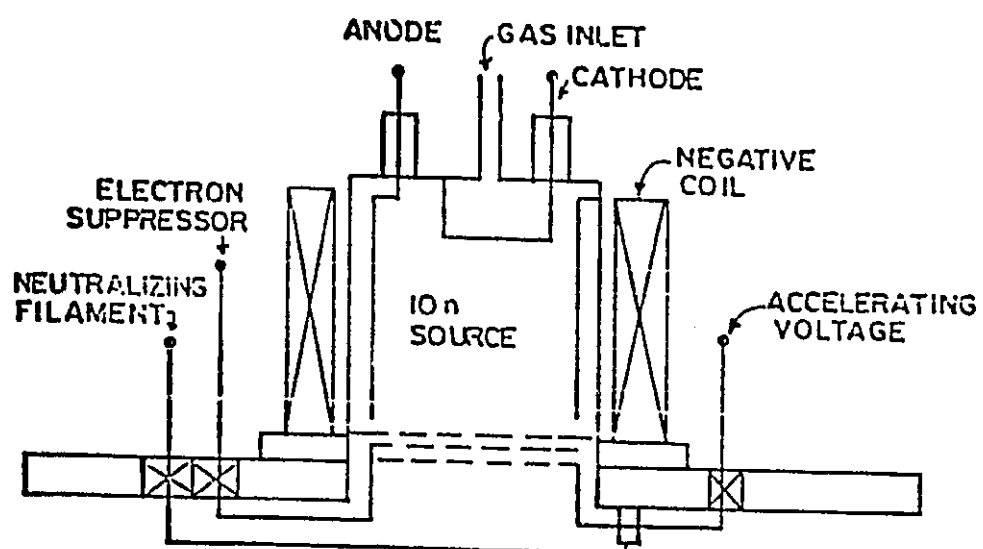


Figure 3.2 - Schematic diagram of the ion source and grid  
(9)  
assembly .

ORIGINAL PAGE IS  
OF POOR QUALITY

For the cathode, an electron emitting tungsten filament together with a regulated power supply is used. The molybdenum cylinder serves as the anode.

An electromagnet is placed outside the ion source to initiate a cycloidal trajectory for the ions. This electromagnet applies a magnetic field of up to 50 Oersteds in the ion source to increase the number of ionizing collisions. The resulting cycloidal motion of the electrons yields a more stable discharge and allows the user to control the current density profile across the beam. In general, increasing the field strength allows for a flatter beam profile and more uniform sputtering of the target material. This field is of course supplemented by the field produced by the cathode filament (typically  $\pm 10$  Oersteds).

## (2) Ion Acceleration System (Figure 3.2)

The molybdenum grid assembly located at the bottom of the ion source extracts the ion beam from the source. These three perforated grids focus and accelerate the beam while preventing ions in the target chamber from returning to the source.

The first of these grids is maintained at the same potential as the ion source and serves as the system ground. By placing a stainless steel plate of the desired size and shape on top of this grid, the operator is able to vary the

beam size and configuration from zero to three inches. Since this plate is at the same potential as the source, it will not be sputtered, affording the user increased flexibility.

The second grid is biased at 175-250V and acts as an electrostatic barrier to prevent electrons in the target chamber from entering the ion source.

The third and final grid serves as the accelerating potential. This grid affords up to -2KV of accelerating voltage, with -1KV being a typical operating value.

In addition to the aforementioned functions, the grids also provide a pressure differential between the discharge and target chamber. Above the grids, in the ion source, a relatively high pressure ( $10^{-3}$  Torr) is required to support a stable discharge. Below the grids, in the target chamber, a lower pressure ( $10^{-4}$  Torr) is needed to insure a large mean free path for the accelerated ions and the off-sputtered particles. The grids act as a "barrier" between the ion source and the target chamber, thereby providing the pressure differential required to maintain both pressures simultaneously.

Located directly below the upper baseplate is the neutralizing filament. The tungsten wire filament serves to neutralize the ion beam and eliminate any surface charge on

the target. This allows for sputtering of both conducting and non-conducting targets. In light of this, it is apparent that the current emitted by this filament should be slightly greater than the total ion current, thereby preventing the buildup of a retarding potential between the target and the bottom (accelerating) grid. Any excess electrons emitted by the neutralizer will be absorbed by the suppressor (second grid).

### (3) Target Chamber (Figure 3.3)

The target consists of a five inch 99.99% pure zinc oxide disk mounted on a water-cooled backing plate. Facilities are provided to rotate the target and change its angle with respect to the ion beam from outside the vacuum system.

With the target set at a 45 degree angle relative to the ion beam, the sputtered particles are directed towards a 12.7cm substrate holder parallel to and approximately 15cm from the center of the ion beam. As with the target, provisions have been made to rotate the substrate holder from outside the bell jar for a more uniform deposition. A coiled filament is supplied to heat the substrates. The desired temperature is regulated by a thermocouple placed on the surface of the substrate holder and an Omega temperature controller.

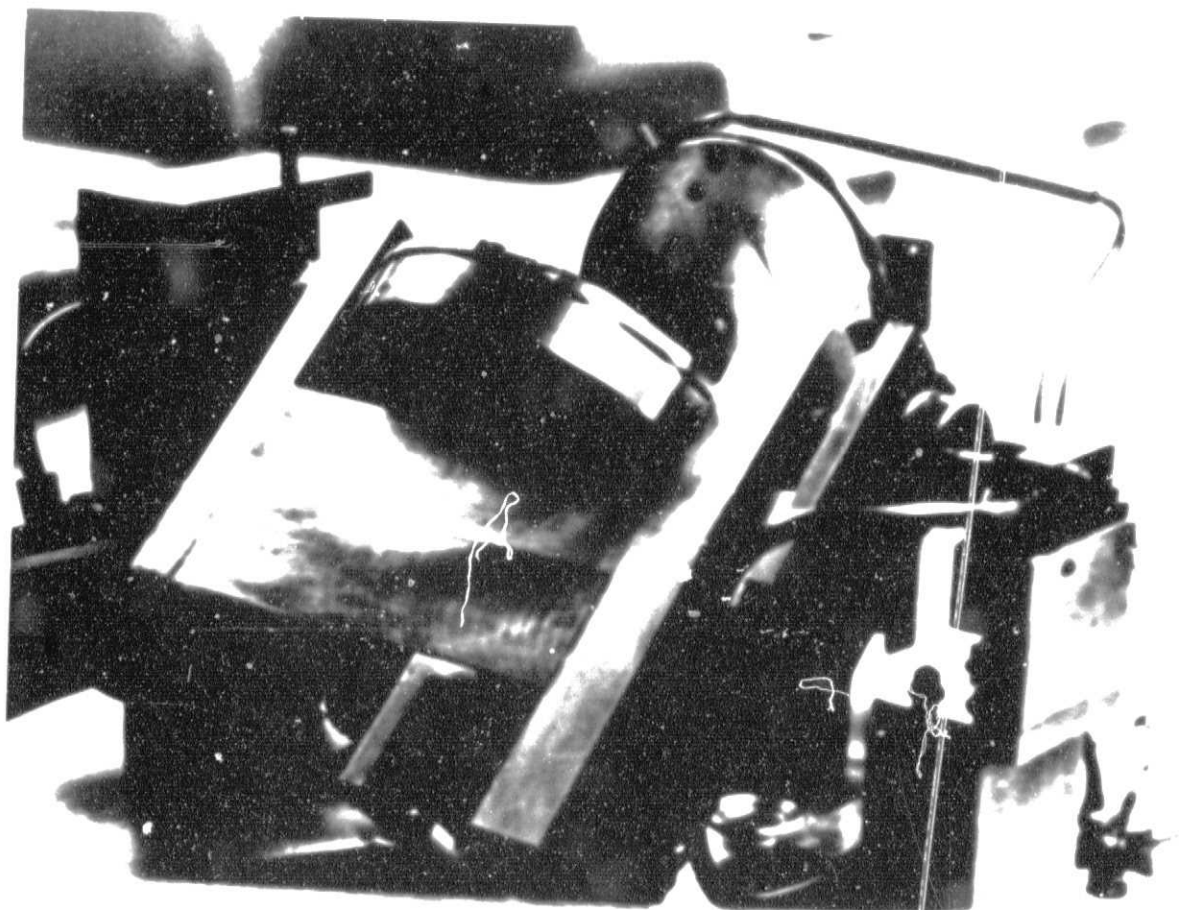


Figure 3.3 - The target assembly. The shafts of the target holder have been hollowed to allow water to circulate behind the target.

ORIGINAL PAGE  
BLACK AND WHITE PHOTOGRAPH

A shutter is provided to shield the target from the ion beam during initial beam adjustment. Provisions are also made to measure the current density of the beam prior to sputtering as well as the total target current while sputtering.

#### IV Deposition Procedure

As with any microelectronic process, substrate preparation is of the utmost importance. While each individual investigator has his own favorite procedure, each focuses on two points: cleanliness and the preparation of nucleating centers.

Prior to sputtering each of the substrates is cleaned according to the procedure listed in Appendix A. To provide the nucleating centers required for growing a c-axis normal zinc oxide film, a thin layer of chromium and gold is evaporated on the substrate. Wagers<sup>(10)</sup> has shown that a 50 to 100 angstrom thick chromium film will provide the necessary orientation for film growth. This is important since the lack of proper nucleating centers can result in grain boundary reversal, effectively cancelling the piezoelectric effect. While we have successfully grown acoustic quality zinc oxide directly on silicon dioxide, the process is more reproducible using the gold-chromium procedure.

To prepare the system for sputtering the target is sputter-etched for 1/2 hour before placing the substrates in the system. In addition, the zinc foil that is used to protect the target holder from being etched by the ion beam is replaced prior to each sputtering session. The time the system is left open to the atmosphere is kept to a minimum.

After the substrates are placed on the target holder the system is pumped down to an initial pressure of  $1 \times 10^{-6}$  Torr. During this process the substrates are heated to 270 degrees centigrade, allowing them to degas prior to film deposition.

When the substrates have reached the proper temperature the system pressure is stabilized at  $2 \times 10^{-4}$  Torr (as measured at the upper baseplate) by the argon-oxygen gas mixture. This corresponds to a pressure of  $5 \times 10^{-5}$  Torr when measured from the usual location of just below the high vacuum valve. Sputtering is then initiated using the following settings:

Accelerating Voltage	1.0KV
Arc Current	1.0A
Suppressor voltage	175V
Magnet Current	0.8A
Arc Voltage	>60V
Target Current	-5.0mA
Acceleration Current	150mA
Current Density	$1.8 \text{ mA/cm}^2$

The target current, acceleration current, and current density are all typical values and may vary slightly from one session to the next.

The system is then run for approximately six to eight hours, depending on the desired film thickness. This results in a 2 to 3 micron film. After sputtering, the substrates are allowed to cool in the oxygen-argon ambient until a temperature of 200 °C is reached. The system is left in the high vacuum state and not opened until the substrates reach a temperature of 50 °C.

Each film is then annealed at 550 °C in a diffusion furnace with a pure oxygen ambient for 1/2 hour. The results of this post-deposition annealing are discussed in the section on annealing (Section 6).

## V Dependence of Film Quality and System Performance on the Sputtering Conditions

As with any sputtering unit the film quality and overall system performance are sensitive functions of the sputtering conditions. While there are numerous parameters that must be controlled, the four most crucial ones are; sputtering gas oxygen content, substrate temperature, sputtering pressure, and accelerating voltage. Each of these is discussed separately below.

### (1) Oxygen Content

The admission of oxygen into the sputtering gas has two effects. First, and foremost, the presence of oxygen helps maintain the proper stoichiometry of the growing film. Secondly, the oxygen also participates in the sputtering process.

The effect of the percentage of oxygen in the sputtering gas on the sputtering rate is shown in Figure 5.1, the data for which is presented in Table 5.1. Here we see that the sputtering rate decreases rapidly with increasing oxygen. This continues until approximately a 60% oxygen content is reached, at which point the sputtering rate becomes nearly constant. This phenomena is expected since oxygen, with its lower atomic number, is a much less efficient sputtering gas than argon. Therefore, from a

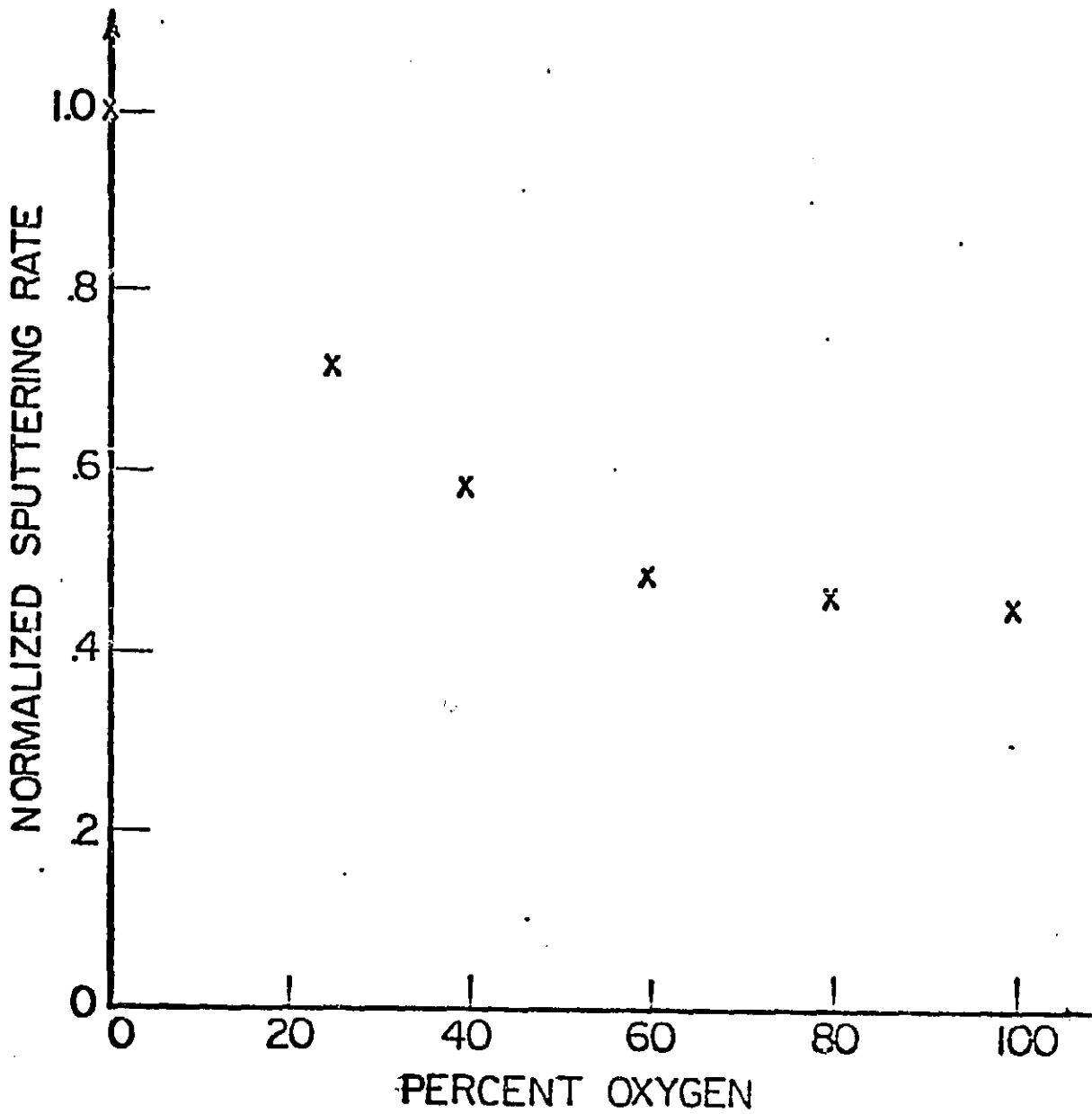


Figure 5.1 - Graph showing the sputtering rate as a function of the percentage of oxygen in the sputtering gas.

ORIGINAL PAGE IS  
OF POOR QUALITY.

Oxygen Content (%)	Acceleration Current (mA)	Film Thickness (Angstroms)	Sputtering Rate (Ang./Sec)
0	65	655	2.18
25	72	472	1.57
40	70	383	1.27
60	70	315	1.05
80	62	300	1.00
100	70	291	0.97

Table 5.1 - Data for Figure 5.1. Each film was sputtered for 5 minutes under the conditions given in Section 4.

deposition rate point of view, the percentage of oxygen allowed into the system should be kept as low as possible.

The other consideration determining the percentage of oxygen in the sputtering gas is the stoichiometry of the growing film. The addition of oxygen to the sputtering gas provides an excess of oxygen ions in the system. Since zinc oxide, zinc ions, and oxygen ions are all sputtered from the target, the presence of the extra oxygen ions tends to decrease the proportion of free zinc in the film. This manifests itself as an increase in substrate resistivity due to proper film stoichiometry. We therefore use the resistivity as a measure of the film stoichiometry.

Figure 5.2 and Table 5.2 show the dependence of the sheet resistance of the film (as measured with a four-point probe) on the percentage of oxygen in the film. Here we see that the presence of 25% oxygen in the sputtering gas yields a six order of magnitude increase in the substrate resistivity. As the oxygen content is increased beyond 40%, the substrates show little further increase in resistivity. These figures are typical for most of the sputtering units in use today. The only systems that normally use a significantly different mixture are those that have a pure zinc target, in which case oxygen gas percentages as high as

100% have been used (11) .

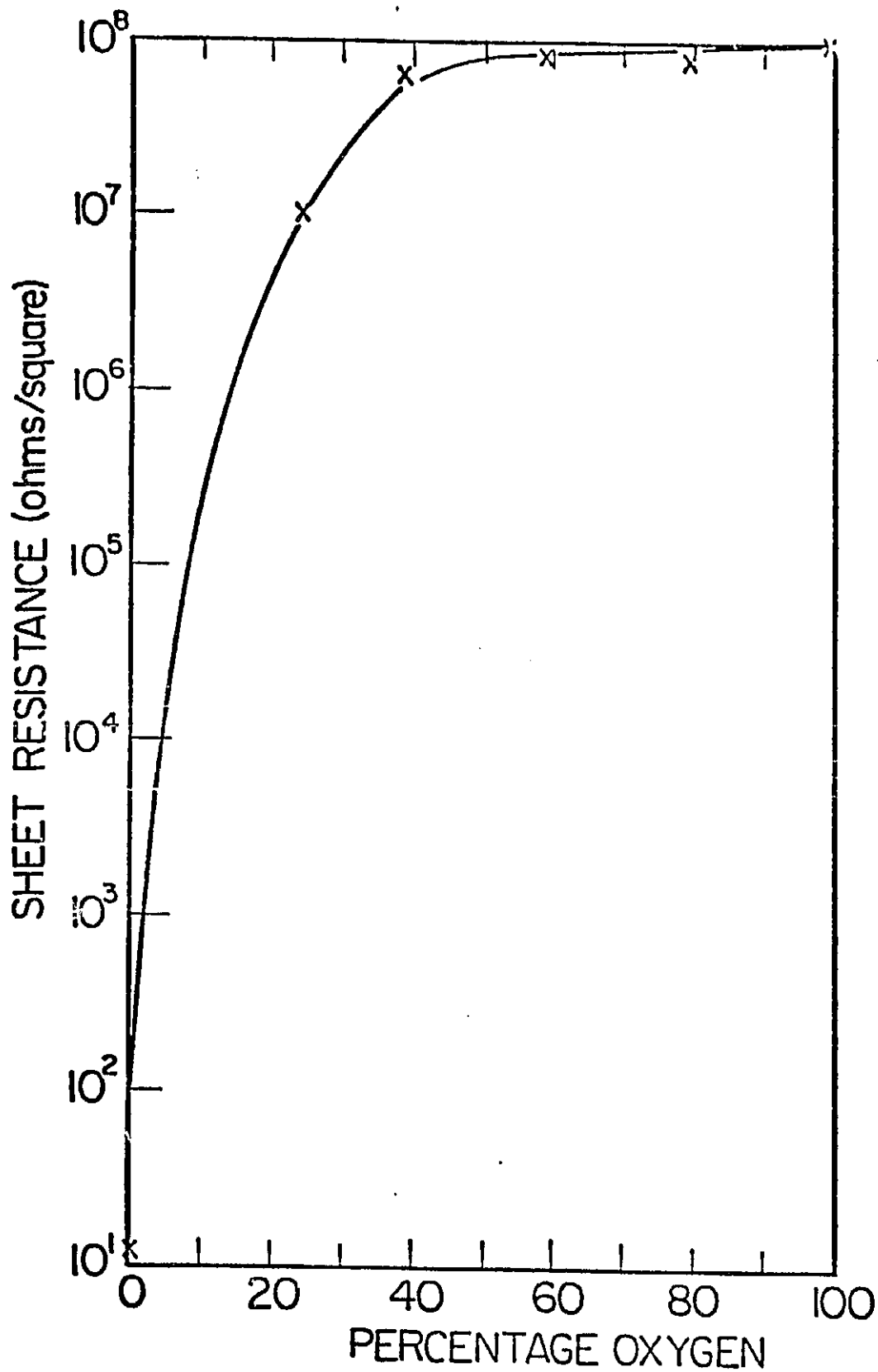


Figure 5.2 - Graph showing the sheet resistance of the film as a function of the percentage of oxygen in the sputtering gas.

ORIGINAL PAGE IS  
OF POOR QUALITY.

Oxygen Content (%)	V (Volts)	I (Amps)	R (Ohms/Square)
0	1.00	.348	13
10	1.00	54.2u	83.6M
25	1.00	.431u	10.1M
40	1.00	75.4n	60.0M
60	1.00	55.9n	81.1M
80	1.00	63.5n	71.3M
100	1.00	49.0n	92.5M

Table 5.2 - Data for Figure 5.2.

The 40% mixture used represents a suitable compromise between sputtering rate and substrate resistivity. It is also in good agreement with work done by researchers at Gould laboratories to determine the optimal percentage of oxygen in the sputtering gas <sup>(12)</sup>. Using an RF Diode sputtering unit they have found via glow discharge mass spectrometry that oxygen contents in this range (25%) yield a minimum in the ratio of Zn ions to ZnO in the plasma. This results in films with the largest amount of c-axis normal orientation and smallest angular distribution of the c-axis orientation about the substrate normal.

## (2) Substrate Temperature

Substrate temperatures for sputtering zinc oxide have traditionally been between 200 to 350 degrees centigrade. The exception to this is once again those systems that use a pure zinc target which tend to run slightly hotter <sup>(4)</sup> (450-500 °C). The argon-ion system operates in the middle of the "traditional" zone at 270 degrees centigrade.

The purpose of heating the substrates is to promote adatom (absorbed atoms) mobility, prevent the formation of voids, and give the proper sticking coefficients for the sputtered materials. A substrate temperature which is too low will result in low density, porous structures with

little piezoelectric qualities or crystalline structure. Too high a substrate temperature will promote excess reevaporation of deposited particles, resulting in a low deposition rate and an abnormally rough surface.

Using the given temperature of 270 degrees centigrade, high density films exhibiting good piezoelectric activity have been grown on both amorphous and crystalline substrates. Films sputtered at lower temperatures have a very high resistivity, but no piezoelectric properties. For temperatures much greater than 270<sup>o</sup> C, the resistivity falls off rapidly. Again there is no piezoelectric activity.

While this temperature is comparable to that used by other researchers, it is not exactly coincident with the prevailing theory on the optimum substrate temperature for film deposition presented by Vincent et al. (13). Vincent and his coworkers have presented a theory that correlates the optimum substrate temperature  $T_s$  for vacuum deposited thin films and the boiling temperature  $T_b$  of the deposited material. They have shown rather conclusively for a number of materials that a ratio of  $T_s$  to  $T_b$  equal to .33 results in the optimization of numerous film properties. It is their belief that this ratio provides a rate of reevaporation from well defined, but disordered, regions just equal to the deposition rate, resulting in a highly

crystalline film with a minimum number of voids.

For zinc oxide ( $T = 2400$  degrees centigrade), this gives  
<sup>b</sup>  
 a substrate temperature of  $800^{\circ}\text{C}$ , almost triple that indicated. This apparent discrepancy indicates that there are other parameters involved such as the sputtering pressure (see part three of this section).

To obtain a quantitative measure of the differences between films sputtered at high and low temperature, both a scanning electron microscope (SEM) <sup>(14)</sup> and Auger electron spectroscopy analysis <sup>(15)</sup> (SAM) were performed. The SEM is a high-resolution microscopy technique which gives a visual indication of the film surface. The Auger analysis allows for the determination of the elements present on the film surface.

The SEM photograph of a film sputtered at low temperature <sup>o</sup> ( $130^{\circ}\text{C}$ ) is shown in Figure 5.3. Here we see that the film is very smooth, exhibiting a surface roughness of about 1000 Angstroms. In addition there are many long striations present. By comparison, the film sputtered at <sup>o</sup>  $400^{\circ}\text{C}$  (Figures 5.4 and 5.5) shows a definite periodic pattern. However, the surface is very rough and voided.



Figure 5.3 - SEM photograph of a ZnO film sputtered at  
130 C.

ORIGINAL PAGE  
BLACK AND WHITE PHOTOGRAPH

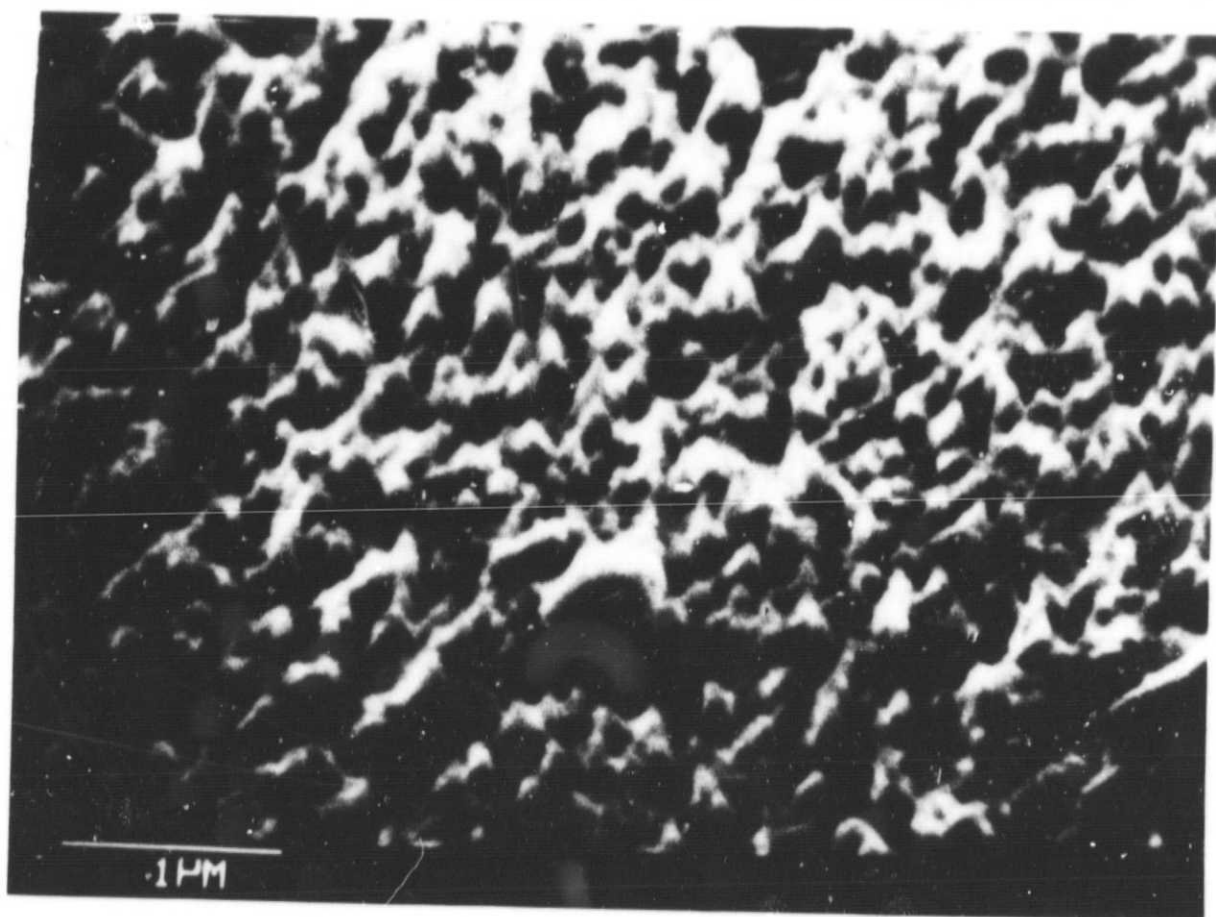


Figure 5.4 - SEM photograph of a ZnO film sputtered at 400<sup>o</sup> C  
(1 micron scale).

ORIGINAL PAGE  
BLACK AND WHITE PHOTOGRAPH

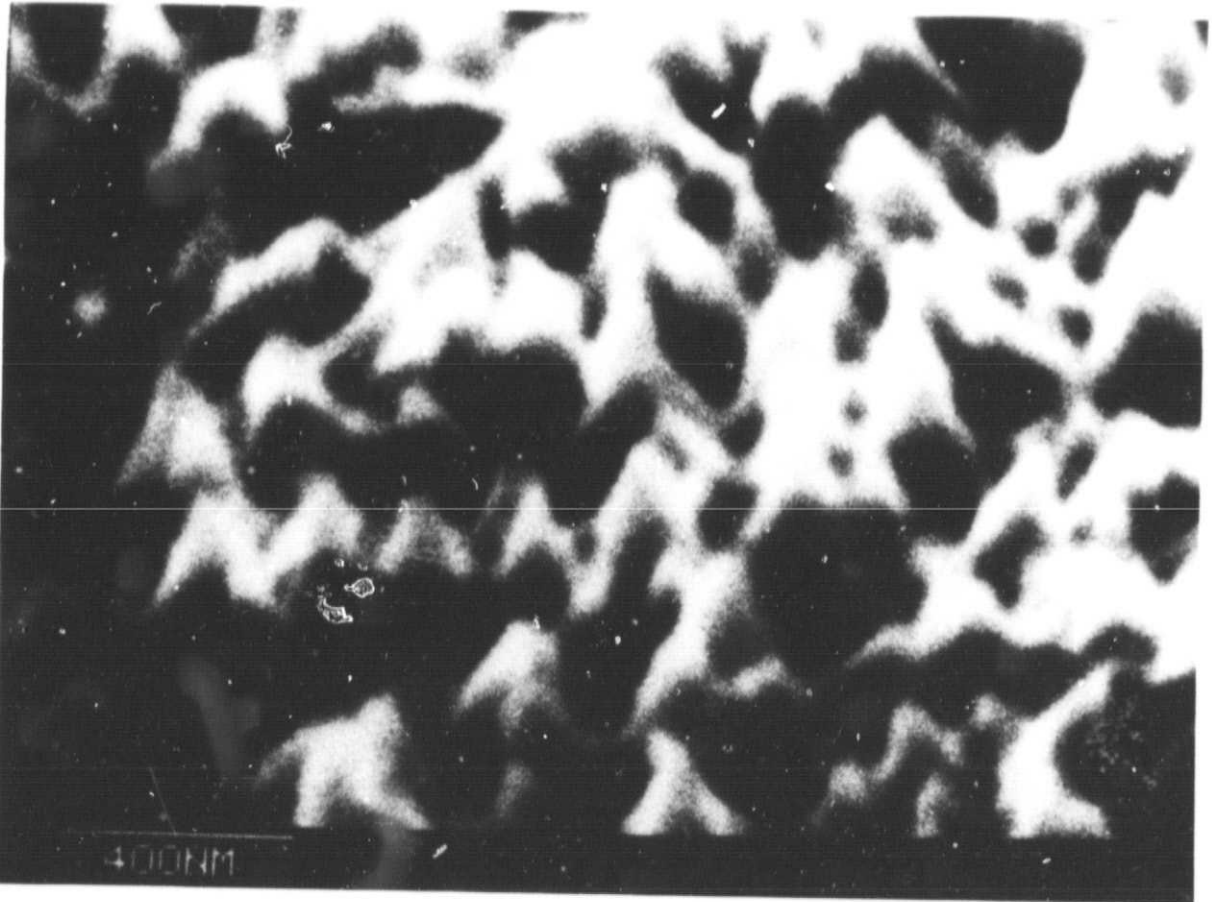


Figure 5.5 - SEM photograph of the film pictured in Figure 5.4 with a higher magnification (400 nanometer scale).

ORIGINAL PAGE  
BLACK AND WHITE PHOTOGRAPH

Obviously the adatom mobility is too low in the first, low temperature, case and too high in the second. For the low temperature film, the incoming particles do not receive sufficient thermal energy to "skate" along the surface of the film until they reach a proper nucleating center. This results in a porous structure with almost no visible surface roughness. For the second (high temperature) case, the particles receive so much energy that they not only skate along the surface, but are also reevaporated. This reevaporation is in excess of that proposed by Vincent, resulting in a surface roughness of about 1/2 micron.

An Auger analysis was performed on each of the above films to determine the difference in their elemental compositions. This technique allows for the determination of the elements present at the film surface. In addition it is possible to determine the bulk composition by using the system's built-in sputtering unit to etch the surface of the film (depth profile). While quantitative results are difficult to obtain with this type of analysis, it does allow for the comparison of the relative concentration of the elements present in different films. By comparing the ratio of the heights of the Auger peaks for each element, it is possible to determine the change in the proportion of the elements from one film to the next.

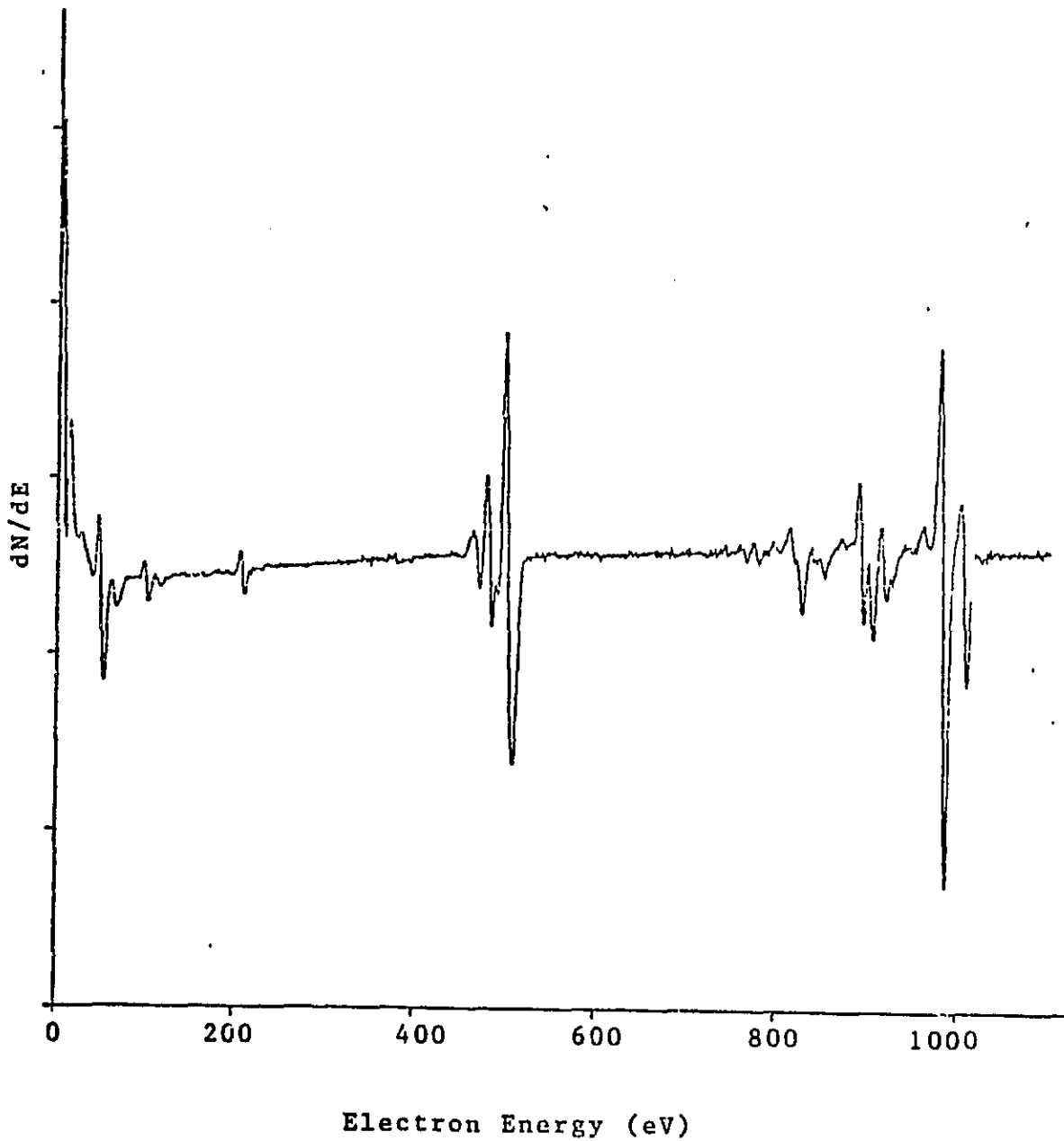


Figure 5.6 - Auger analysis of the film sputtered at low temperature after 90 seconds of depth profile.

ORIGINAL PAGE IS  
OF POOR QUALITY

Figure 5.6 presents the Auger analysis results for the low temperature film after 90 seconds sputtering time. This initial sputter-etch is done to remove any surface contamination. Using an average sputtering rate of 30 angstroms per minute for the Auger's systems built-in sputtering unit, this corresponds to a depth of 45 angstroms. By comparison with the Auger electron spectroscopy data presented in Appendix B, three elements can be identified; oxygen, argon, and zinc.

The peaks from zero to 150eV correspond to zinc. The small peak at 200eV is argon. Those peaks in the 500eV range are due to oxygen. Another set of zinc peaks occurs at 1000eV.

From Figure 5.6 we see that the ratio of the height of the major zinc peak to the oxygen peak is about 1.23. For the high temperature film, Figure 5.7, the ratio is only 1.05. In addition, a small amount of carbon is present. This implies that there is more zinc present in the higher resistivity film!

Initially, it may seem rather unusual that an increase in the zinc concentration would lead to an increase in the conductivity. However, for a compound such as zinc oxide it is the balance or ratio of the elements which is important. Since the more stoichiometric the film is the higher the resistivity should be, one can infer that a ratio of the zinc to oxygen peak height near 1.23 indicates a well grown,

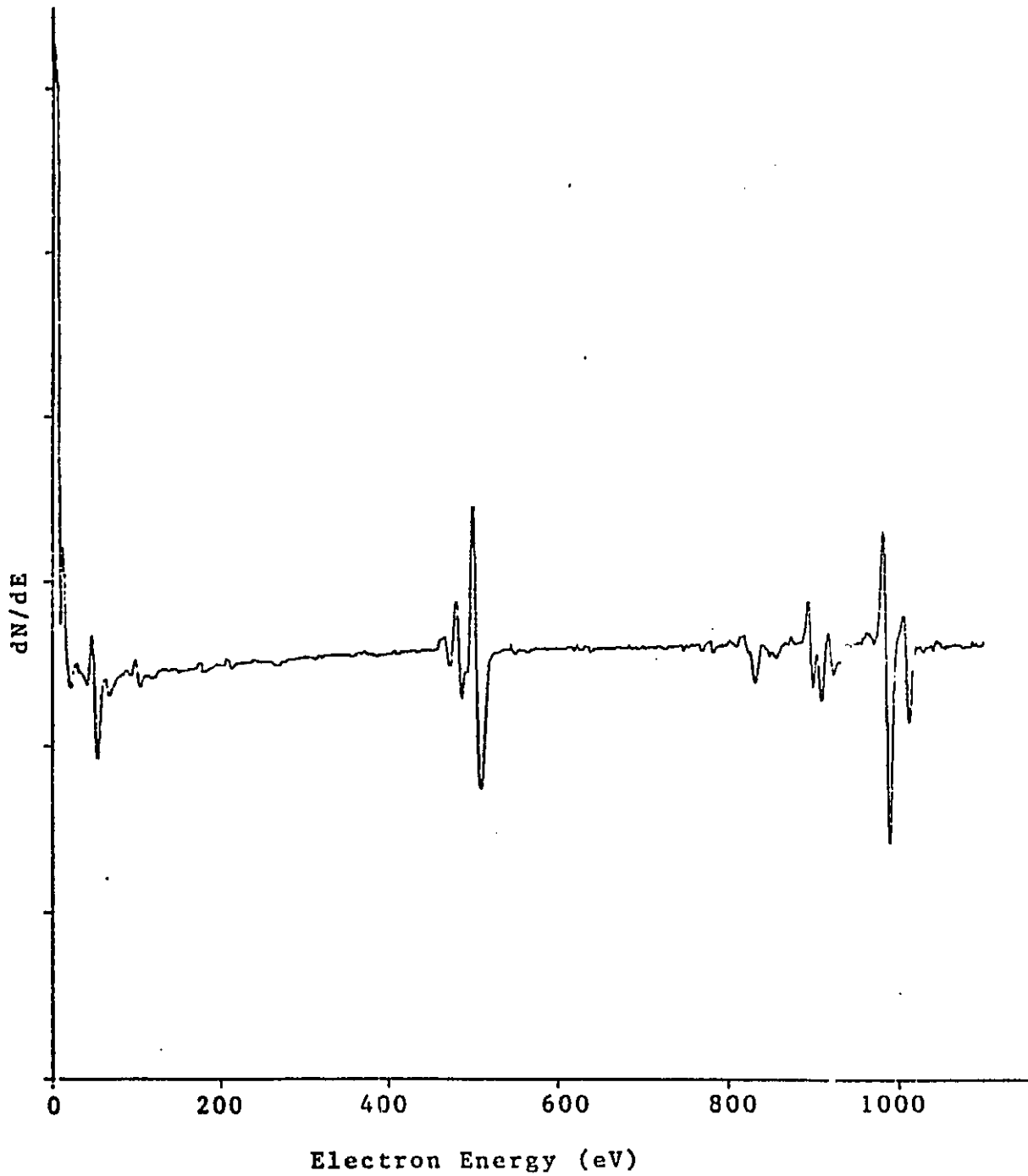


Figure 5.7 - Auger analysis of the high temperature film after 90 seconds of depth profile.

ORIGINAL PAGE IS  
OF POOR QUALITY

stoichiometric film. As the ratio moves either side of 1.23, the balance between the zinc and oxygen concentrations will be upset, causing a decrease in the resistivity.

Again these results can be related to the adatom mobility. For low temperatures there is insufficient energy for the heavy zinc atoms to reevaporate. As the substrate temperature increases the adatom mobility rises, resulting in increased evaporation. This results in a lower zinc concentration, a film which is not stoichiometric, and a lower resistivity.

Figures 5.8 thru 5.11 show the results of continued sputtering on each of the films. The ratios given persist for both films during the entire depth profile (about 300 angstroms). The only notable change is that the carbon present in the high temperature film decreases, indicating its presence is only a surface contaminant.

### (3) Sputtering Pressure

One of the biggest differences between the various sputtering units in terms of operating characteristics is the sputtering pressure. In general, the lower the sputtering pressure, the purer the film, although this is

not always the case <sup>(16)</sup>. The lower pressure limit of the system is determined by the point at which the ion source

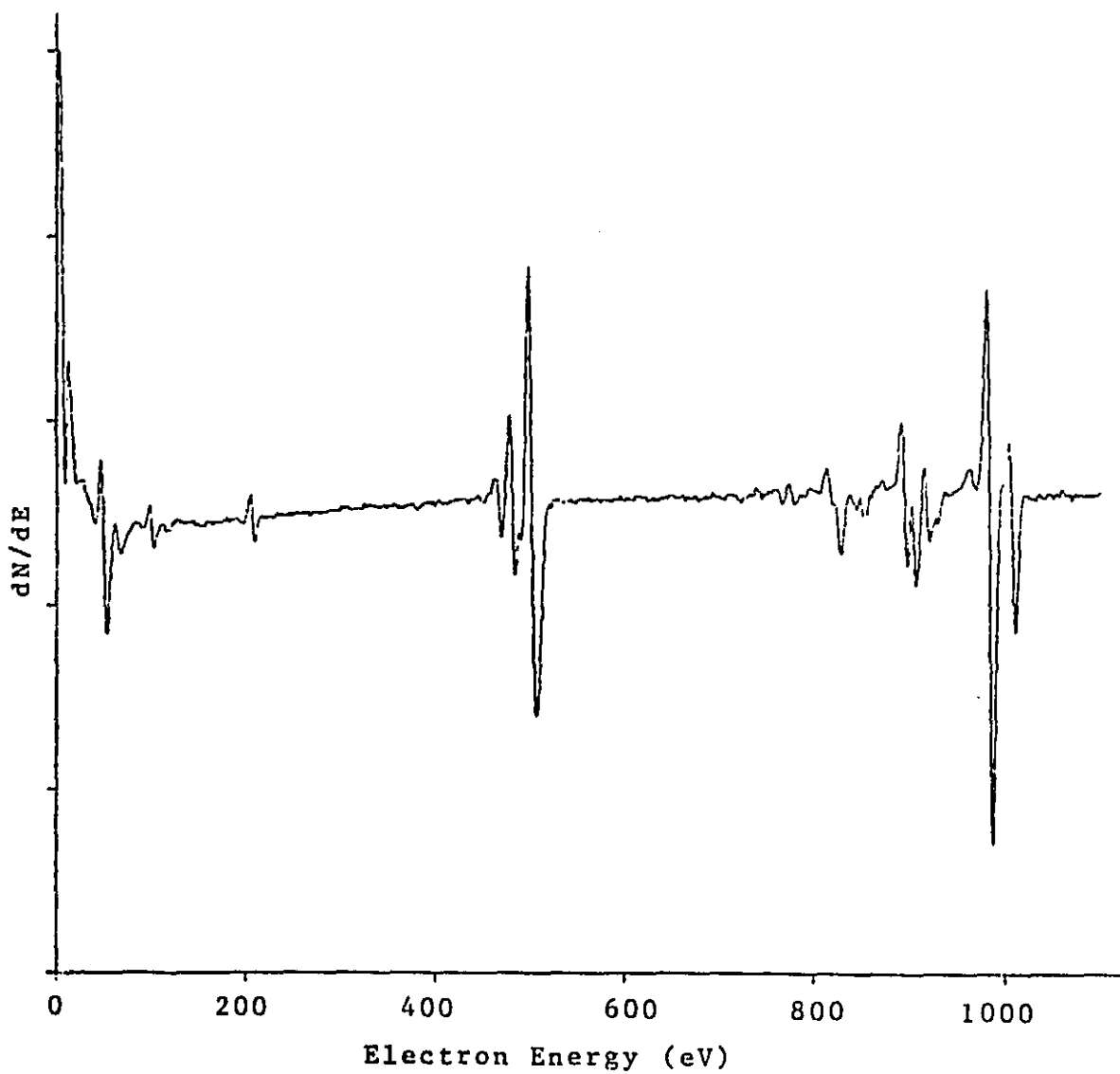


Figure 5.8 - Auger analysis of the low temperature film after four and one half minutes of the depth profile.

ORIGINAL PAGE IS  
OF POOR QUALITY.

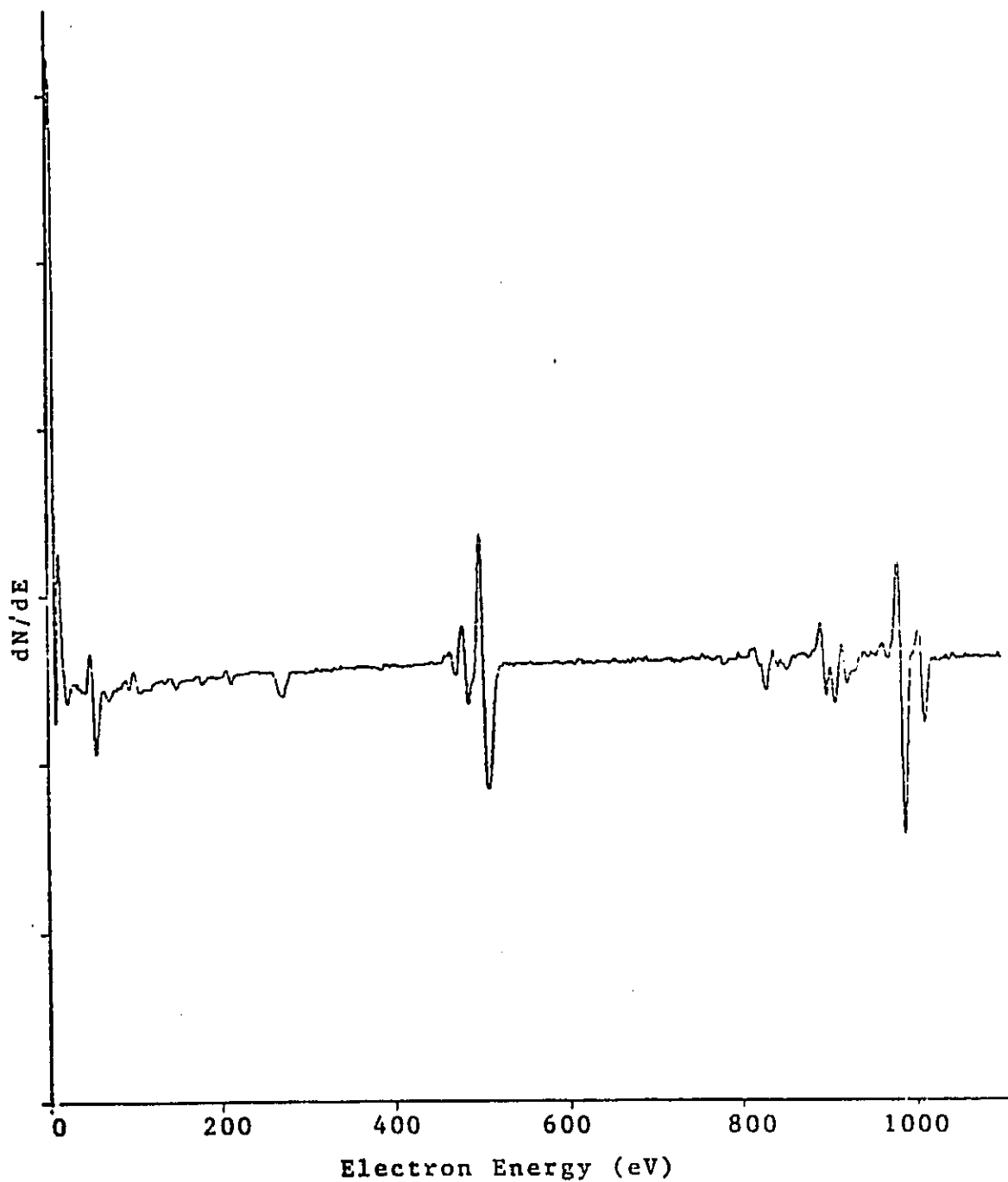


Figure 5.9 - Auger analysis of the high temperature film after four and one half minutes of the depth profile.

ORIGINAL PAGE IS  
OF POOR QUALITY

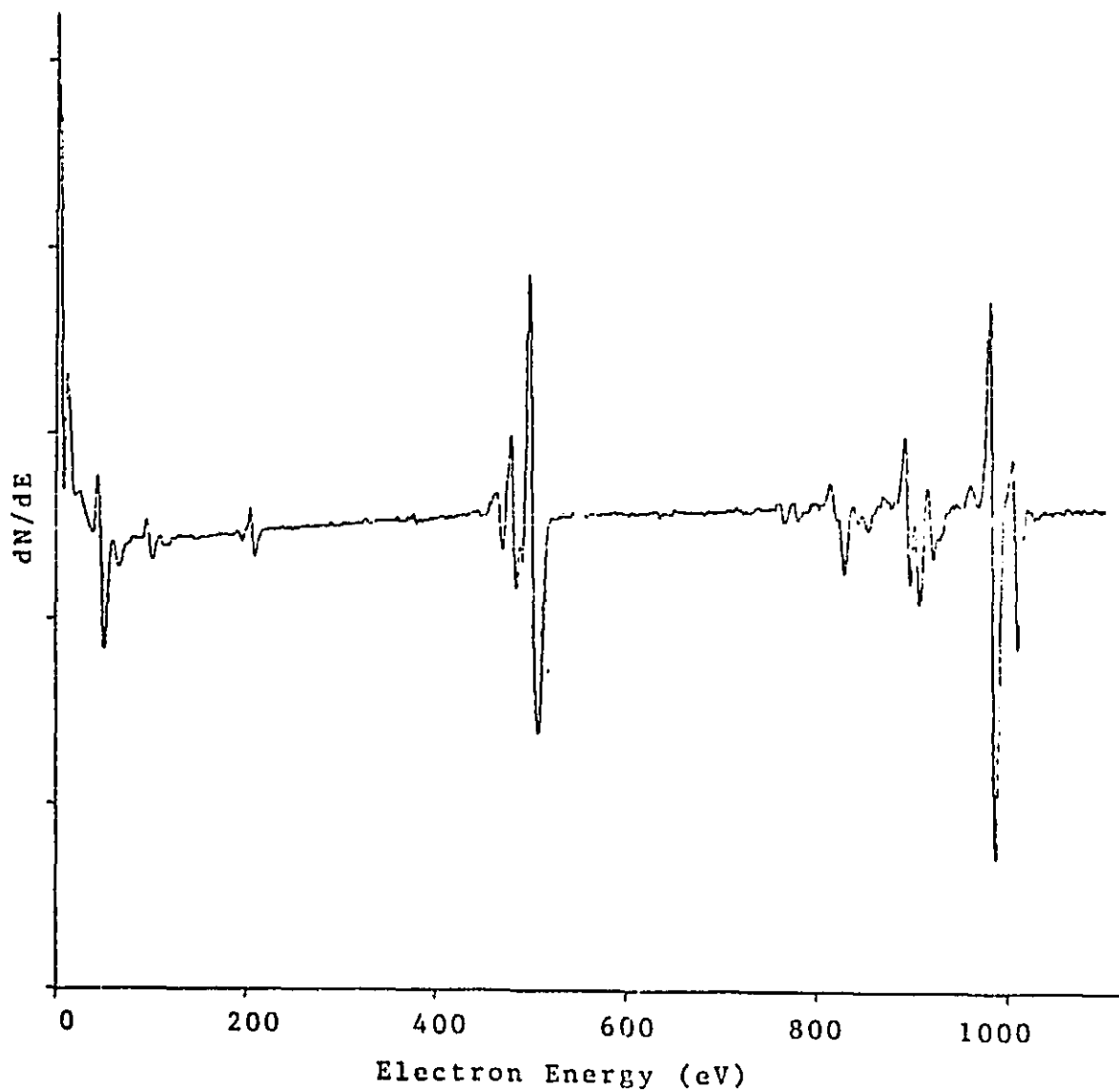


Figure 5.10 - Auger analysis of the low temperature film upon completion of the depth profile.

ORIGINAL PAGE IS  
OF POOR QUALITY

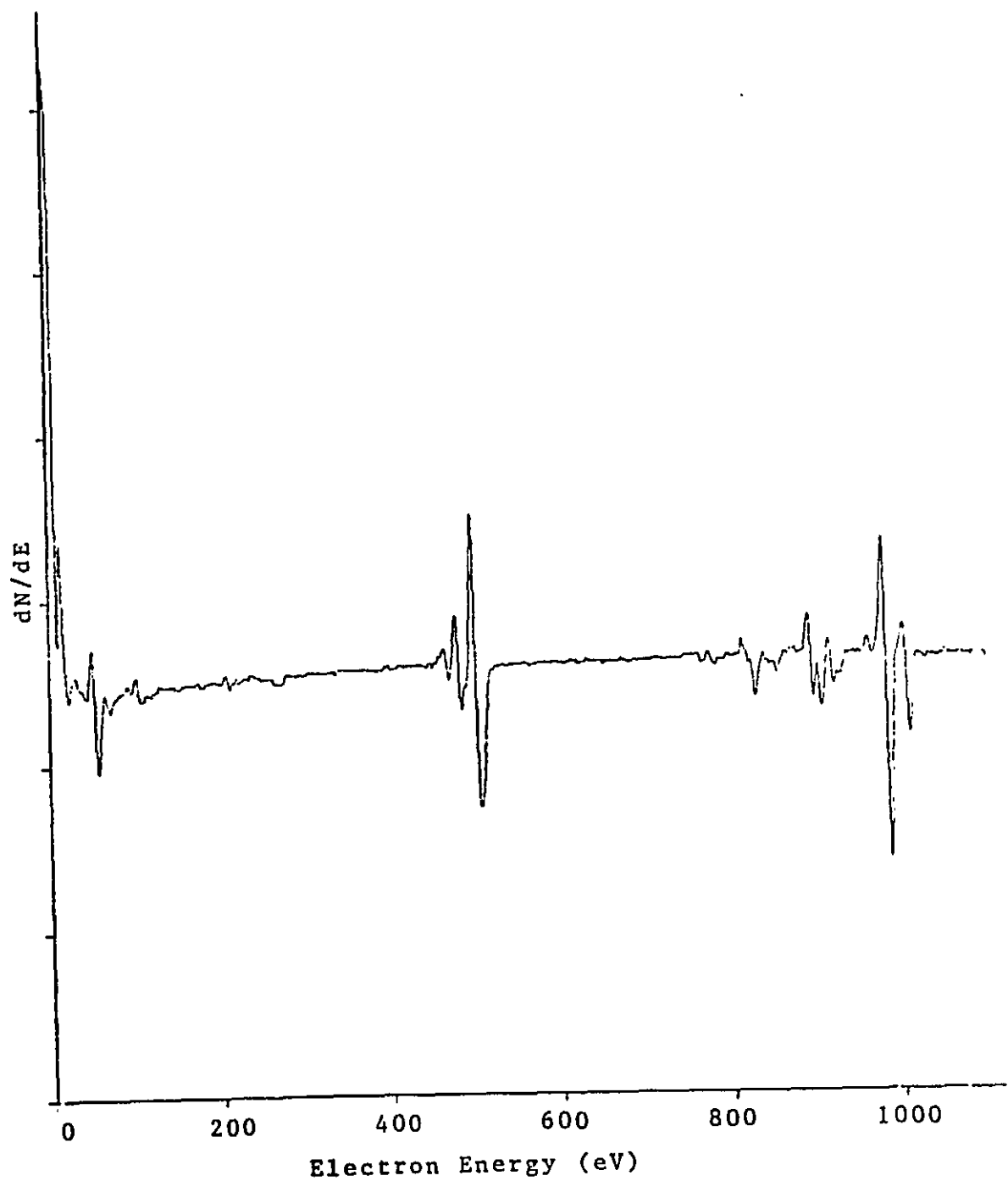


Figure 5.11 - Auger analysis of the high temperature film upon completion of the depth profile.

ORIGINAL PAGE IS  
OF POOR QUALITY

can no longer sustain a plasma. This pressure is normally lower in those systems which provide some form of RF excitation.

The argon-ion system, being of the DC type, functions best in the range of  $10^{-4}$  Torr (as measured from the upper baseplate). For pressures less than  $2 \times 10^{-4}$  Torr, the beam current begins to fall off rapidly, making it difficult to maintain a plasma below  $8 \times 10^{-5}$  Torr. For pressures greater than  $4 \times 10^{-4}$  Torr, the mean free path in the ion source becomes extremely short. This results in the beam current being almost independent of the gas pressure. The system is therefore limited to a practical operating range of between .1 and .4 millitorr.

Since the pressure is restricted to this rather small region it is impractical to perform an extensive study relating film quality to sputtering pressure. Fortunately, some rather general conclusions have been formulated by

Thornton in this area <sup>(17)</sup>. By observing the grain structure in metals, Thornton has been able to relate both the sputtering gas pressure and substrate temperature to film quality. He has, in effect, generalized the work of Vincent. The main conclusion of his work is that a lower sputtering pressure gives a larger temperature range over which dense, well ordered films will be formed and that such

structures occur at lower substrate temperatures . A pictorial representation of these results is given in Figure 5.12.

These claims are supported by films produced with the argon-ion sputtering unit. Sputtering at a pressure of  $2 \times 10^{-4}$  Torr and a substrate temperature of 270 degrees centigrade, the films pictured in Figures 5.13 and 5.14 were obtained. Figure 5.13 pictures the etched edge of a zinc oxide film. Here we observe that the acid etch has selectively attacked the film, indicating the presence of grain boundaries. These boundaries appear to be approximately 500 angstroms in size. In Figure 5.14 (the same film pictured in Figure 5.13 but away from the edge) we observe that the film exhibits a surface roughness of about 500 angstroms. By comparison, an RF magnetron system (11) (sputtering pressure 0.1 microns Hg, substrate temperature  $200^{\circ}$  C ) will produce films with an observable grain size and surface roughness of 100 angstroms. This is about one-fifth the grain size of the pictured films, indicating that the lower sputtering pressure does indeed make possible a lower sputtering temperature.

Zone A of Figure 5.12 is indicative of the structure of a film sputtered at too low a temperature. Here, as in Figure 5.3, we see the characteristic smooth surface and long striations. As the substrate temperature is increased

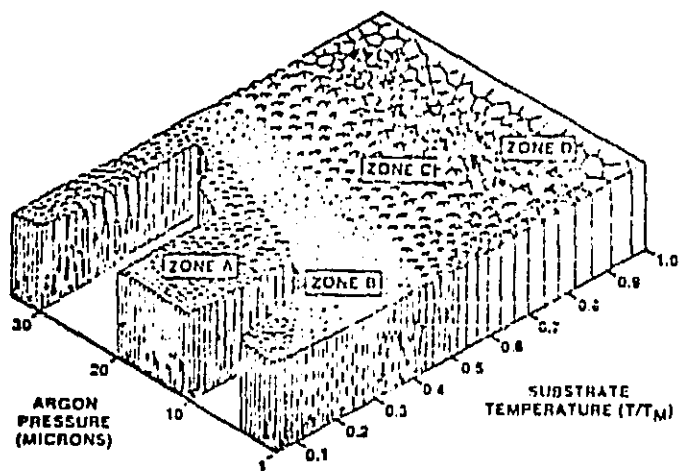


Figure 5.12 - Graphical representation of the dependence of the structure of the sputtered film on the substrate temperature and sputtering gas pressure (reprinted from (7)).

ORIGINAL PAGE IS  
OF POOR QUALITY

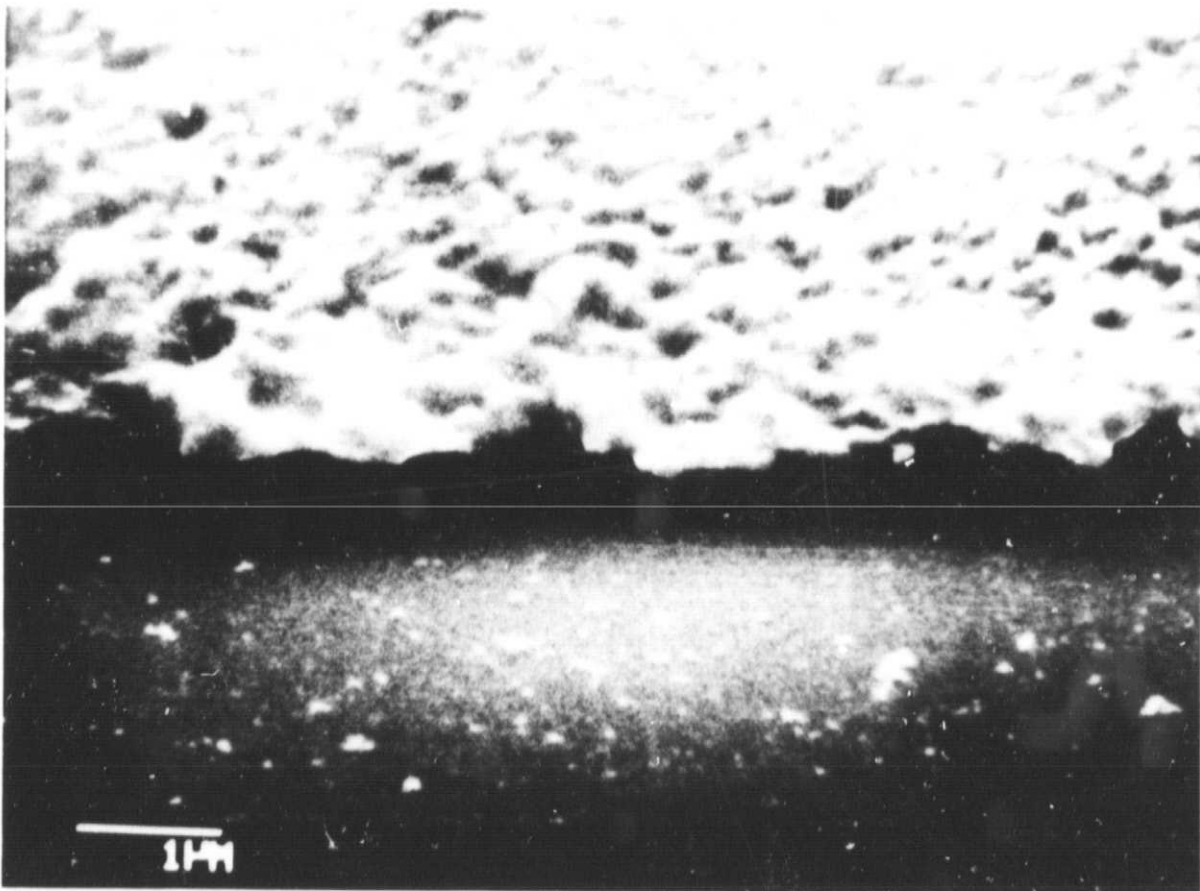


Figure 5.13 - SEM photograph of the edge of an etched zinc oxide film. Notice that the etch has selectively attacked the zinc oxide film.

ORIGINAL PAGE  
BLACK AND WHITE PHOTOGRAPH

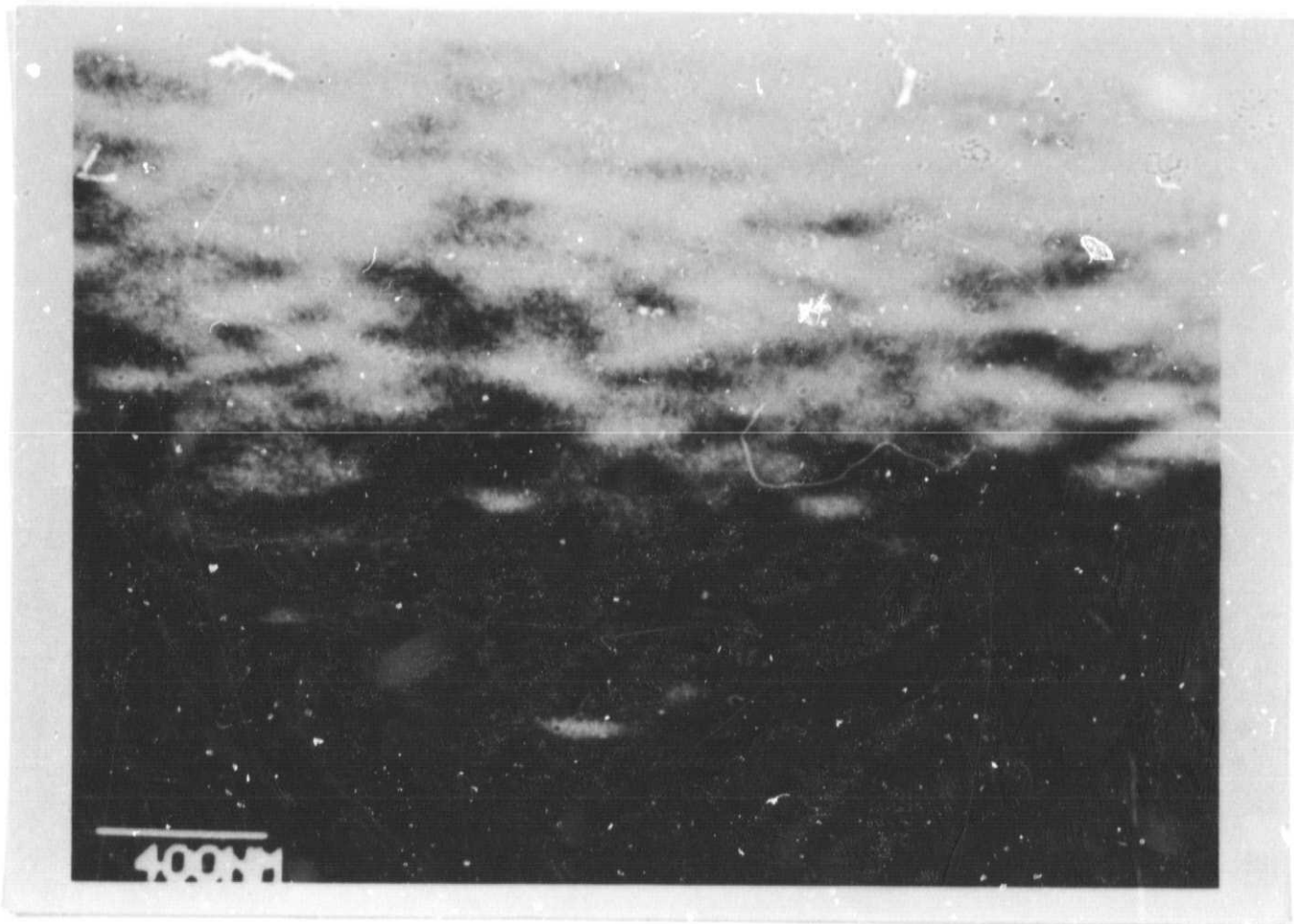


Figure 5.14 - SEM photograph of the film pictured in figure 5.13 away from the film edge. Notice the very small grain size and smooth appearance.

ORIGINAL PAGE  
BLACK AND WHITE PHOTOGRAPH

into zone B (the proper temperature range), we see that the surface remains very smooth and the striations are no longer present as in Figure 5.14. For a film sputtered at too high a temperature, zones C and D, we see that Thornton predicts a rough surface with a periodic structure. This is in good agreement with Figures 5.4 and 5.5.

#### (4) Acceleration Voltage

By varying the accelerating voltage, one is actually changing two important sputtering parameters. The first and most obvious is the beam current. The beam current (and hence the sputtering rate) is proportional to the acceleration voltage. Therefore, from a purely deposition rate point of view, the acceleration voltage should be as large as possible.

However, the sputtering yield is also dependent on the acceleration voltage. Recalling the remarks made in Section I, we expect the yield to be a rather complicated function of the acceleration voltage. Wishing to maximize the sputtering rate and therefore minimize the sputtering time, it is obvious that the acceleration voltage should be adjusted so as to maximize the yield.

Figure 5.15 and Table 5.3 show the sputtering rate of the system as a function of the acceleration voltage. Since the data is for a constant arc current (1A), it is actually

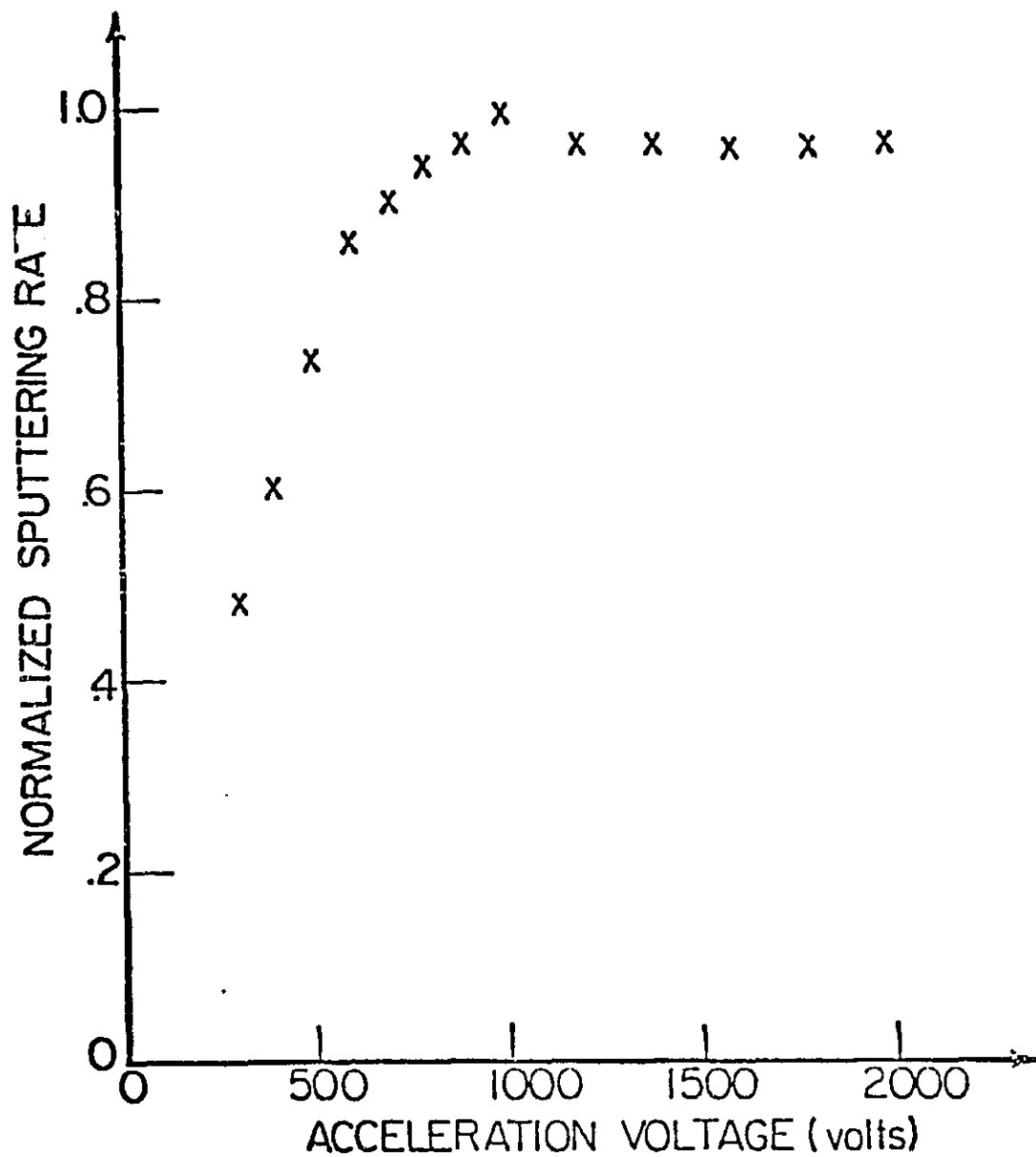


Figure 5.15 - Graph showing the sputtering rate versus the acceleration voltage for a constant arc current (1A).

ORIGINAL PAGE IS  
OF POOR QUALITY

Acceleration Voltage (Kilovolts)	Film Thickness (Angstroms)	Sputtering Rate (Angstroms/Second)
300	114	.380
400	143	.477
500	175	.583
600	206	.687
700	214	.713
800	224	.747
900	230	.767
1000	238	.793
1200	230	.767
1400	230	.767
1600	232	.773
1800	232	.773
2000	231	.770

Table 5.3 - Data for Figure 5.15. Each film was sputtered for 5 minutes with a 1A arc current.

a graph of the dependence of the sputtering yield on the acceleration voltage. Once again referring to Section I, we see that the curve exhibits the expected shape. It is linear for voltages from 300 to 1000 volts and is essentially constant for voltages above 1000 volts. The other two regions (exponential just above threshold and decreasing for high voltages) are beyond the range of the system. For voltages below 300 volts, the ion beam will lose its collimation, resulting in excessive etching of the grid assembly.

In light of this, voltages of 1000 volts and greater should be used. A voltage of 1000 volts is usually adequate, resulting in a beam current near the system maximum of 200mA.

## VI The Effect of Post-Deposition Annealing on Film Quality

After deposition each zinc oxide film is annealed at 550 °C in a diffusion furnace with a pure oxygen ambient for 1/2 hour. It was initially believed that this post-deposition annealing process was essential in yielding a high resistivity, crystalline film. However, recent films have shown the proper piezoelectric properties without annealing. It therefore became necessary to determine the nature of the annealing process.

The dependence of the substrate resistivity on the annealing temperature is shown in Figure 6.1 and Table 6.1. Prior to annealing each of the films exhibited a sheet resistance on the order of 10 kilohms per square as measured with a four point probe. These films have a relatively low sheet resistance, probably due to a slight misalignment of the system while sputtering. After annealing, little change was noted in those films annealed below 200 °C. For annealing temperatures between 200 and 600 °C, the substrate resistivity increases rapidly with temperature. As the annealing temperature is varied from 600 to 900 degrees the resistivity becomes nearly independent of the annealing temperature. For temperatures of 1000 degrees centigrade and higher the bonding between the ZnO and the substrate is broken, destroying the film.

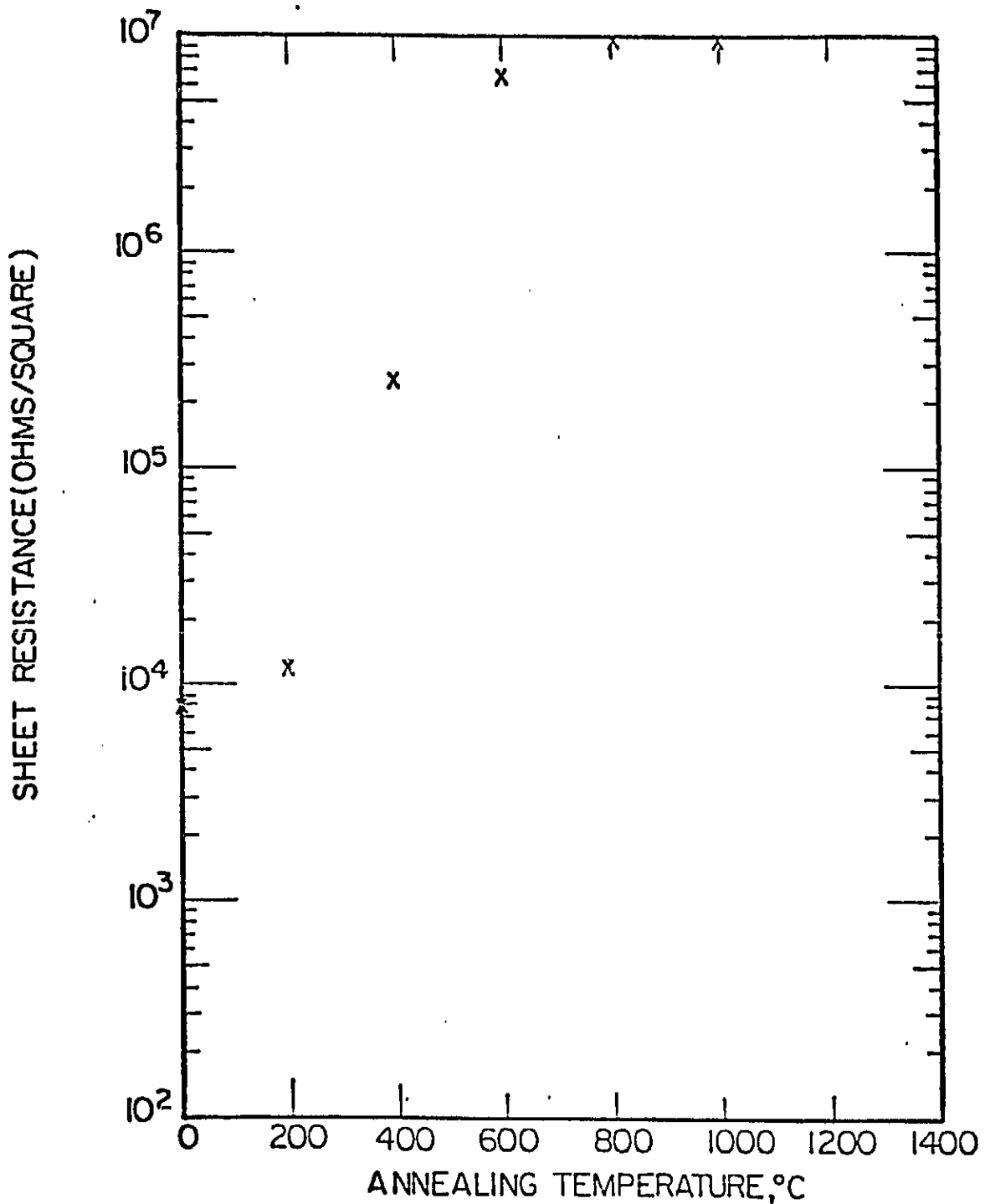


Figure 6.1 - Graph showing the zinc oxide sheet resistance as a function of the annealing temperature. Notice that the curve begins to level off for temperatures above 600 C.

ORIGINAL PAGE IS  
OF POOR QUALITY

Temperature ° C	V (Volts)	I (Amps)	R (Ohms/Square)
0	-.170	25.5 $\mu$	8.95K
200	-.195	39.5 $\mu$	22.7K
400	-.773	13.8 $\mu$	253K
600	-.038	76.0n	6.62M
800	-.069	31.5n	9.93M
1000	-.031	14.0n	10.0M

Table 6.1 - Data for Figure 6.1.

To determine the source of the increase in resistivity an Auger analysis and depth profile were performed on annealed and unannealed films. For this analysis a 0.6 micron film was sputtered on silicon dioxide. (It is necessary to use very thin films to prevent electrostatic charging problems during the Auger analysis.) One of the resulting films was annealed, the other left unannealed. The results of this analysis are shown in Figures 6.2 through 6.11.

Figure 6.2 presents the Auger analysis results for the unannealed film after the completion of the depth profile. By comparison with the Auger electron spectroscopy data in Appendix B, three elements can be identified; carbon, oxygen, and zinc.

The presence of zinc and oxygen in the film are, of course, expected. The carbon is most likely due to the diffusion pump oil.

The Auger analysis of the annealed film after the depth profile is shown in Figure 6.3. By comparison with Figure 6.2, we see that the two films are, within the resolution of the machine, virtually identical as far as bulk composition. This conclusion is substantiated by Figures 6.4 through 6.7 which show expanded versions of a zinc and oxygen peak for both films. Again the results are remarkably similar.

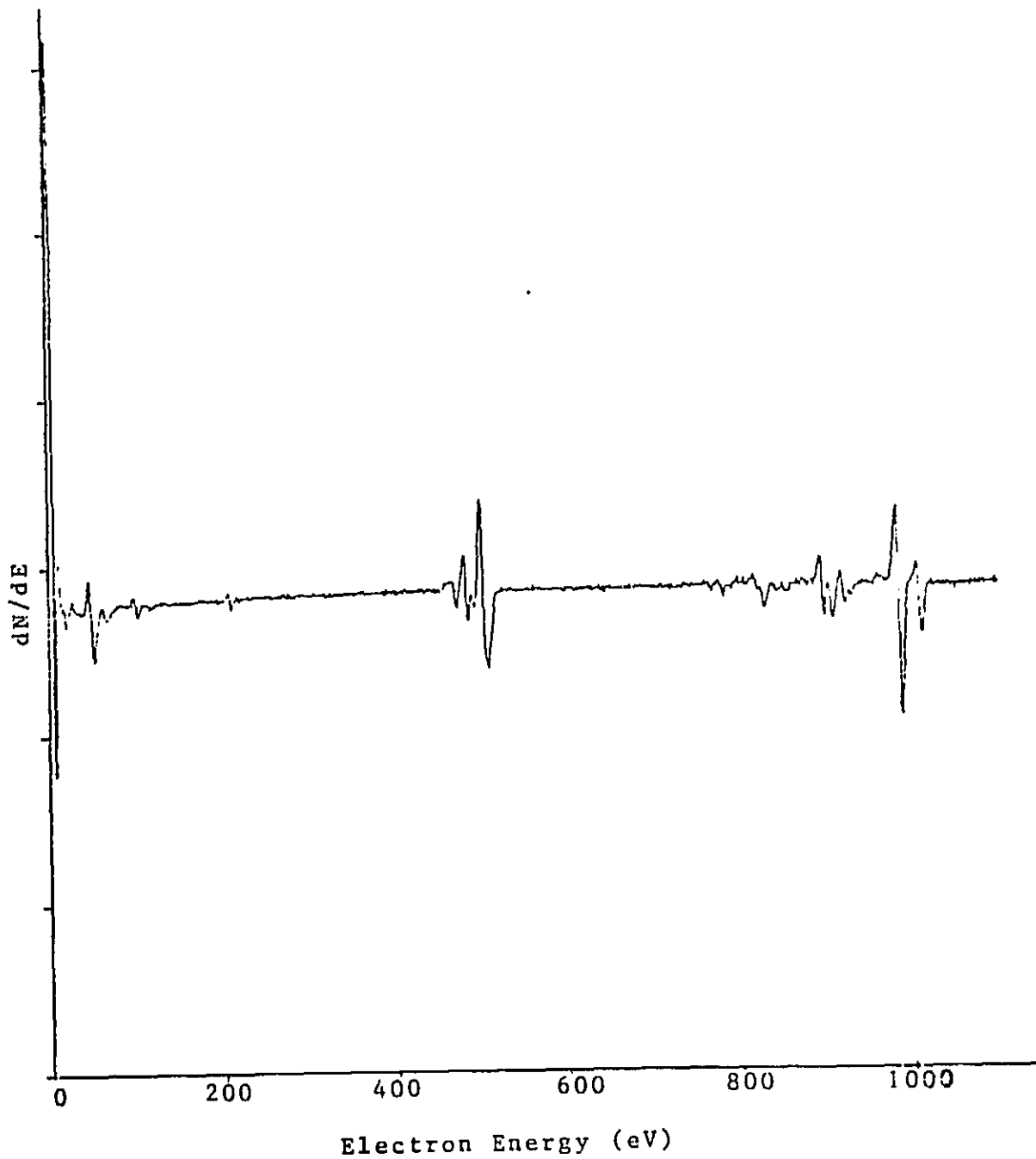


Figure 6.2 - Auger analysis of the unannealed film after completion of the depth profile.

ORIGINAL PAGE IS  
OF POOR QUALITY

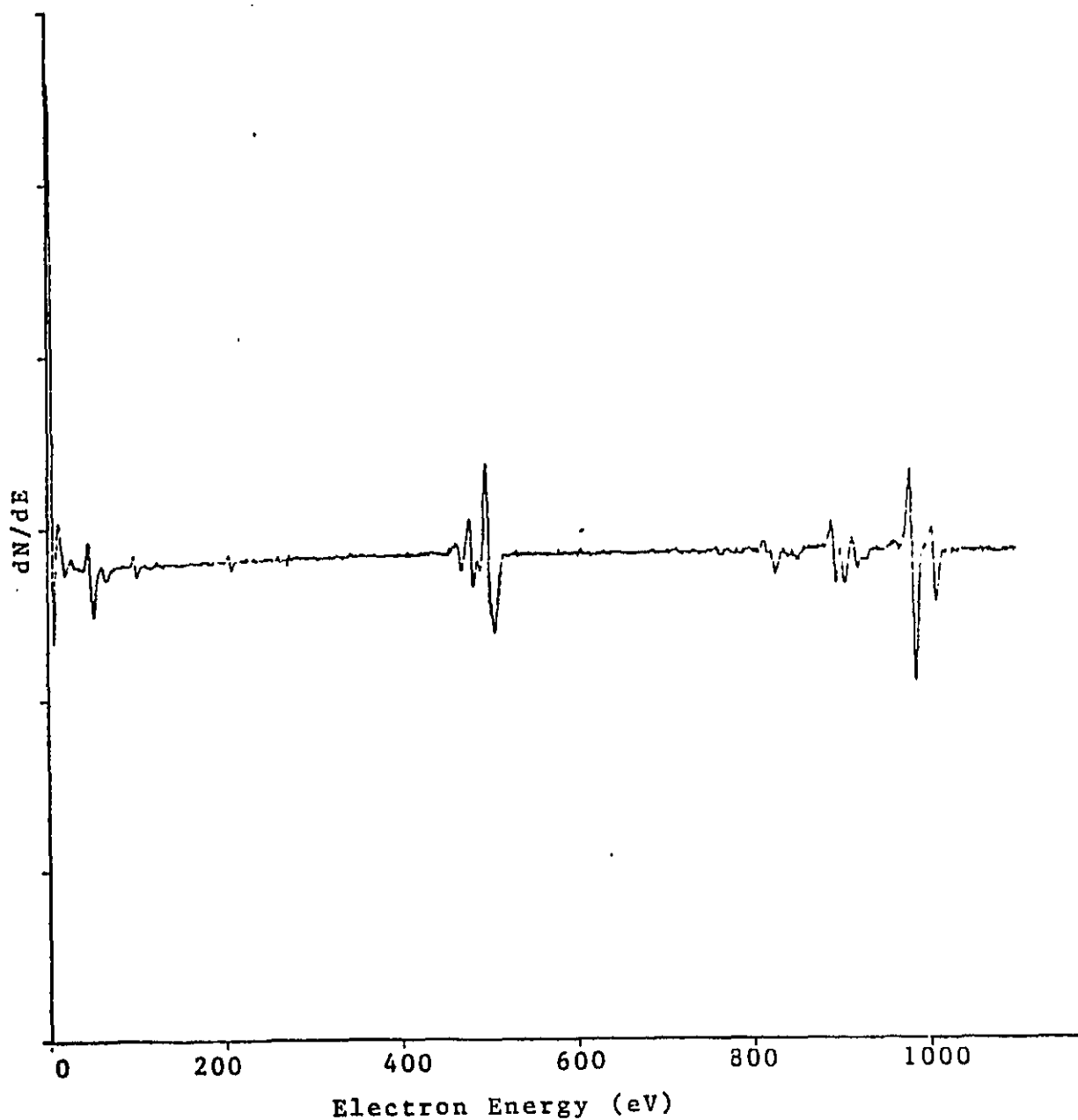


Figure 6.3 - Auger analysis of the annealed film after completion of the depth profile. Notice the similarity to Figure 6.2.

ORIGINAL PAGE IS  
OF POOR QUALITY

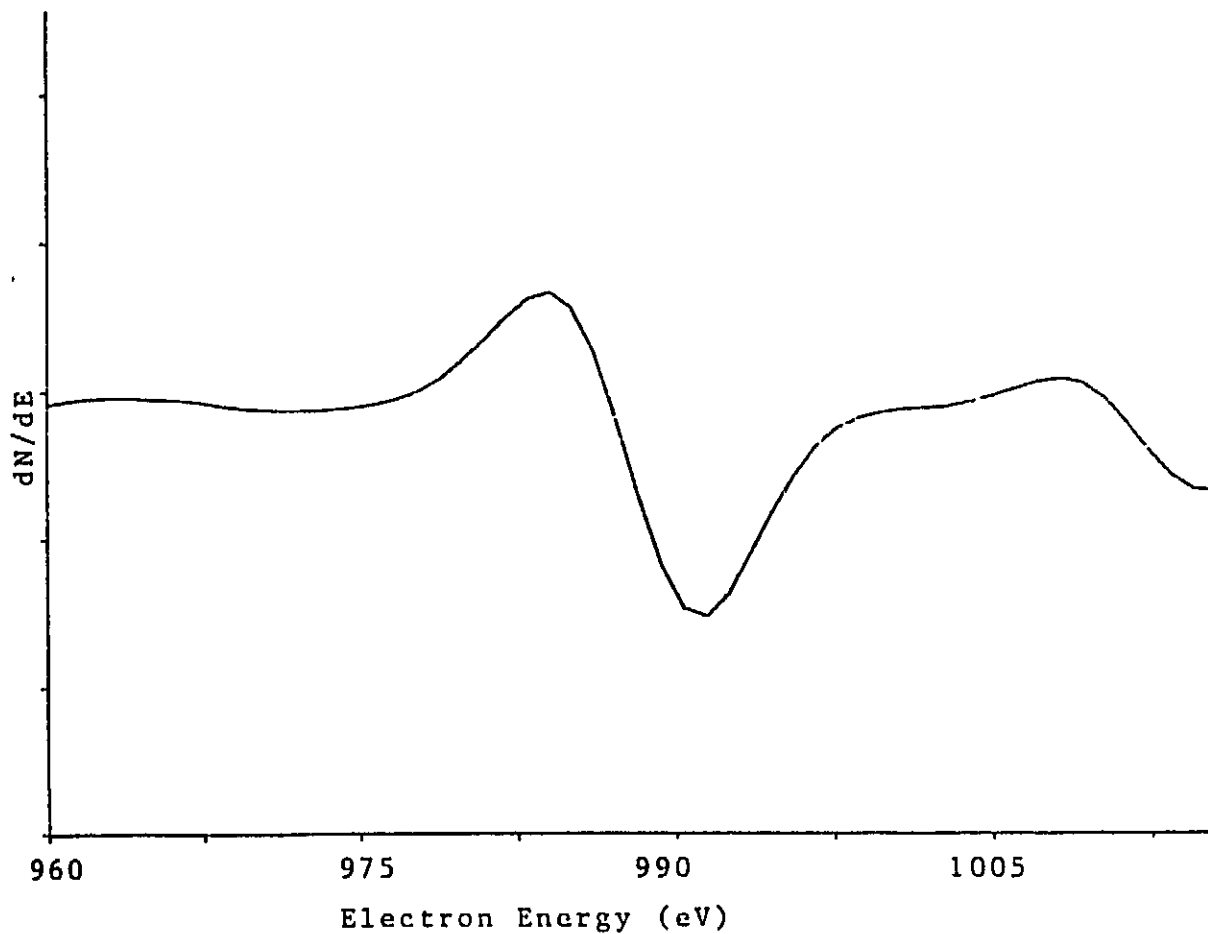


Figure 6.4 - Expanded version of the zinc peaks for the unannealed film.

ORIGINAL PAGE IS  
OF POOR QUALITY

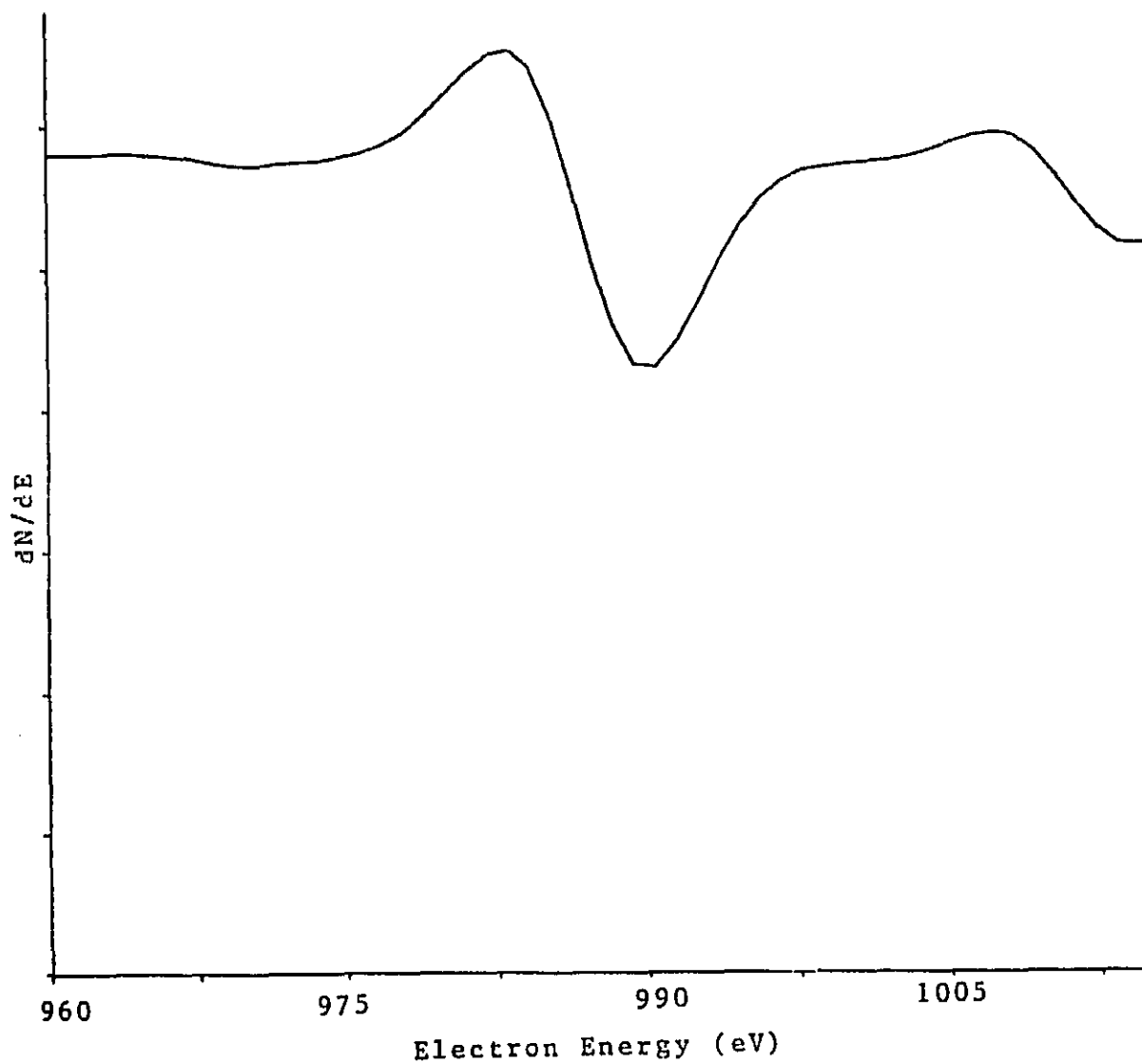


Figure 6.5 - Expanded version of the zinc peak for the annealed film.

ORIGINAL PAGE IS  
OF POOR QUALITY

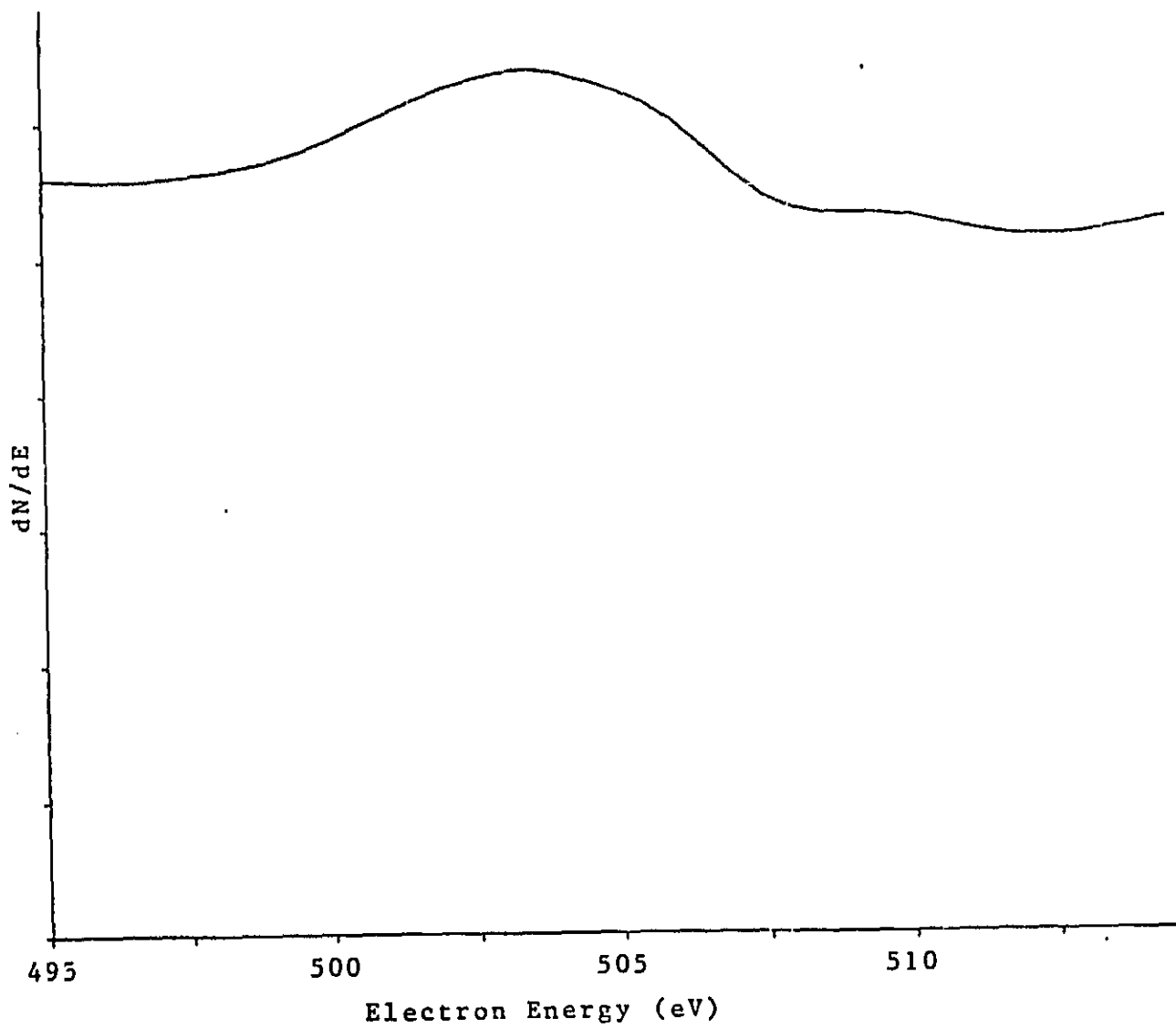


Figure 6.6 - Expanded version of the oxygen peak for the unannealed film.

ORIGINAL PAGE IS  
OF POOR QUALITY.

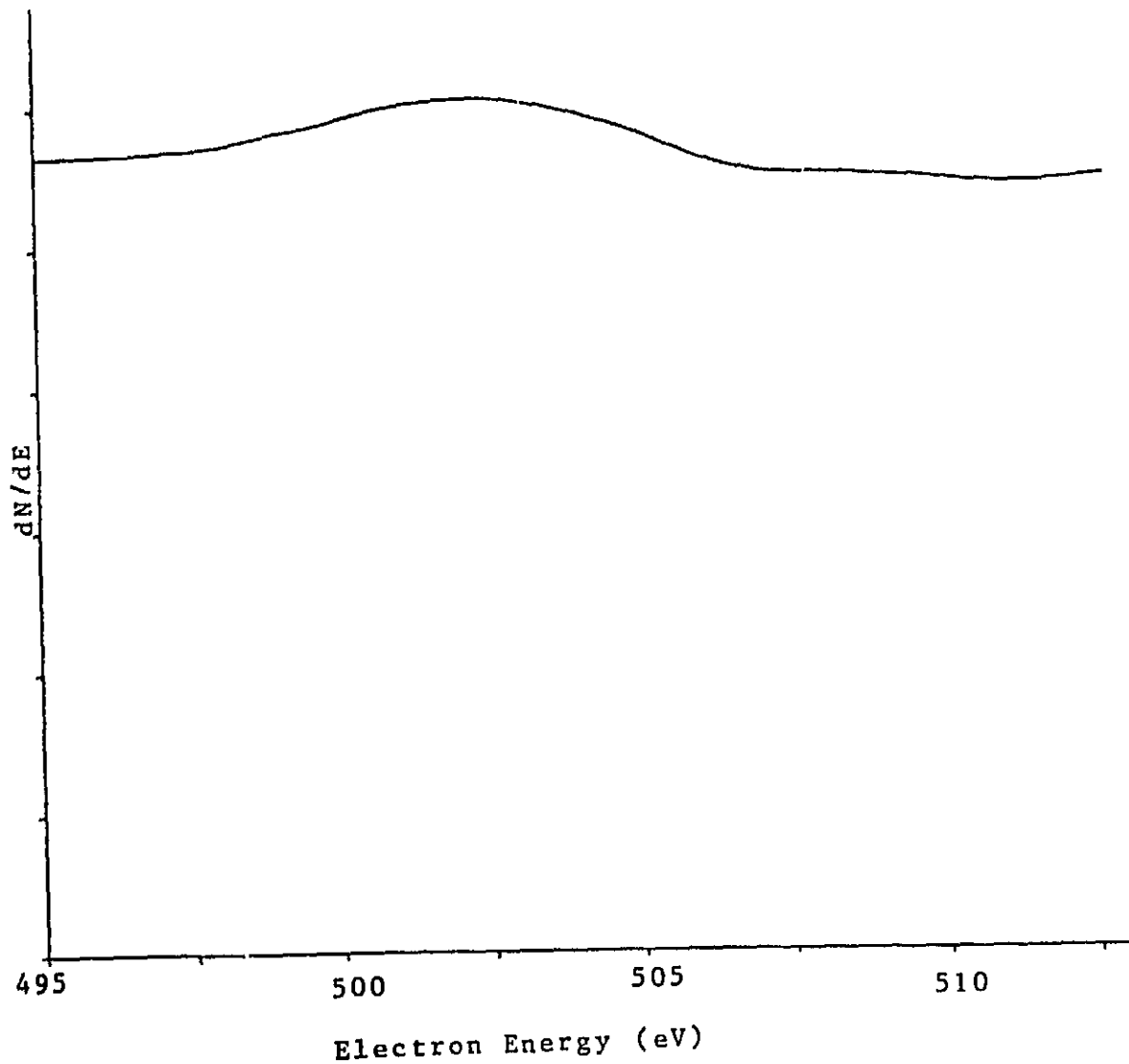


Figure 6.7 - Expanded version of the oxygen peak for the annealed film after completion of the depth profile.

ORIGINAL PAGE IS  
OF POOR QUALITY.

The source of the increased resistivity is readily explained via the depth profile, the results of which are shown in Figures 6.8 through 6.11. Figures 6.8 and 6.9 present the variation in the peak height of zinc, oxygen, and carbon peaks as a function of the profile time. Using an average sputtering rate of 30 angstroms per second, this corresponds to a depth profile of approximately three hundred angstroms. From Figure 6.8, we see that the unannealed film shows a relatively constant concentration of zinc, oxygen, and carbon over the entire profile. For the annealed film (Figure 6.9) during the first four minutes sputtering time the zinc concentration is significantly less than the bulk value. Over the same range the carbon content increases slightly and the oxygen content remains relatively constant. This change in surface concentration is again shown in Figures 6.10 and 6.11 where the average concentrations are plotted.

At first this may appear to be a relatively small change in the zinc concentration to account for such a large change in conductivity. However, it must be remembered that the film is largely composed of zinc which is already bound to oxygen. These bound zinc atoms are not those that participate in conduction. It is the free zinc which is contributing to the relatively high conductivity. Since the ratio of ZnO to free zinc is presumably very large, a substantial change in the amount of free zinc present, and hence the conductivity, will appear as a relatively small

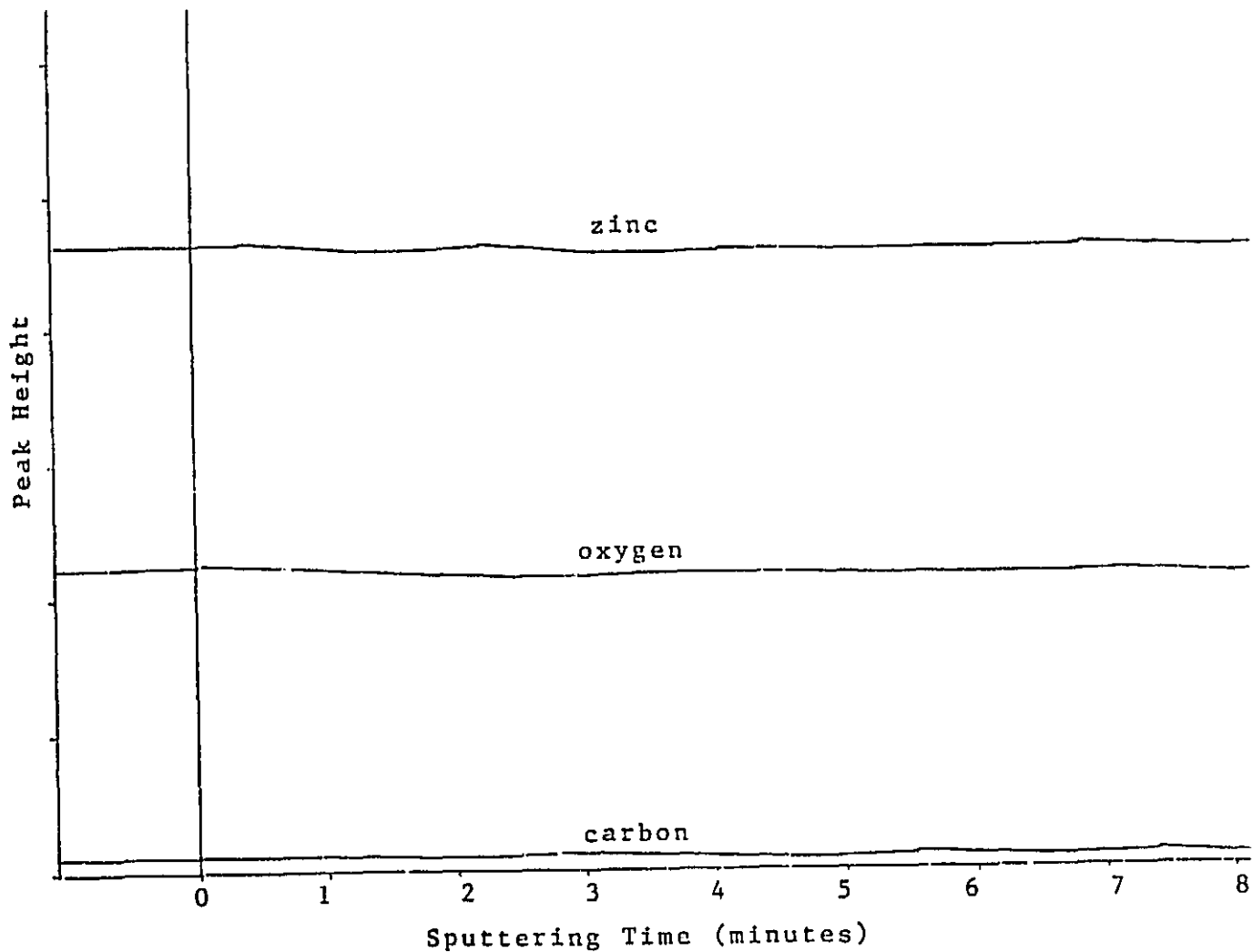


Figure 6.8 - Variation in the height of zinc, carbon, and oxygen peaks as a function of the profile time for the unannealed film.

ORIGINAL PAGE IS  
OF POOR QUALITY

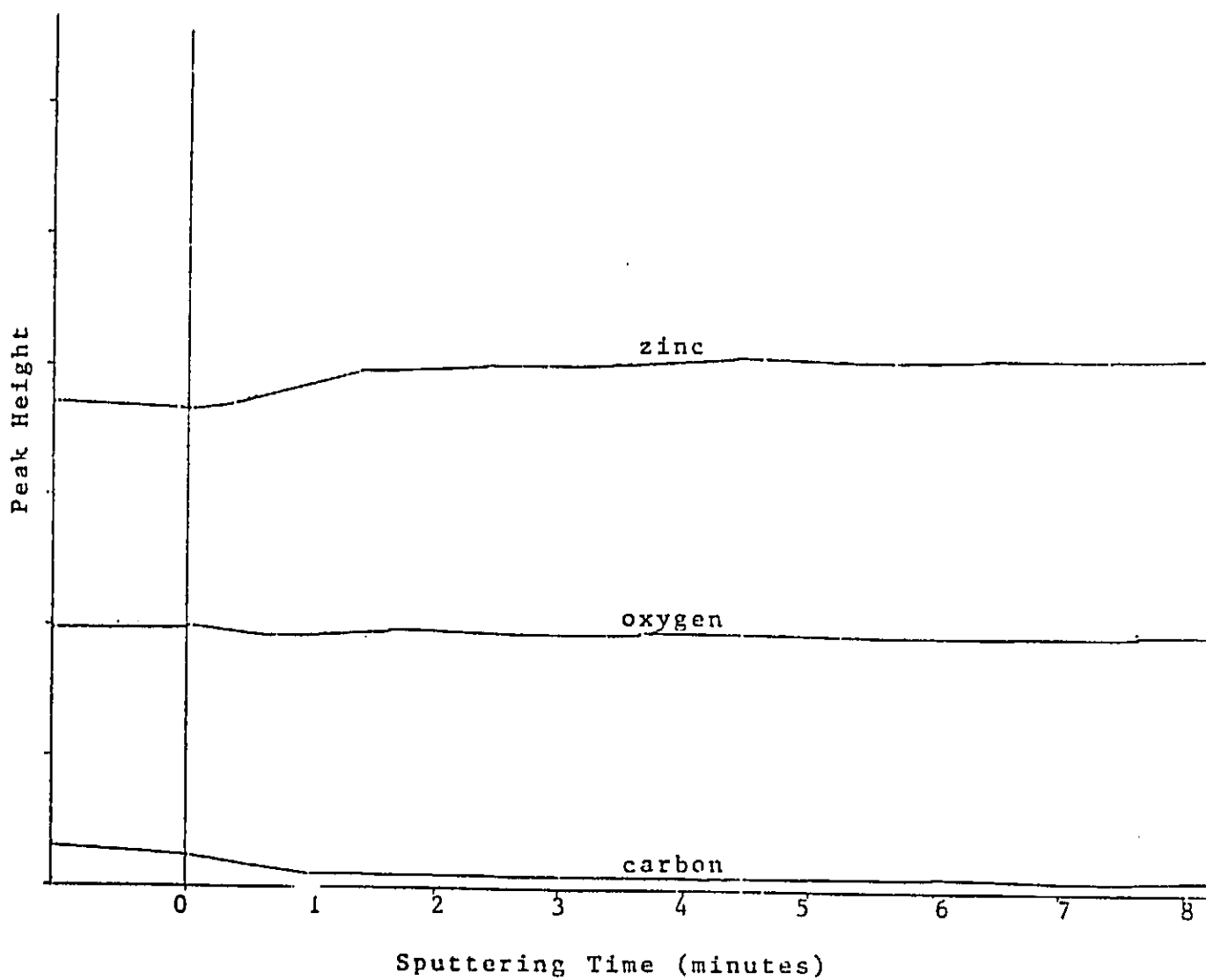


Figure 6.9 - Variation in the height of zinc, carbon, and oxygen peaks as a function of the profile time for the annealed film.

ORIGINAL PAGE IS  
OF POOR QUALITY

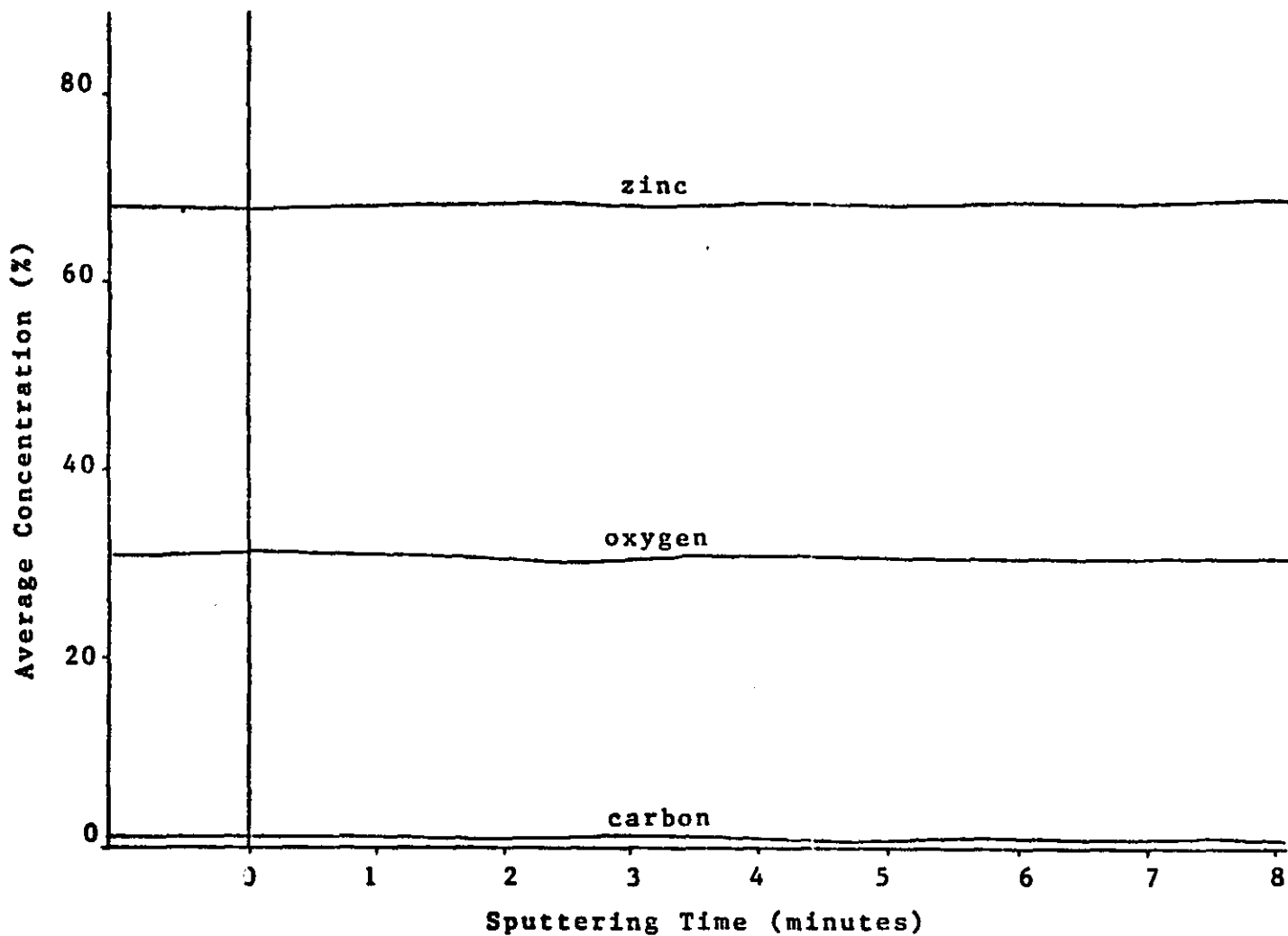


Figure 6.10 - Variation in the average concentration of zinc, carbon, and oxygen as a function of the profile time for the unannealed film.

ORIGINAL PAGE IS  
OF POOR QUALITY

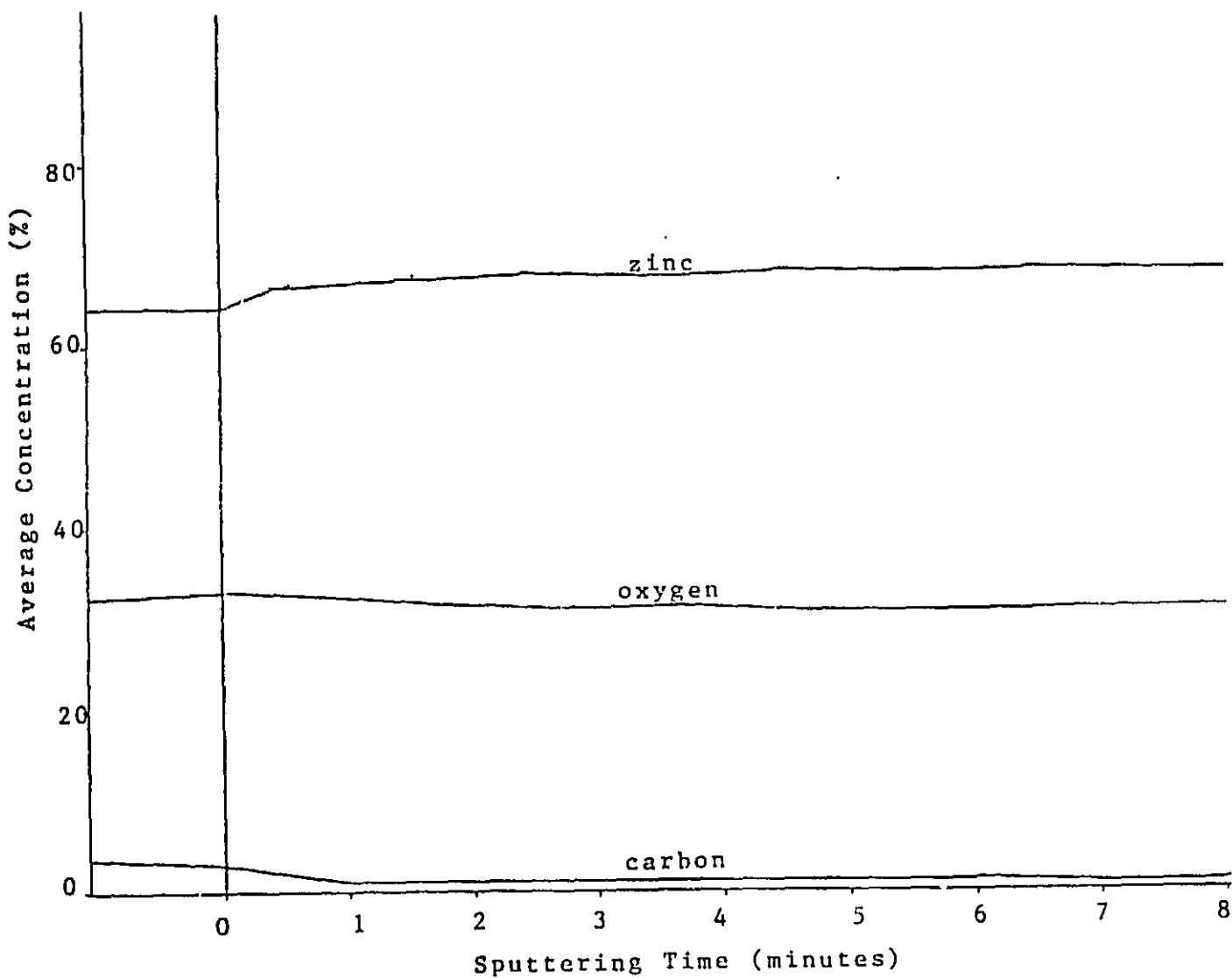


Figure 6.11 - Variation in the average concentration of zinc, carbon, and oxygen as a function of the profile time for the annealed film.

change in the total percentage of zinc in the film.

This is in sharp contrast to the normal relationship between carrier concentration and conductivity in, for example, a semiconductor. In that case, the impurity elements (the ones that participate in conduction such as boron or phosphorous) are different from the host atoms. Then the conductivity is indeed proportional to the concentration of the element which is acting as the charge carrier (as long as extreme doping levels are avoided).

To determine the effect of the annealing process on the crystalline structure of the ZnO an x-ray diffraction analysis was performed on each of the above films.

Schoenwald et. al. <sup>(18)</sup> have shown that this analysis technique provides a quick and non-destructive evaluation of film quality, directly relating the piezoelectric properties of the film to x-ray diffraction patterns.

This method involves determining the scattering intensity from the crystallographic planes of the film as a function of the scanning angle of an x-ray beam. From the theory of Bragg diffraction it is known that this angle is related to the separation between planes by

$$2d\sin(\theta) = n\lambda$$

where d is the separation between the crystal planes,  $\lambda$  is

the wavelength of the x-ray, and  $n$  is an integer. The angular dependence of the scattering intensity can then be compared to the spectra obtained from bulk single-crystal zinc oxide to determine the relative crystallinity of the film.

Ideally, the results for first order diffraction should show a single peak at theta (for ZnO, this is 17.25 degrees) and zero everywhere else. In actuality a well ordered film will yield a large peak over a small angular span, falling off by a factor of five to ten within one degree of the maximum. In general, the higher and narrower the peak the better.

The result of this analysis for the unannealed film is shown in Figure 6.12. While this film does exhibit a peak at  $17.25^\circ$ , it has a rather large width of about 4 degrees. This indicates the presence of a strain and a small particle size. In addition, there are spurious peaks present at  $14^\circ$  and  $15.3^\circ$ .

From Figure 6.13 it is apparent that the annealing process has improved matters drastically. The width of the curve has decreased to approximately one half its original value. In addition, the peak present at  $15.3^\circ$  has decreased in size by 50% while the peak at  $14^\circ$  has almost disappeared.

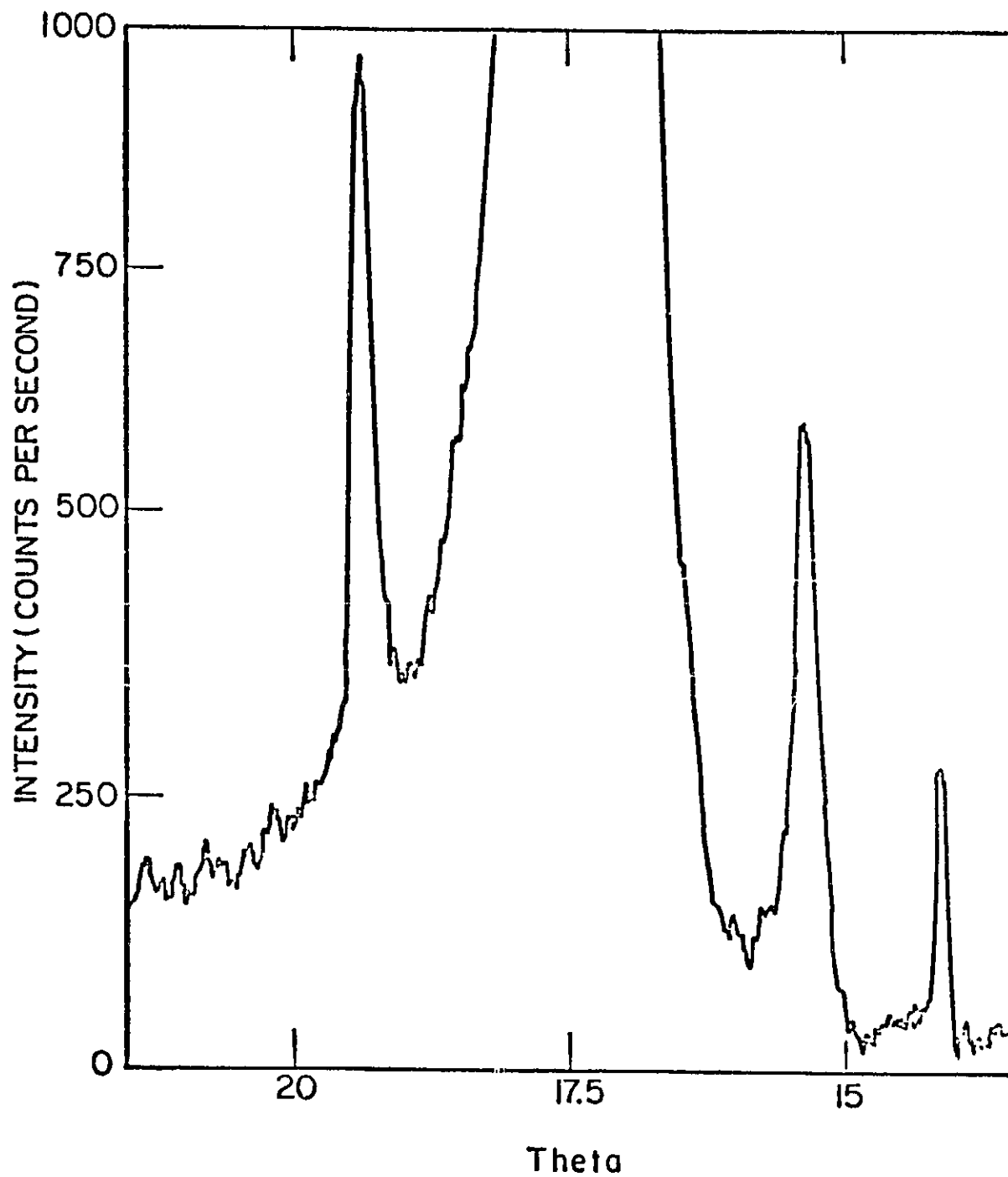


Figure 6.12 - Results of the diffraction analysis for the unannealed film. The graph presents the intensity as a function of the scanning angle.

ORIGINAL PAGE IS  
OF POOR QUALITY

Both of these changes indicate possible strain relief and an increase in the particle size due to annealing.

Since piezoelectricity is diminished by conductivity and enhanced by crystallinity, one might expect the annealing process to yield an increase in the piezoelectric properties of the film. To determine if this is indeed the case, a pair of aluminum interdigital transducers <sup>(19)</sup> was deposited on each film after annealing .

These transducers allow for the generation and detection of elastic surface waves within the film. Each transducer consists of a series of parallel metal lines periodically spaced on the substrate and connected as shown in Figure 6.14. Here we see that the transducer is a two terminal device with alternating electrodes interconnected. When a voltage is applied to these terminals electric fields are generated within the substrate. These fields will excite stress patterns within the film via the piezoelectric effect. If the applied voltage alternates at the proper frequency (see Appendix C), then surface acoustic waves will be launched in both directions normal to the transducer.

Detection of the surface wave is achieved with a second transducer. As the acoustic wave passes under the receiving transducer the piezoelectric effect will cause the elastic stress to be converted back to an electrical voltage which is then displayed on an oscilloscope. Using a pulsed 30MHz

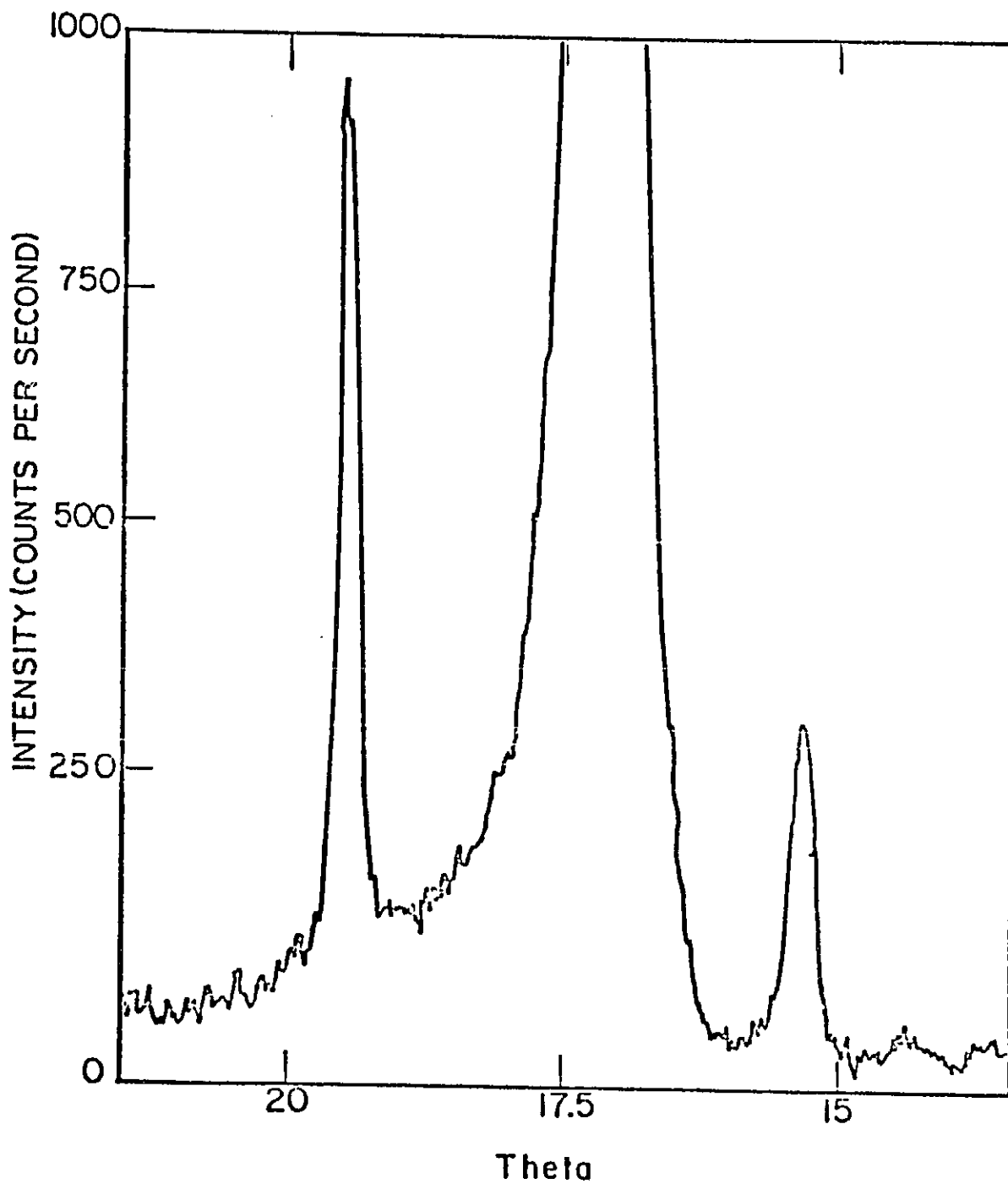


Figure 6.13 - Results of the diffraction analysis for the annealed film. The graph presents the intensity as a function of the scanning angle.

ORIGINAL PAGE IS  
OF POOR QUALITY

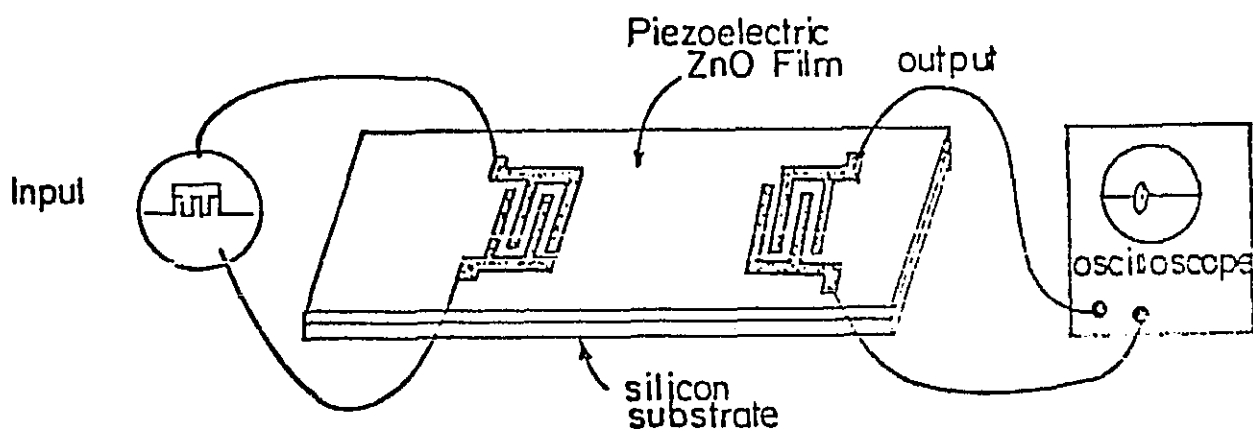


Figure 6.14 - Surface acoustic wave insertion and detection apparatus.

ORIGINAL PAGE IS  
OF POOR QUALITY.

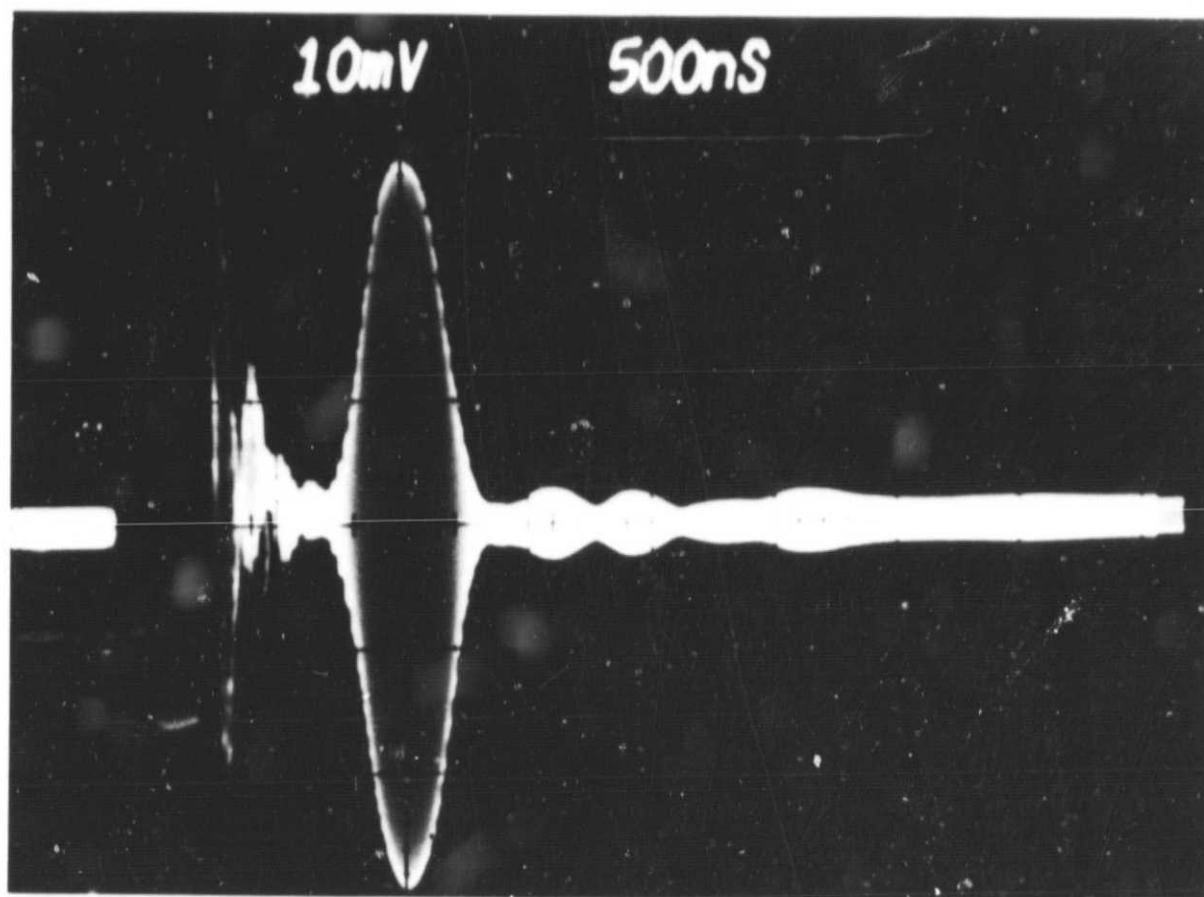


Figure 6.15 - Picture of the acoustic response of the zinc oxide film. The large pulse to the left is a feedthrough signal. The second, smaller pulse is the acoustic signal.

ORIGINAL PAGE  
BLACK AND WHITE PHOTOGRAPH

ORIGINAL PAGE  
~~BLACK AND WHITE PHOTOGRAPH~~

source, a typical surface acoustic wave output is shown in Figure 6.15 . These surface waves, as well as the interdigital transducer, are discussed further in Appendix C.

Figure 6.16 shows the dependence of the acoustic signal strength on the annealing temperature. Here we see that the acoustic output is an increasing function of the annealing temperature. We also observe that Figures 6.1 and 6.16 have essentially the same shape; increasing for temperatures below 600 degrees and constant for temperatures above 600 degrees. This tends to point to 600 °C as an effective upper limit for the annealing temperature.

The 600 °C point is an upper limit in another sense also. Since the ultimate goal of the ZnO technology is to integrate it with the existing silicon technology to create monolithic devices, the zinc oxide deposition procedure must not be detrimental to any active circuitry. Because the substrate will normally have been metalized prior to film deposition and annealing, this places an upper limit on the annealing temperature of 577 degrees. Above this point silicon and aluminum will form a eutectic alloy, rapidly destroying any active devices .

(20)

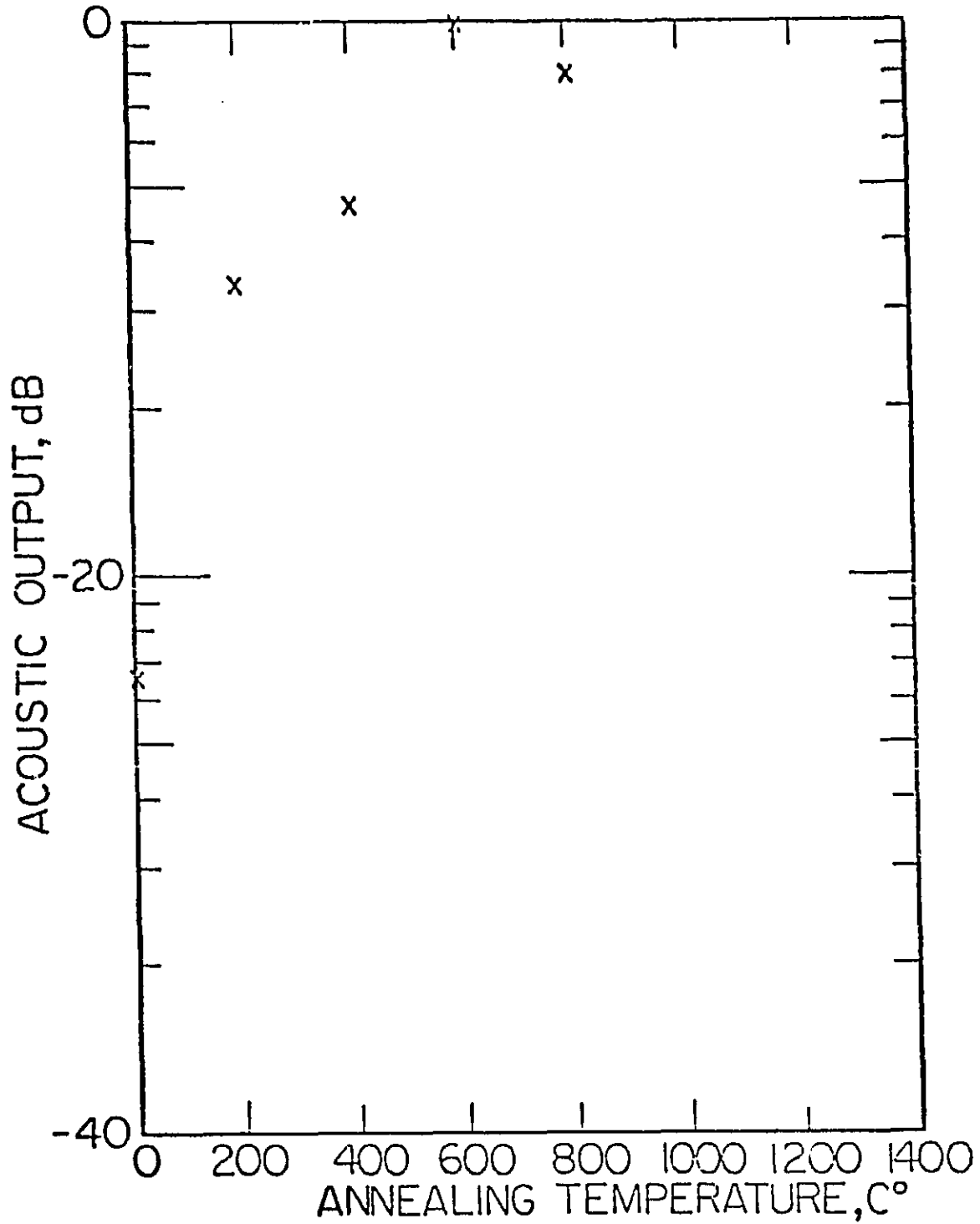


Figure 6.16 - Graph of surface acoustic wave amplitude versus the annealing temperature of the film. Notice that the curve begins to level off above 600 C.

ORIGINAL PAGE IS  
OF POOR QUALITY

The annealing process has been used successfully with photodiodes overlaid with zinc oxide and annealed at temperatures up to 550 °C. Annealing temperatures in this range yield high resistivity zinc oxide films without compromising silicon device performance.

In conclusion, we see that there is a lower temperature limit of 200 °C, below which annealing has little effect on the film quality. There is also an upper limit of 600 degrees, above which there is little further beneficial effects. The increase in resistivity due to annealing is related to surface stoichiometry only. The annealing process does significantly alter the bulk crystalline properties of the film, resulting in a decrease in the strain and an increase in the particle size. the combination of these two effects enhances the piezoelectric properties of the film, indicating that the annealing process is indeed a beneficial step in the production of zinc oxide films.

Temperature ° C	Acoustic Output (mV)	Attenuation (dB)
0	1.05	29
200	1.40	15
400	6.70	13
600	30.0	0
800	18.9	4

Table 6.2 - Data for Figure 6.16. All attenuations are referenced to 30mV.

## VII Comparison of the Argon-Ion System With Competitive Sputtering Units

Considerable attention has been paid to the the application of zinc oxide films to surface wave technology during the past several years. In particular a great deal of this activity has been directed towards developing new sputtering techniques. RF magnetron, RF diode, DC diode, and DC triode systems have each been used with varying degrees of success. To this list we now add the argon-ion deposition system.

Table 7.1 presents a comparison of the aforementioned systems with the argon ion unit in seven crucial areas; sputtering pressure, deposition rate, sputtering power, acoustic loss, coupling coefficient, surface roughness, and grain size (21,22,23). The first three of these areas are what might be termed system characteristics while the last four are related to system performance.

As previously mentioned the lower limit on the sputtering pressure is determined by the point at which a stable plasma can no longer be maintained. From Section 5 we know that lower sputtering pressures translate into a broader range of suitable substrate temperatures. The argon-ion and DC triode systems use a separate ion source and are therefore able to maintain a relatively low sputtering pressure. This separate ion source allows these

two DC systems to overcome the advantages of the RF sputtering units and achieve a comparable sputtering pressure.

The average deposition rate was determined by dividing the thickness of a sputtered film by the deposition time. Using a Tencor stylus system to measure the height of a step etched in the film, the average deposition rate was found to be .83 angstroms per second. From Table 7.1 we see that this is comparable to the rate obtained with the DC diode system, but less than all the others. While this may be a fatal disadvantage for a production environment, in the laboratory it is not as crucial a fault. In addition, these figures were obtained with a 125mA beam current. Extrapolating to the system maximum of 200mA, a deposition rate of greater than one angstrom per second should be possible.

The total power used for sputtering is closely related to the deposition rate. All other factors being equal, the DC sputtering units will sputter at a higher rate than the RF systems since DC sputtering is more efficient than RF sputtering. However, the RF units have a much greater power capability. For example, The highest powered DC unit, the DC triode system, uses only 200 watts. By comparison the RF magnetron unit uses a hefty 1.25 kilowatts. This enormous power advantage allows the RF units to overcome their inherent inefficiency and achieve the highest sputtering

rates.

The argon-ion unit is the lowest powered of the five units with 125 watts sputtering power. While the actual maximum power available is 400 watts (2KV accelerating voltage and a 200mA beam current), we know from Section 5 that the yield is independent of the accelerating voltage for voltages greater than 1KV. Therefore, the effective power limit is actually 200 watts. This places it in the same power range as the DC triode system.

The surface roughness and grain size are representative of the film density and structural uniformity. Here once again the argon ion unit is comparable to the DC diode unit, but lacking the others. In fact, there is no presence of a grain structure in the triode and magnetron films (24).

The most important figures of merit for the majority of zinc oxide applications are the acoustic propagation loss and coupling coefficient  $K^2$ . As its name suggests, the acoustic propagation loss indicates how quickly acoustic waves in the film are attenuated. This loss is usually expressed in decibels per centimeter (dB/cm) and obviously should be as low as possible. The coupling coefficient  $K^2$  is a measure of the efficiency with which the surface waves interact with electrodes on the surface of the material. To obtain the greatest possible transducer efficiency and

bandwidth,  $K^2$  should be as high as possible. For bulk single crystal zinc oxide these values are 2.5dB/cm (at 500MHZ) and .01 (23)

The best film produced to date with the argon-ion unit has yielded an acoustic loss of 5dB/cm at 50MHZ and a  $K^2$  of .009. Assuming that the loss follows a frequency squared dependence, this corresponds to an attenuation of 45dB/cm at 500MHZ. In this respect the argon-ion unit compares well with the RF diode unit and is only slightly behind the RF magnetron system.

In conclusion, we see that the argon-ion unit seems to fall in the same performance category as the RF diode system. This, in my opinion, places it above the DC diode system but behind the DC triode and magnetron units, mainly because of their greater deposition rates.

### VIII Application of the ZnO Films to the DEFT Device.

As previously mentioned, the ultimate goal of the zinc oxide technology is the development of monolithic acoustic devices on silicon. Traditionally, acoustic wave devices such as air gap correlators, convolvers, and filters (25,26) have employed taps or air gaps to interface with external silicon devices. By sputtering piezoelectric zinc oxide on silicon, the functions of active devices and acoustic modulation can be combined on one substrate.

The lack of widespread acceptance of this novel approach has focused on three points: (27)

- (1) the inability to reproducibly and inexpensively manufacture acoustic quality zinc oxide,
- (2) the instability of sputtered films under temperature extremes and aging,
- (3) the existence of undesirable properties such as the presence of surface traps and isolation problems between active and acoustic devices.

For films sputtered with the argon-ion system, problems 1 and 2 are present, but not significant. As we shall see, problem 3 has proved substantial.

Once the proper films were fabricated the next step was to determine the ideal substrate/transducer configuration for optimum coupling of the surface acoustic waves to the substrate. Following the lead of other researchers, four possible combinations were investigated;

- (28)
- (a) interdigital electrodes on top of the ZnO film and a metal film at the ZnO/Si interface,
  - (b) same as (a) but without the metal film
  - (c) the interdigital transducers at the interface and a metal film on top,
  - (d) same as (c) but without the metal film.

The results of this study indicated that configuration (a) yielded the most well defined output (ie. "least noise" ) and reproducible results. Combination (b) yielded a slightly smaller and noisier result than (a). No output was observed from either (c) or (d).

Calculations of the coupling coefficient  $K^2$  by Kino and Wagers (29) substantiates the above result. Figure 8.1 presents the calculated values of  $K^2$  as a function of the  $hk$ , where  $h$  is the film thickness and  $k$  the wave number. Here we see that configuration (a) yields a maximum at  $hk=.5$ , the typical operating region of the films (see Appendix C). Each of the other configurations yields a

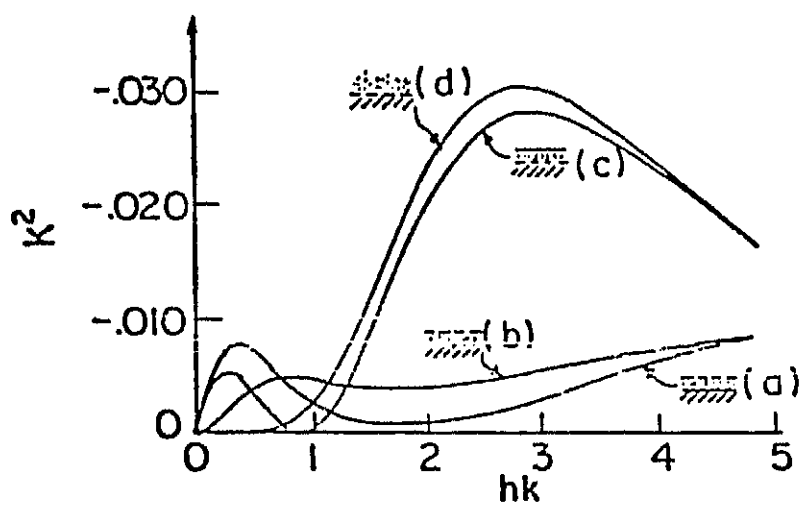


Figure 8.1 - Graph of  $K^2$  versus  $hk$  for  $hk < 5$ .

ORIGINAL PAGE IS  
OF POOR QUALITY.

value somewhat smaller. Since higher values of  $K^2$  indicate lower insertion loss, enhanced transducer efficiency, and greater bandwidth, configuration (a) should be expected to offer the best performance.

The surface acoustic wave device under consideration is a monolithic sensor composed of a silicon photodiode array (the sensors) for which the piezoelectric medium is the zinc oxide. This device, known as a DEFT (Direct Electronic Fourier Transform) device, derives an electrical signal representative of the Fourier components of an optical image by modulating the photo-generated electrons in the photodiodes with the electric field associated with the SAW. Similar devices built with CdS and lithium niobate have proved useful in spatial spectrum analysis, motion detection, and focusing (30,31).

Schematic diagrams of the device are presented in Figures 8.2 thru 8.5. The sensor consists of a 40x40 array of photodiodes, each connected in parallel, and overlaid with the sputtered zinc oxide film. The SAW transducers use a chromium-gold ground plane, a ZnO film covering the ground plane, and an interdigital aluminum film contact pattern on the ZnO film.

The general theory of the DEF device is published in numerous sources (32,33) and applies to this device. Only a

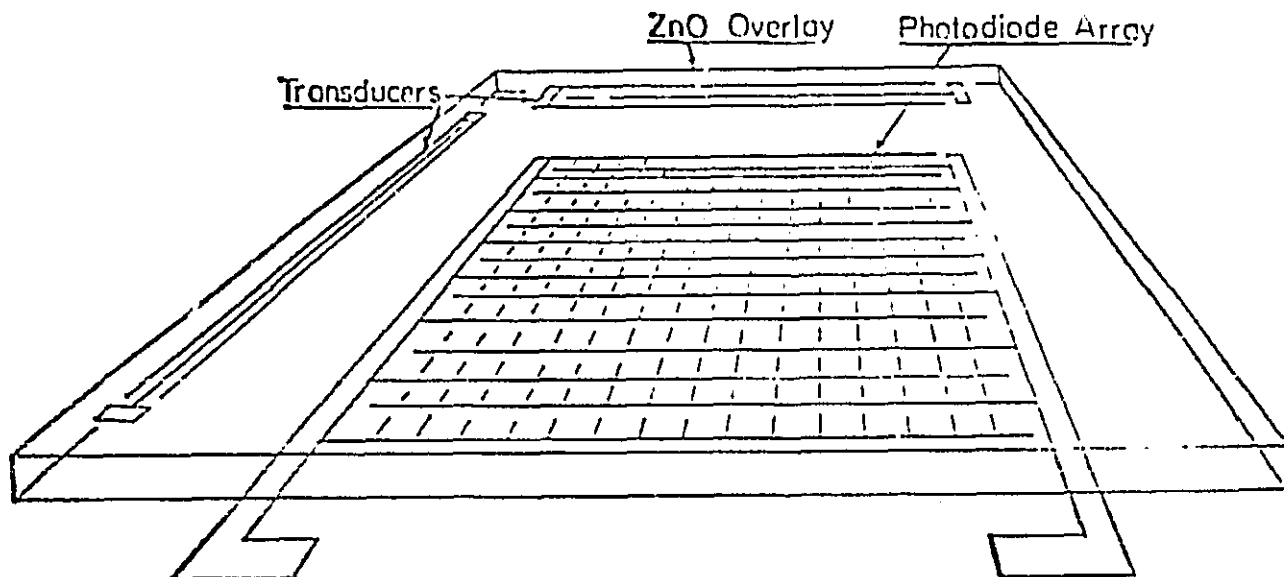


Figure 8.2 - The device consists of an array of photodiodes, each connected in parallel by an interdigital contact pattern. The array is covered with ZnO. Two transducers are located adjacent to the array.

ORIGINAL PAGE IS  
OF POOR QUALITY

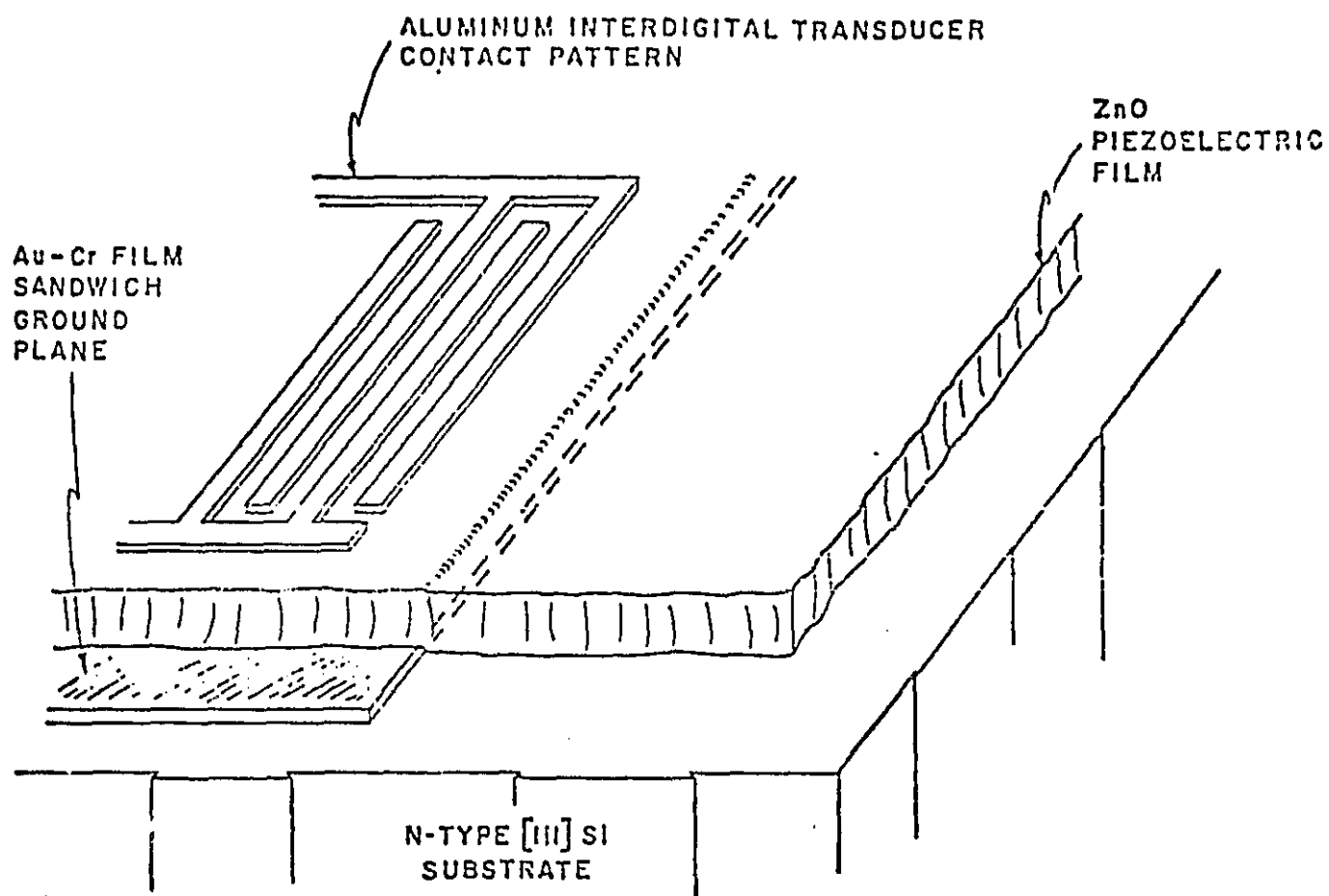


Figure 8.3 - Transducer geometry for the sensor of figure 8.2.

ORIGINAL PAGE IS  
OF POOR QUALITY.

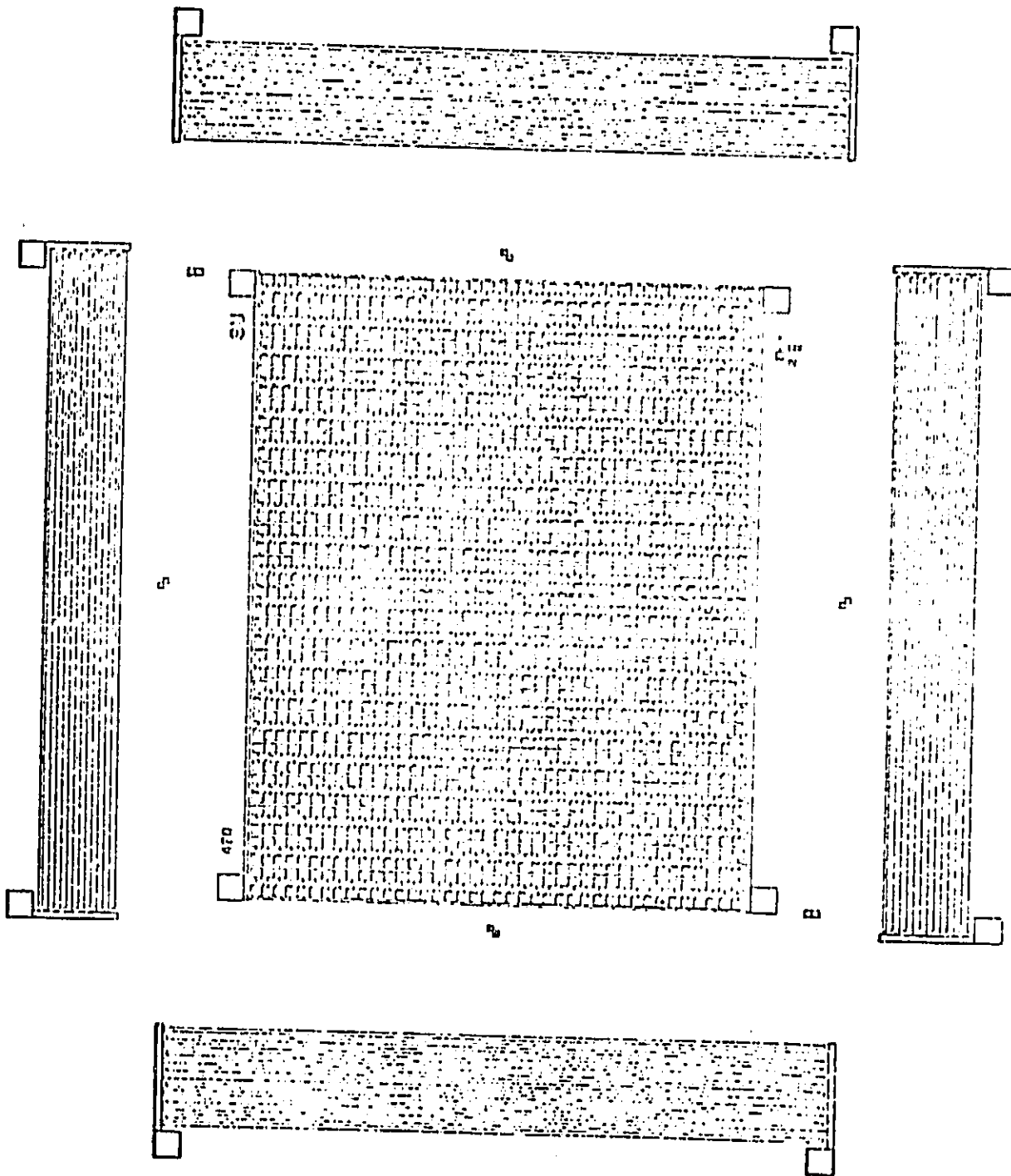


Figure 8.4 - An overview of the DEFT device.

ORIGINAL PAGE IS  
OF POOR QUALITY.

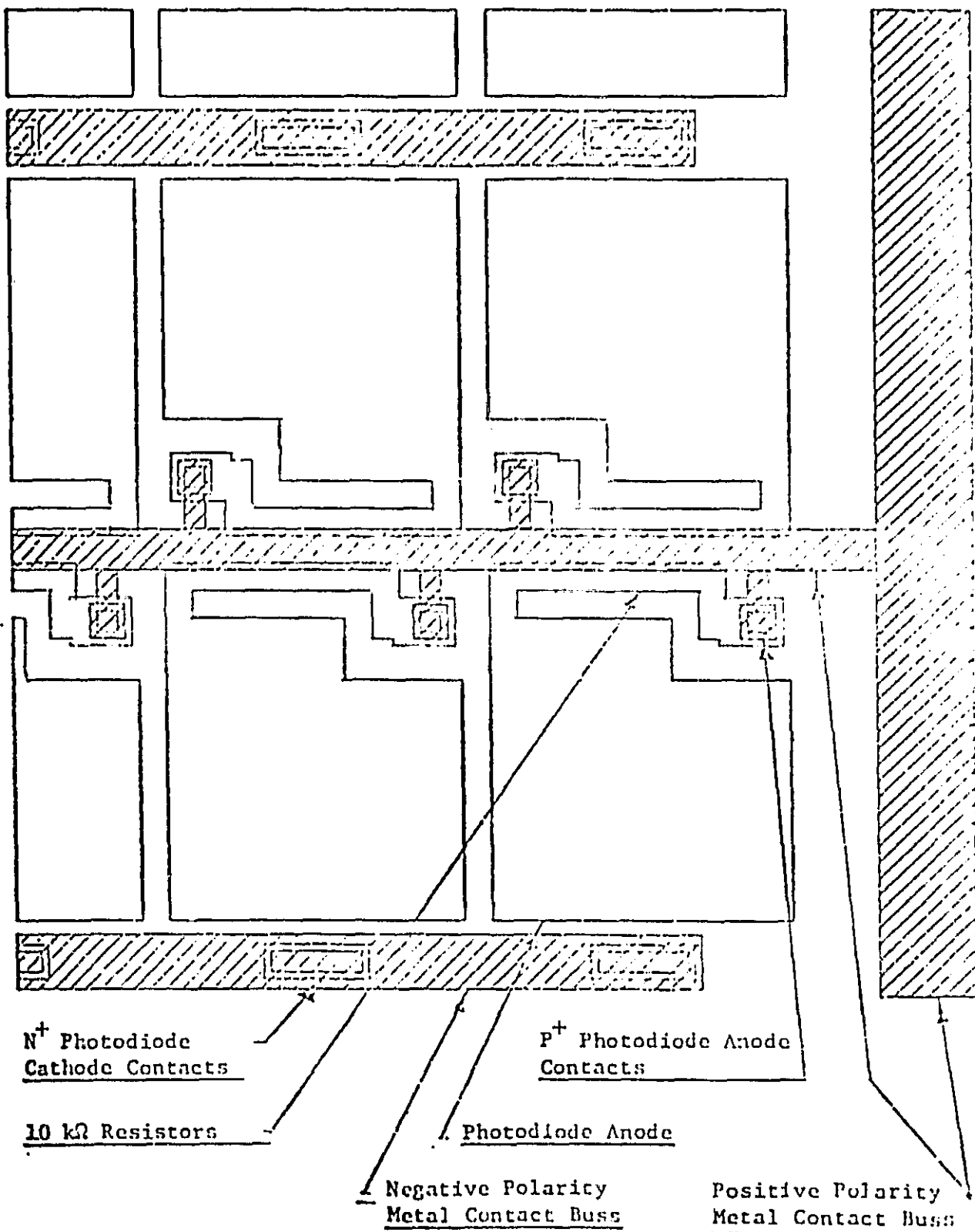


Figure 8.5 - Detail of the image sensing array elements.

ORIGINAL PAGE IS  
OF POOR QUALITY

brief description will be given here.

Suppose that we apply a sinusoidal voltage of frequency  $\omega$  to one of the transducers shown in Figure 8.4 and a sinusoid of frequency  $\omega$  to a second, orthogonal transducer.

There will then be an electrical field

$$e_x = E_x \cos(\omega t - k_x X)$$

associated with the X-propagating SAW and a field

$$e_y = E_y \cos(\omega t - k_y Y)$$

associated with the Y-propagating SAW. The total electric field will be the sum of these two fields.

Consider now the effect of projecting an optical image on the diode array. This will cause a photocurrent in the individual photodiodes. Assume that the proper bias has been applied to the diodes so that each photodiode is forced to operate in the non-linear or knee region of its operating curve (quadrant 4). Then as the surface acoustic wave passes over the photodiodes there will be a non-linear modulation of the photocurrent by the electric field associated with the SAW. This non-linear effect will create a mixing of the two surface waves, resulting in the

generation of not only the temporal sum and difference frequencies but also the vector sum and difference spatial frequencies.

The photocurrent in each diode will depend on the light intensity at the position of the diode as well as the amount of modulation by the electric field associated with the SAW's. The total current from the array will be the sum

over all the photodiodes. This sum is <sup>(33)</sup>

$$I_{\text{signal}} = C \sum_{m,n} (I_{dmn} - I_{pmn} + I_o) \exp j(q_x mb + q_y nb)$$

where

$I_{dmn}^{\text{th}}$  = bias current in the  $m$ n<sup>th</sup> diode

$I_{pmn}^{\text{th}}$  = steady state current in the  $m$ n<sup>th</sup> diode

$I_o$  = diode reverse saturation current

$q_x = k_x - 2\pi/b$

$q_y = k_y - 2\pi/h$

$b$  = periodicity of the photodiodes

$C$  = proportionality constant.

Thus the total current is proportional to the sampled Fourier transform of the image that is projected on the device. Different Fourier components may be selected by choosing appropriate frequencies for  $W_x$  and  $W_y$ .

C-2

Several prototype devices such as the one pictured in Figure 8.6 have been produced. A thin (approximately 2 micron) zinc oxide film covers the entire substrate. After annealing, the interdigital transducers are photolithographically deposited on the film and contact windows for the diode array are etched in the film. Contact is made to both the diodes and transducers via silver paint.

Unfortunately, the resultant output of the device is not as expected. When operated in the one-dimensional mode (that is, it is taking the one-dimensional transform by using only one pair of colinear transducers) and illuminated with uniform light, a sinc-function should be observed as the output. However, the output shown in Figure 8.7 is obtained. When compared with the sinc-function, we see that although there does appear to be a central maximum, the majority of the distribution is obscured by a large background noise. When the light is removed as in Figure 8.8, we see that the central maximum decreases while the background noise remains. This indicates that the expected modulation is indeed occurring.

Recent studies have shown that the presence of the undesired signal is due to improper isolation of the diode array from the acoustic input. Indeed, the background signal is present even if the ZnO film is removed, indicating that the signal is passing directly from the transducers to the diode contacts via the silicon. However,

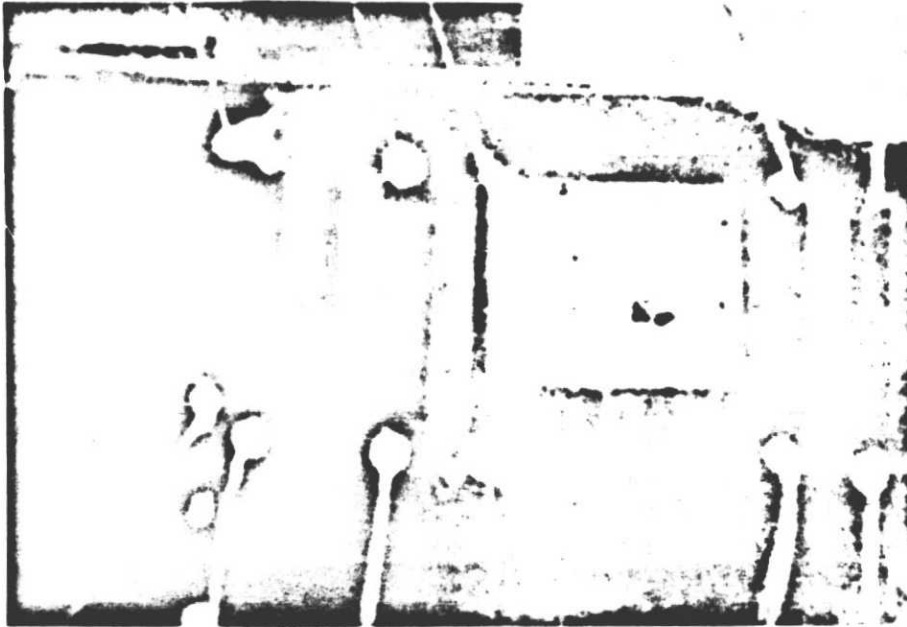


**Figure 8.6 - Prototype zinc oxide DEFT device. The device has been mounted on a glass slide to facilitate handling.**

**ORIGINAL PAGE IS  
OF POOR QUALITY.**

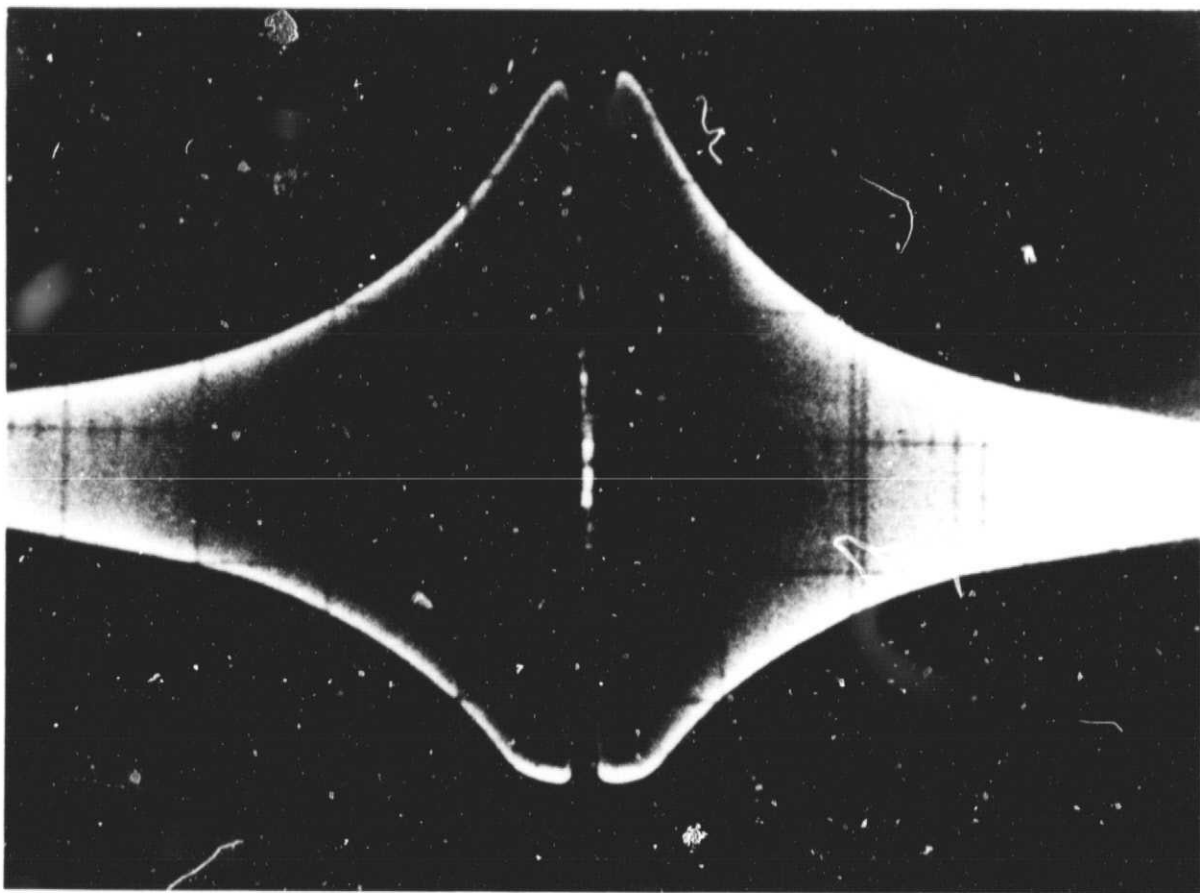


Figure 8.7 - Output of the ZnO device when illuminated with uniform light. The figure depicts the amplitude as a function of the spatial frequency. The zero at  $k=0$  is due to a filter in the detection circuit.

ORIGINAL PAGE  
BLACK AND WHITE PHOTOGRAPH

due to the large size of the diode array, it is impractical to use any of the standard integrated circuit isolation techniques for the array.

There are several approaches one may use to overcome this background noise. One is to increase the acoustic modulation so that the desired signal rises above the background. This would require an increase in the amplitude of the SAW. Such an increase may be obtained by using a thicker film and a different transducer configuration to propagate Sezawa waves rather than the present first-order Rayleigh waves (see Appendix C). A second method is to investigate other configurations for the diode array. A third alternative is to use a very high resistivity silicon. This would decrease the capacitance of the array to the substrate and help eliminate any possible current flow in the substrate between input and output.

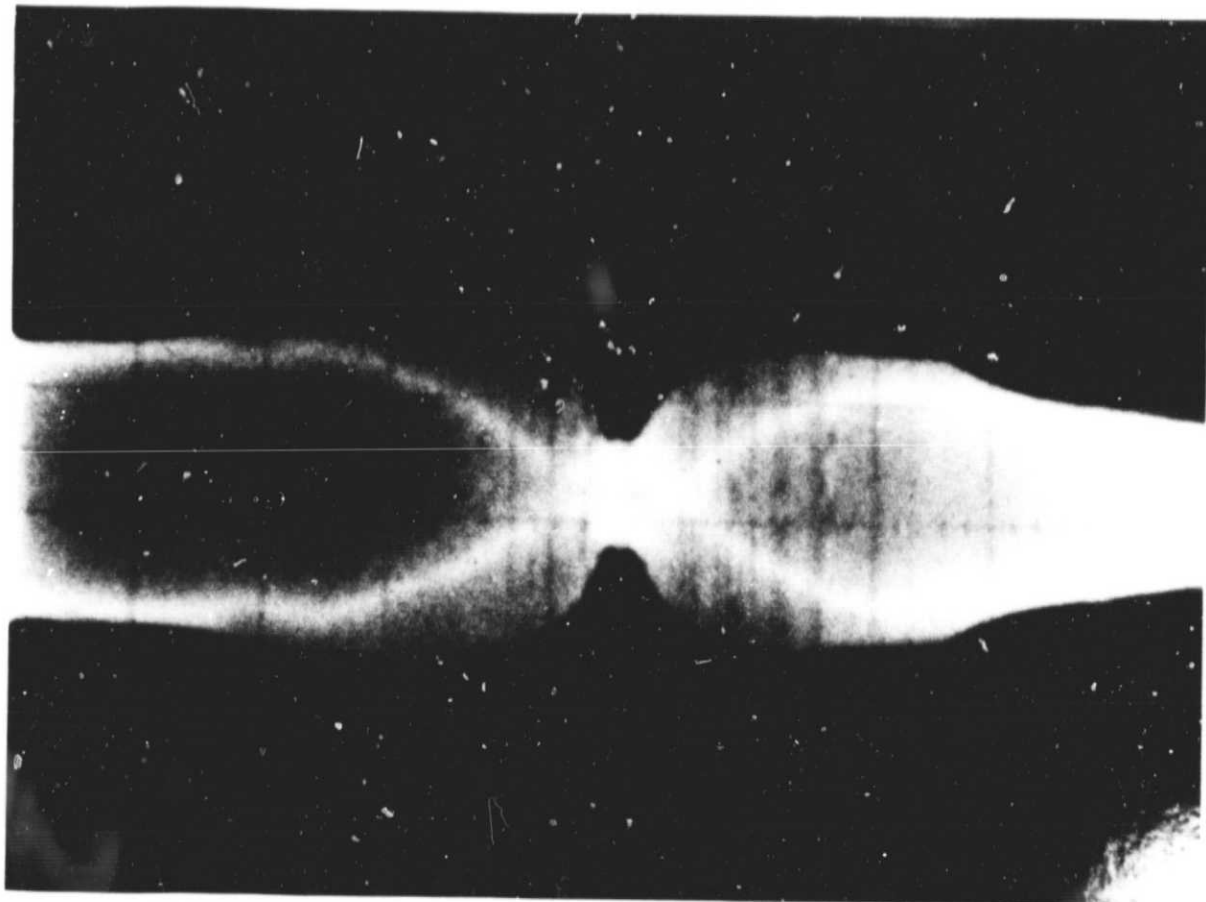


Figure 8.8 - Output of the ZnO device with no image present.

ORIGINAL PAGE  
BLACK AND WHITE PHOTOGRAPH

IX Conclusion

It is apparent that the argon-ion system is a worthy addition to the existing line of sputtering units. While it is not as fast as some, it can manufacture acoustic-quality ZnO films in a reproducible fashion. It also is capable of being converted to an ion milling apparatus within a matter of minutes. The system has proved very reliable in over two years of use. Its simplicity, cost, availability, and versatility make it a valuable addition to any facility.

As for the sensor presented in Section 8, the future is unclear. The background noise must be eliminated. It is hoped that a suitable solution can be found, thereby providing a useful addition to the fields of signal processing, robotics, and any other area in which optical image processing is important.

**Appendix A Substrate Cleaning Procedure**

The following cleaning procedure was followed prior to metalization of each substrate;

- (1) clean with soap and water,
- (2) flush with water,
- (3) flush with dionized water
- (4) flush with TCE,
- (5) blow dry with nitrogen,
- (6) flush with acetone,
- (7) blow dry with nitrogen,
- (8) flush with methanol,
- (9) blow dry with nitrogen.

ORIGINAL PAGE IS  
OF POOR QUALITY

## Appendix B Scanning Auger Electron Spectroscopy Standards

The Auger electron spectroscopy standards for elemental zinc, oxygen, carbon, and argon are presented <sup>(34)</sup>. Each of these curves is for the primary electron energy of 3KeV which was used exclusively in this report.

These standards allow for a rapid determination of the elements present in the film. By comparing the location of the energy peaks in the Auger analysis of a given film with the standard curves, the elemental composition of the film can be found. For example, if the Auger analysis of a film shows a peak at 503eV, then from Figure B.1 we can conclude that there is oxygen present. This process is then repeated for all the peaks present in the analysis.

ORIGINAL PAGE IS  
OF POOR QUALITY

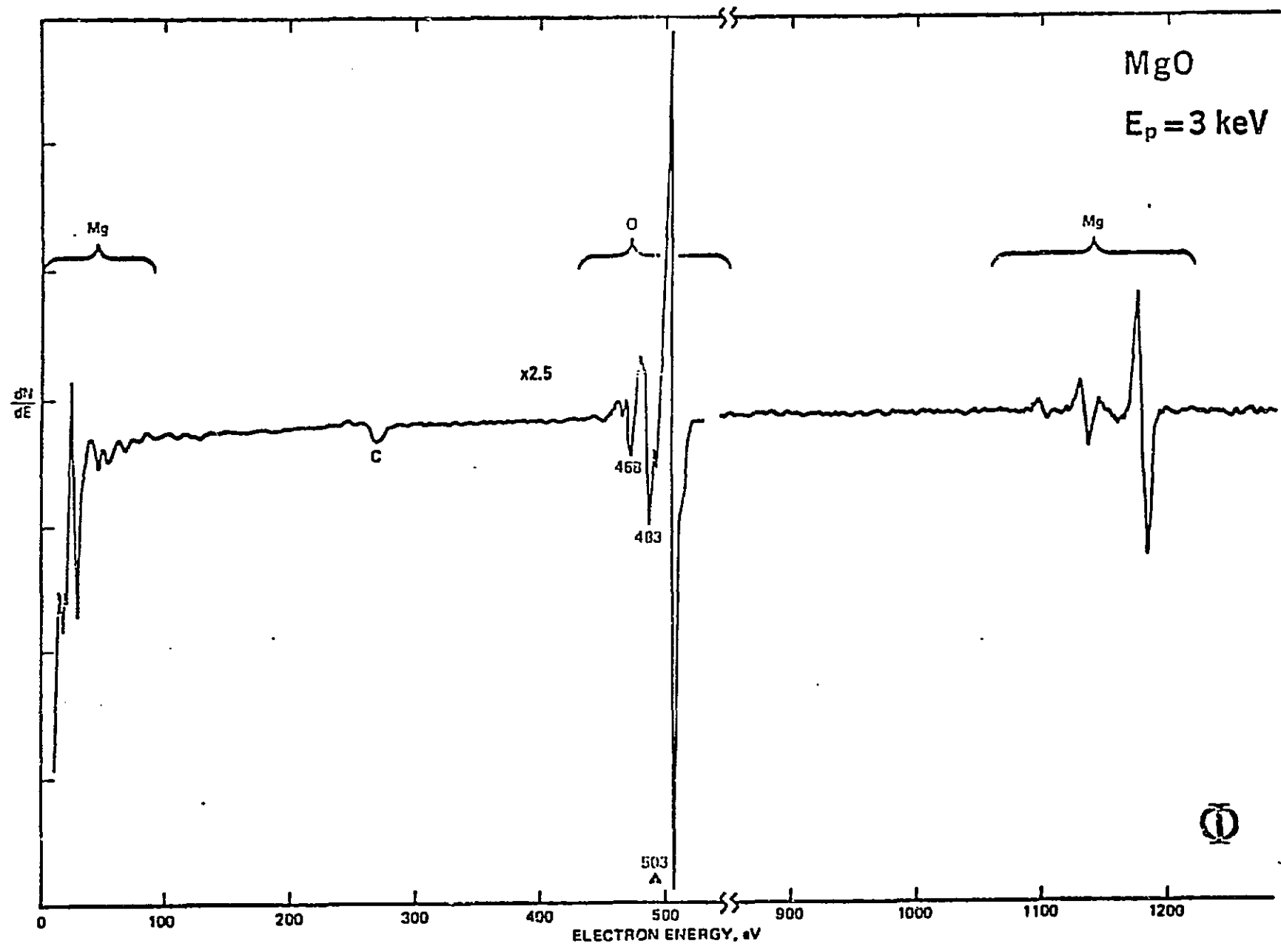


Figure B.1 - Auger standard for oxygen.

ORIGINAL PAGE IS  
OF POOR QUALITY.

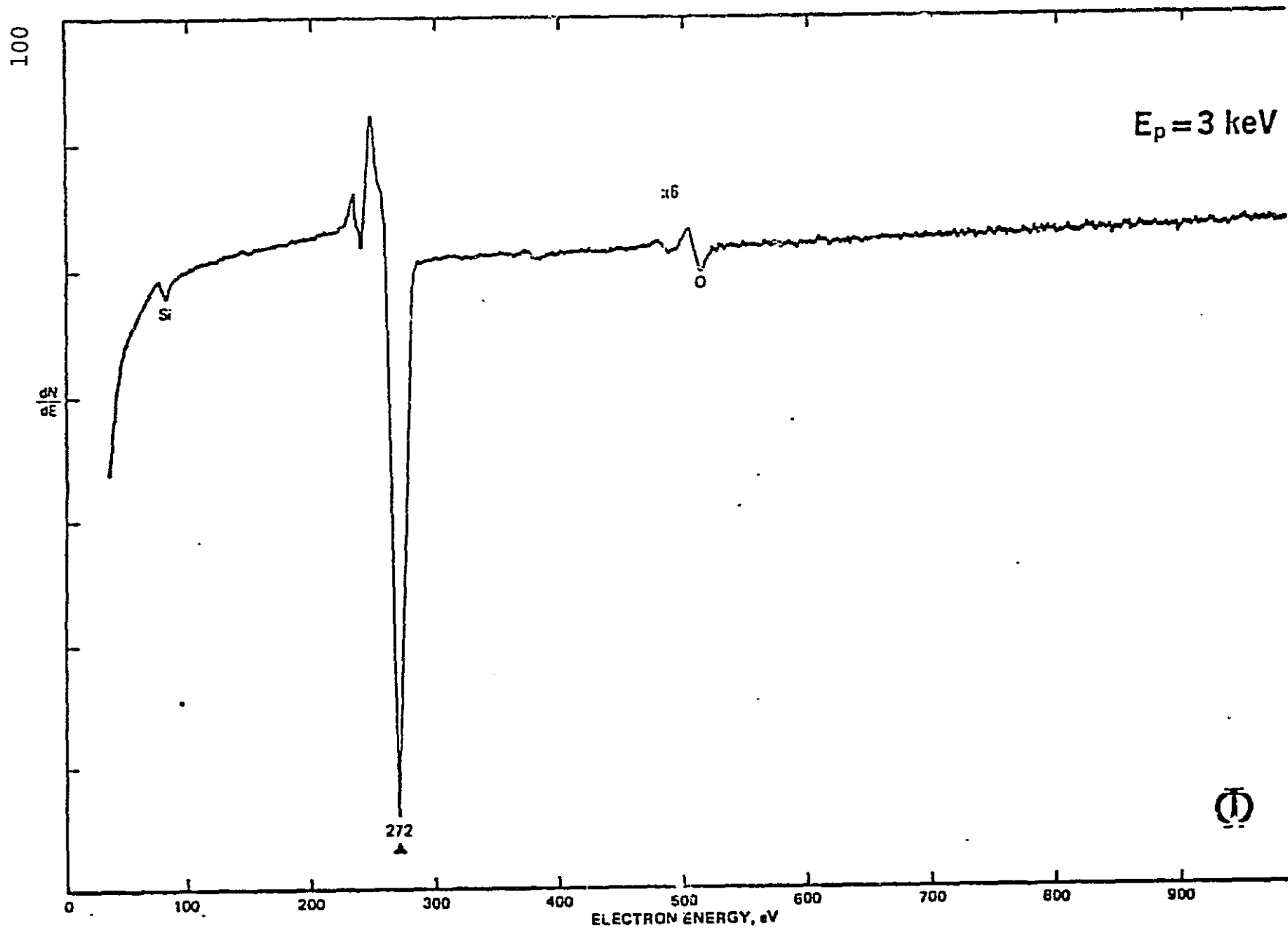


Figure B.2 - Auger standard for carbon.

ORIGINAL PAGE IS  
OF POOR QUALITY

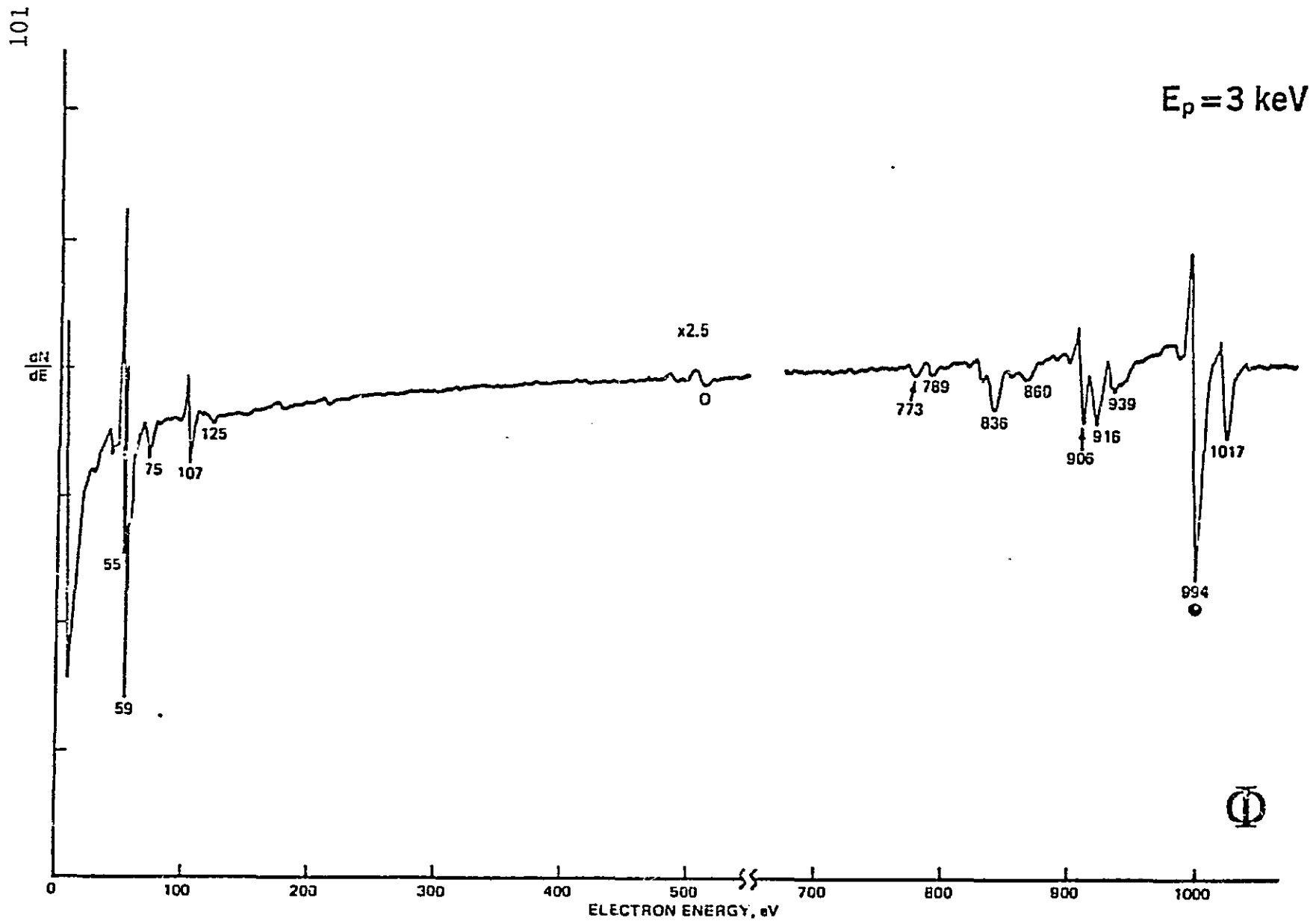


Figure B.3 - Auger standard for zinc.

ORIGINAL PAGE IS  
OF POOR QUALITY.

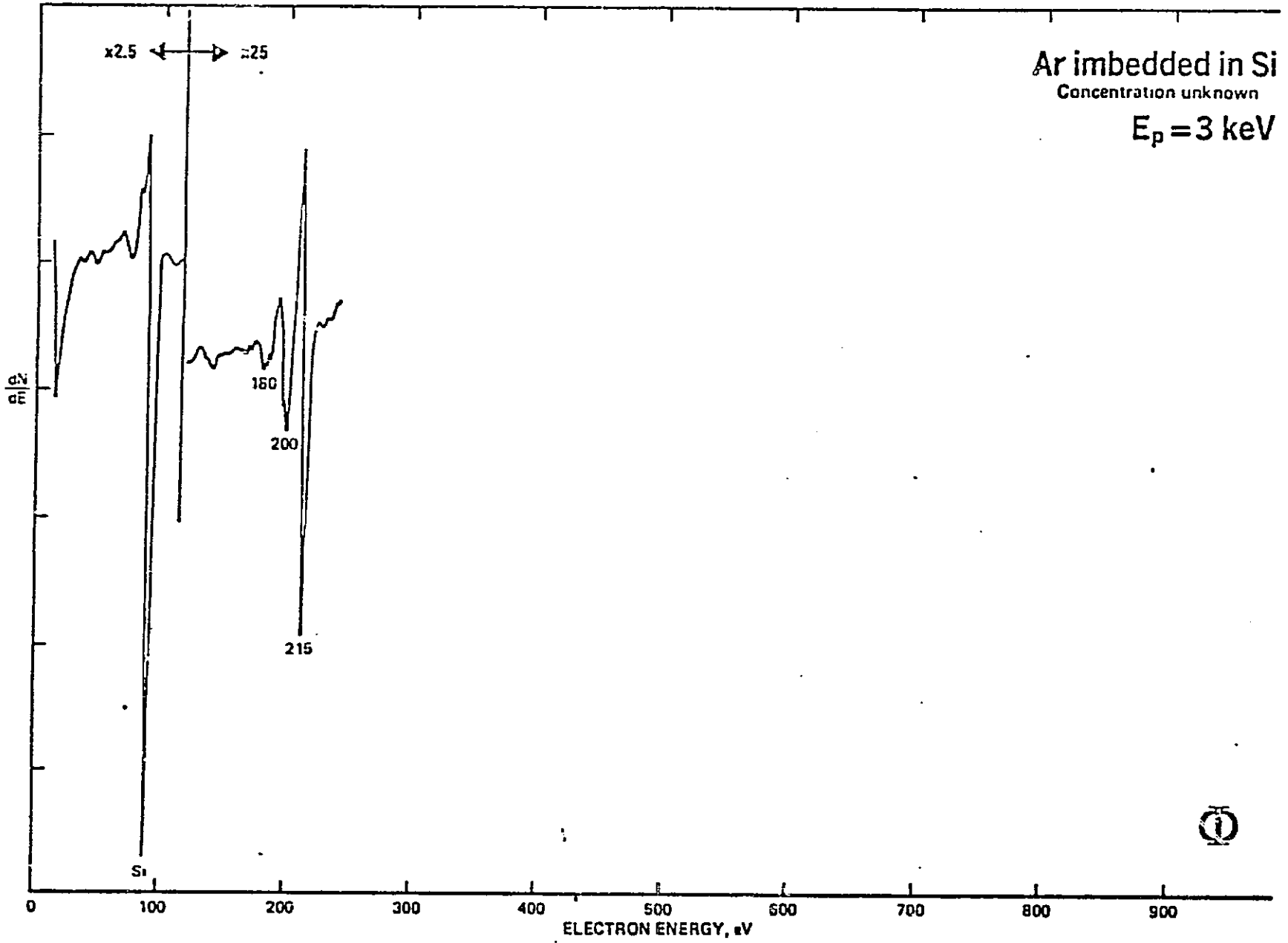


Figure B-4 - Auger standard for argon.

ORIGINAL PAGE IS  
OF POOR QUALITY

## Appendix C Calculation of the Acoustic Mode

Most monolithic surface acoustic wave (SAW) devices consist of a thin piezoelectric layer placed in intimate contact with the surface of a substrate. The SAW is generated via an alternating electric field applied to an interdigital transducer such as the one shown in Figure C.1 (see also Figures 6.14 and 8.3).

A thorough evaluation of the types of waves that may propagate in both the substrate and film involves consideration of a thin, piezoelectric, anisotropic layer of thickness  $h$  and a certain crystalline orientation placed on an anisotropic substrate of some other crystalline orientation. This results in two wave equations, one for each material, and a total of 12 boundary conditions. If the solution to these equations is assumed to be the superposition of a number of partial waves, then a total of eight separate waves will be obtained <sup>(35)</sup>. This is obviously a rather formidable problem.

Fortunately, most of the cases of interest involve an isotropic, piezoelectric layer (ZnO) on an isotropic, non-piezoelectric substrate (silicon). For this case the wave equation yields two separate sets of solutions, or modes. The first mode, known as a Rayleigh wave, involves only sagittal plane displacements. The sagittal plane is the plane which contains the wave vector  $k$  and the surface

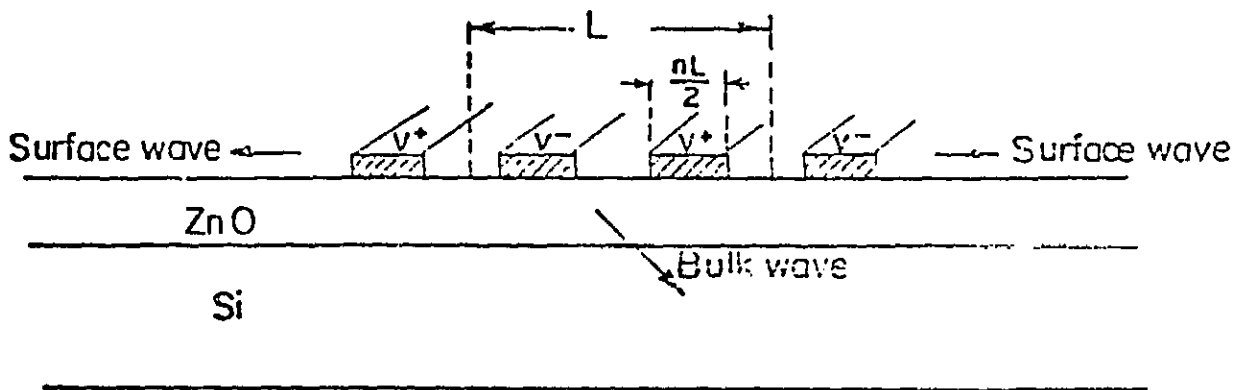


Figure C.1 - A cross-section of the interdigital transducer. Notice that the wavelength of the SAW is determined by the geometry of the transducer.

ORIGINAL PAGE IS  
OF POOR QUALITY.

normal. The second mode is called a Love mode and is characterized by displacements perpendicular to the sagittal plane (Figure C.2). However, Love modes are not excited by interdigital transducers.

Some general conclusions are possible <sup>(36)</sup>. The dominant phenomenon is that the medium in which the wave propagates becomes dispersive, with the phase velocity depending on the ratio of the acoustic wavelength  $L$  to the film thickness  $h$ . For small  $kh$  ( $k=2\pi/L$ ), most of the energy of the wave is carried in the substrate with the wave decaying exponentially in depth. As  $kh$  increases, more of the energy is contained within the thin layer. Of course, since the film is piezoelectric, there will be an electric field associated with each wave in the film.

We now concentrate on the specific case of zinc oxide on silicon. Since these materials satisfy certain conditions on the surface wave velocity <sup>(35)</sup>, there will be many independent Rayleigh-type modes in the ZnO. Each mode will have a minimum value of  $kh$ , below which solutions with real  $k$  are not allowed. At this value of  $kh$  the wave will cease to propagate. The wave which propagates for the smallest value of  $kh$  is a first order Rayleigh wave, that with the next largest value a second-order Rayleigh wave (commonly called a Sezawa wave), and so on. These higher order solutions exhibit a progressive higher phase

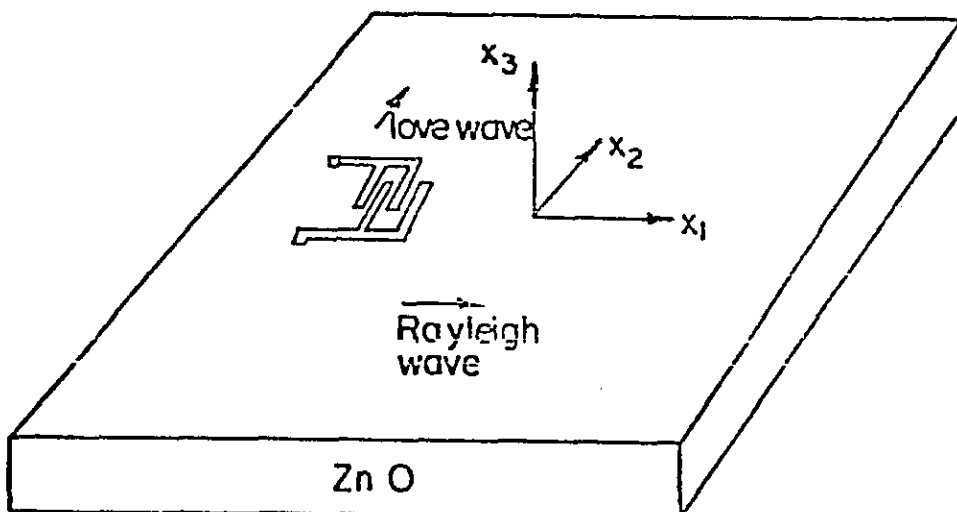


Figure C.2 - Direction of propagation of the Rayleigh wave. The wave vector  $k$  lies along  $X_1$ .  $X_3$  is the surface normal.  $X_1$  and  $X_3$  form the sagittal plane. The direction of the Love wave is given for reference.

ORIGINAL PAGE IS  
OF POOR QUALITY

velocity and coupling coefficient, making them very desirable for SAW work. However, they also require a much thicker film.

(37)

Workers at Stanford have numerically determined the dispersion characteristics for those waves that may propagate in ZnO on silicon. Figure C.3 shows the dispersion characteristics for a film thickness  $h < (6/k)$ . This figure provides a vehicle for determining which mode (or modes) may propagate in the material. Given the phase velocity, film thickness, and wavelength of a certain wave, then the wave type can then be quickly identified from Figure C.3.

The film thickness is easily determined either by knowing the sputtering rate and deposition time or from one of the standard thickness measuring techniques (inductive stylus, interferometer, etc...). To find the phase velocity and wavelength, one of two methods may be employed.

The first method involves the geometry of the interdigital transducer. From Figure C.1 we see that if the dimensions of the transducer are known, then the wavelength of the resulting SAW is easily determined. The resonant frequency  $F$  of the transducer can then be found by maximizing the acoustic output with respect to frequency. For this transducer resonance will occur at frequencies which correspond to an odd multiple of the acoustic

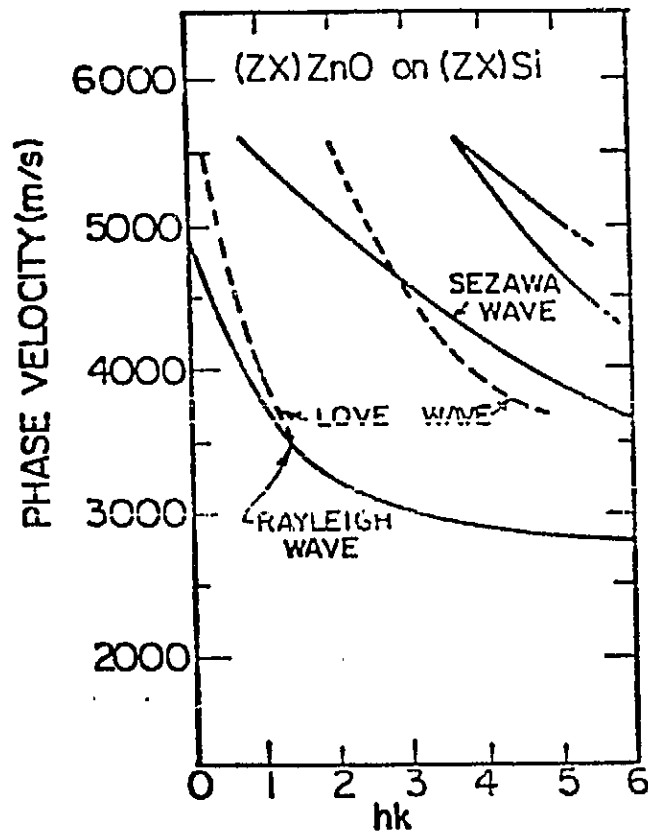


Figure C.3 - Dispersion characteristics of the various modes for ZnO on silicon.

ORIGINAL PAGE IS  
OF POOR QUALITY

wavelength. The phase velocity  $V$  and wave number  $k$  are then calculated from the relationship

$$V = \lambda L$$

Once these are known, the corresponding mode can be obtained from Figure C.3.

For the second method the wave velocity is determined by measuring the center-to-center spacing between consecutive transducers and the time required for a pulse of frequency  $F$  to propagate between them. The wavelength can then be found from the above equation.

Both of these techniques were used to determine which mode was present in the zinc oxide film. For this analysis, a film with six consecutive transducers was used, allowing an averaging of the data. The thickness of the film was measured using a Tencor stylus system and the separation between transducers found using a Unitron measuring microscope. The results are presented in Tables C.1 and C.2, with the corresponding points shown in Figure C.3.

From Figure C.3, we see that the SAW being observed is indeed a first-order Rayleigh wave. This is expected since, as previously stated, the Love wave is not excited by interdigital transducers and the Sezawa wave will not propagate for such a low film thickness.

Separation (millimeters)	Delay (nanoseconds)	Velocity (Kilometers/sec)
3.92	800	4.90
3.05	650	4.69
3.71	850	4.36
4.13	850	4.86
3.73	850	4.39

Average Velocity            4.64Km/Sec

Frequency                    45.4MHz

Film Thickness                4 microns

Wavelength                    .1022mm

Wave Number                   $61.5 \times 10^3$  /meter

hk                                .246

Table C.1 - Calculation of the acoustic mode by measuring the separation between successive transducers.

L (microns)	V (Kmeters/sec)	k (1000/meter)	hk
102	4.63	61.56	.246
103	4.68	61.02	.244
102	4.63	61.56	.246
101	4.59	62.18	.249
103	4.68	61.02	.244
100	4.54	62.80	.251

Table C.2 - Calculation of the acoustic mode using the geometry of the interdigital transducer.

### Acknowledgements

We would like to thank the National Aeronautics and Space Administration which provided the financial support for this research.

We would like to thank Mr. Din How Mei of Syracuse University for performing the diffraction analysis presented within.

We are grateful to Dr. Edward Wolf, Director of the National Research and Resource Facility for Submicron Structures (NRRFSS) at Cornell University for the use of its outstanding facilities and to Dr. Lynn Rathbun of NRRFSS for performing the Auger analysis presented in this report.

ORIGINAL PAGE IS  
OF POOR QUALITY

REFERENCES

- 1) Handbook of Thin Film Technology, McGraw-Hill, 1970, 4-2.
- 2) Integrated Circuit Engineering, Glaser-Subak Sharpe, Addison Wesley, Mass., 1979, Chap. 5.
- 3) Introduction to Thin Films, Leon Maissel, New York, Gordon and Breach, 1973.
- 4) Thompson, M.W., and R.S. Nelson, Phil. Mag., 7, 84, 2015, 1962.
- 5) Ref 1, pq. 3-16.
- 6) Gurmin, B.M., and T.P. Martynenko, Fiz. Tverd. Tela., 10, 411, 1968.
- 7) Ref 2, pq 171.
- 8) Nelson, R.S., and C.J. Beevers, Phil. Mag., 9, 343, 1964.
- 9) Veeco Microetch Owners Manual, Veeco Instruments Inc., Plainveiw, New York.
- 10) Wagers, R.S., Kino, G.S., Galle, P., and D. Winslow, "ZnO Acoustic Transducers Utilizing Crystalline Gold Substrates", 1977 IEEE Ultrasonics Proceedings.
- 11) Khuri-Yakub, E.T., and J.G. Smits, "Reactive Magnetron Sputtering of ZnO", 1980 Ultrasonics Symposium, pq. 801.
- 12) Aita, C., "Sputter Deposition of ZnO Thin Films Using Glow Discharge Mass Spectrometry", 1980 Ultrasonics Symposium, pq. 795.
- 13) Vincent, P.S., Barlow, W.A., and G.G. Roberts, "Quality of Vacuum Deposited Films", Nature, Vol. 255, pp. 542-544, Jun. 1975.
- 14) Use of the Scanning Electron Microscope, Hearn, J.W.S., Pergamon Press, Oxford, 1972.
- 15) Handbook of Auger Electron Spectroscopy, Physical Electronics Industries Inc., Minn., 1976.
- 16) Ref. 1, pq. 4-25.
- 17) Thornton, J.A., "Influence of Apparatus Geometry and Deposition Conditions on the Structure and Topography

- of Thick Sputtered Coatings", J. Vac. Sci. Tech., Vol. 16, 11, pp. 666-670, Jul./Aug. 1974.
- 18) Scheonwald, J.S., Keester, K.L., and E.J. Staples, "Characterization of RF Sputtered ZnO and ZnS Thin Films for SAW Transducers by X-Ray Diffraction Analysis", 1979 Ultrasonics Symposium, pg. 926.
  - 19) Wanuga, S., Medford, T.A., and J.P. Deitz, "Zinc Oxide Film Transducers", 1965 IEEE Ultrasonics Symposium, pg. 785.
  - 20) Basic Integrated Circuit Engineering, Hamilton and Howard, McGraw-Hill, 1975, Chapter 2.
  - 21) Hickernell, F.S., "ZnO Processing for Bulk and Surface Wave Devices", 1980 IEEE Ultrasonics Symposium, pg. 785.
  - 22) Hickernell, F.S., "Low Loss Zinc Oxide Optical Waveguides on Amorphous Structures", Digest of the Topical Meeting on Integrated and Guided Wave Optics, pp. WBG-1 to WBG-4, 1980.
  - 23) Ref. 11, pg 803.
  - 24) Yamamoto, T., Shiosaki, T., and A. Kawabita, "Characterization of ZnO Piezoelectric Films by RF-Planar Magnetron Sputtering", J. Appl. Phys., Vol. 51, pp. 3113-3120, Jun, 1980.
  - 25) Green, J.B., and B.T. Khuri-Yakub, "A 100 Micrometer Beamwidth ZnO on Silicon Convolver", 1979 Ultrasonics Symposium, pg. 911.
  - 26) Chuinq, "Thin Zinc Oxide Film Array for Programmable Filters and Scanned Receiving Transducers", 1979 IEEE Ultrasonics Symposium, pg. 915.
  - 27) Ref. 18, pg. 928.
  - 28) Kino, G.S., and R.S. Wagers, J. Appl. Physics, 44, 1480, April 1973.
  - 29) Kino, G.S., "Zinc on Silicon Acoustoelectric Devices", 1979 IEEE Ultrasonics Symposium, pg. 900.
  - 30) Kornreich, P., Kowel, S.T., Fleming, D., Yang, N.T., Gupta, A., and O. Lewis, "DEPT: Direct Electronic Fourier Transforms of Optical Images", IEEE Proceedings, Vol. 62, No. 8, pg. 1072-1087, August 1974.
  - 31) Kowel, S.T., Kornreich, P., and O. Lewis, "Passive Detection of Motion Transverse to the Optical Viewing

- Axis", IEEE Transactions on Instrumentation and Measurement, Vol. IM-24, pp. 244-255, September, 1975.
- 32) Kowel et.al., "The Vector Imaging Convolver", 1977 IEEE Ultrasonics Symposium, pp. 715.
- 33) Kowel, S.T., and P. Kornreich, NASA/Langley Contract NSG1611, Report 1, October, 1979.
- 34) Ref. 15, pp. 25,34,65,99.
- 35) Surface Wave Filters, Herbert Mathews, J. Wiley and Sons, 1977, pg 31.
- 36) Acoustic Surface Waves, A.A. Oliner, Springer-Verlag, Chapter 1.
- 37) Physical Acoustics, W.P. Mason, Academic Press, 1966, Chapter 1.
- 38) Ref. 29, pp. 909.
- 39) Kowel, S.T., and P. Kornreich, NASA/Langley contract NSG1611, Report 4, December 1981.

ORIGINAL PAGE 13  
OF POOR QUALITY